Physiological and metabolical high-resolution MRI of plants

Dissertation zur Erlangung des
naturwissenschaftlichen Doktorgrades
der Julius-Maximilians-Universität Würzburg

vorgelegt von

Eberhard Munz

aus Würzburg

Würzburg, 2018

Eingereicht am: 28. Februar 2018
bei der Fakultät für Physik und Astronomie

1. Gutachter: Prof. Dr. rer. nat. Peter Michael Jakob
2. Gutachter: Prof. Dr. rer. nat. Randolf Hanke
der Dissertation

Vorsitzender: Prof. Dr. rer. nat. Jean Geurts

1. Prüfer: Prof. Dr. rer. nat. Peter Michael Jakob
2. Prüfer: Prof. Dr. rer. nat. Randolf Hanke
3. Prüfer: Prof. Dr. rer. nat. Ansgar Denner
im Promotionskolloquium.

Tag des Promotionskolloquiums: 19. Oktober 2018
Doktorurkunde ausgehändigt am: .....

All energy flows according to the whims of the Great Magnet. What a fool I was to defy him.

Raoul Duke

(from: 'Fear and Loathing in Las Vegas', written by Hunter S. Thompson)

Contents

Chapter 1
Introduction

The interest of the food and energy industries in oilseed and cereal plants has been growing for years. Despite the wide variety of mostly invasive analytical methods based on sectioning and extraction, the transfer of the obtained results to the living plant organisms is challenging if not impossible. Typically, a large number of plants or seeds is analysed for retrieving significant results from the measured data. The examined samples are destroyed during the process, thus the personnel involved has to work thoroughly during the preparation, sectioning and staining procedures to ensure the unambiguousness of the obtained results. Yet, the data gained remains a snapshot of the sample's status - if it wasn't truncated by the invasiveness of the applied methods itself.

Nuclear magnetic resonance (NMR) offers a variety of means for noninvasive imaging and analysis of living organisms. The specific manipulation of nuclear spins enables the encoding of different information into the NMR signal. In the well-known clinical application of magnetic resonance imaging (MRI), two- and three-dimensional images of human organs can be acquired with a sufficiently high resolution within a few minutes.

The plant as an MRI research object usually requires less precautions than humans in clinical measurements. The application of higher magnetic field strengths, which in MRI experiments leads to an increase of signal, allows for the acquisition of datasets with increased spatial resolution typically in the range of tens of micrometers. This advantage is accompanied by influences on the magnetic homogeneity of the sample leading to an accelerated decay of the NMR signal during acquisition. Conditioned by the plant's anatomy, the utilized MR imaging analysis protocols have to be adjusted to the sample in order to obtain reliable information about anatomy, growth, metabolite transport, and metabolism. By adaption of MRI protocols developed for clinical applications or for the spectroscopic analysis of samples, dynamic measurements containing chemical information about the living organism can be acquired. The measured object is not destroyed, metabolism can take place uninfluenced. The results gained can be used to validate the results from the previously and invasively acquired data. Since

MR imaging is capable of acquiring three-dimensional data, the sectional plane in a dataset can be adjusted at any time, thus answers to questions can be addressed in retrospect.
Starting in 1986 with the investigation of the root system of *Vicia faber* [Bot86], several research groups, typically consisting both of biologists and physicists, worked on the development of various NMR and MRI applications on plants. While some groups mostly focus on the visualization and quantification of flow in plant stems [VA84], other groups concentrate on the analysis of plant roots [Pfl17] via MRI. Some cooperations, such as the one between the Department of Experimental Physics V (University for Würzburg) and the research group Assimilate Allocation and NMR (IPK Gatersleben), investigate the accumulation and spatial distribution of lipid in plant seeds.
Metaphorically speaking, in the map of MR plant imaging, some areas are well-explored while other regions still remain blank spots. This work aimed to fill some of these unexplored areas by developing methods for both physiological and metabolical magnetic resonance imaging of plants and seeds. Some of the experiments are based on projects previously conducted in the Department of Experimental Physics V [Kau08; Mel09a; Win11; Fuc13]. The main focus lied on the chemical shift-selective imaging of lipid-rich seeds, such as the rapeseed seed and the soybean. The spatial distribution of lipids in the seeds allows for direct comparison between different seed types and a 3D visualization of the outcome of plant breeding.

After a short overview of the basics of MRI and the anatomy and functionality of plants, the challenges regarding plant imaging via magnetic resonance are discussed. Limitations are mostly caused by the susceptibility differences in plant tissue. For this reason, most plant experiments are performed with a standard MR sequence, the spin echo [Hah50], since it can compensate the signal loss induced by the inhomogeneities in the plant tissue.
An overview of lipid-imaging in plants within the last decade is provided in Chap. 4, presenting the recent developments in this area. Unsurprisingly, most experiments were performed with pulse sequences based on the spin echo imaging.
The re-awakening of a plant seed during germination is one of nature's many little wonders, understanding the temporal and spatial pattern of this process was the aim of Chap. 5 in this work. Chemical shift-selective imaging was applied for high-resolution analysis, both in temporal and in spatial dimension. Combined with 3D rendering and visualization techniques, major questions in biological research, such as the entry point of water into the germinating seed and the pattern of re-awakening were addressed.
By adapting this MRI sequence and including a selective saturation module [Haa85],

chemical shift-selective 3D datasets of seeds were acquired for spatial localization of different fatty acid components in the plant tissue. The results are presented in Chap. 6.
The direct imaging of plant tissue with short relaxation times was performed in Chap. 7 by adjusting an ultrashort echo time sequence (UTE, [Ber91]), in order to obtain an improved visualization of dry seed tissue.
In Chap. 8, the dynamic imaging of transport processes in living plants was conducted by applying a contrast agent to the plant and using it as a tracer. For this experiment, T_1-maps had to be acquired with an improved temporal resolution, thus providing the means to determine longitudinal and horizontal transport velocities in the plant tissue.

The results obtained underline the capabilities of magnetic resonance imaging in plant science and demonstrate the variety of questions that previously could not be addressed in living organisms.

Chapter 2
The plant fundamentals

The anatomy of the plant is very different to the mammal's, thus many challenges and restrictions regarding the imaging capabilities of MRI appear. In this chapter, a short overview of the plant's anatomy and its organs is provided to explain the major challenges and limitations of MRI on plants.

Preface

On our planet, approximately 310,000 species of plants exist; the majority of them (approx. 270,000) reproduce via seeds [Int17]. Plants produce most of the molecular oxygen in the atmosphere and the human diet is entirely dependent on plants - either via direct nutrition or as a feed for the animal meat industry.
Typically, plant research is based on invasive analytical tools, such as microscopy, mass spectrometry, and FTIR (Fourier-transform infrared spectroscopy). These technologies have produced detailed insights into the plant's anatomy. The investigation of dynamic processes, such as the uptake of water, with these techniques is hampered by the invasiveness. In most cases experiments rely on staining dyes that are taken up by the plant and which can be detected in the sections. When using a staining protocol, the results obtained on different plants have to be interpolated for the estimation of dynamic processes.
While magnetic resonance imaging cannot, however, reach the detailed image resolution of advanced microscopy analyses, MRI can, in contrast, provide the dynamic information of one individual plant sample. Since the sample is not destroyed during an MR experiment, further analyses of the object investigated can still be performed.
In plant imaging via MRI, some restrictions and difficulties appear, which are related to the physical properties of the plant tissue. Before a detailed explanation of the physical processes leading to a decay of the NMR signal is provided, the basics of the plant's anatomy and its organs is explained.

2.1 Plants - anatomy and functionality

The body of the plants consist of the root, the leaves, the stem, and the fruits containing the seeds.
The plant's life cycle starts with a single **seed**. During the germination process, the **root** breaks through the seed coat and starts to provide the growing plant with nutrients and water taken up from the soil. A filtering system in the root's surface determines the uptake of components dissolved in the ground's water. The roots serve the plant as a footing to the ground and a support.
The plant produces nutrients via photosynthesis in the **leaves**; these nutrients are transported through the vascular system towards the root and the reproductive organs, thus the flowers and the seeds.
The **vascular system** connects all plant organs and mediates the water and metabolite exchange at the level of entire organs. This transport process is typically called translocation. The main components dissolved in the water are sucrose and amino acids. In the plant, two different vascular subsystems are present: the xylem and the phloem. The xylem's main function is the transport of water from the roots towards the shoots and leaves, replacing the water being lost due to transpiration and photosynthesis. In the xylem sap, inorganic ions and some organic chemicals can be present, yet it mostly consists of water. The phloem transports soluble organic compounds built during the photosynthesis in the source locations (leaves) towards the consumption places in the plants (sinks).
Any plant organ consists of **various tissues**, as for example the epidermis (bordering tissue), the chlorenchyma (supporting tissue), the storage parenchyma, and others. The individual function and specialisation of the tissues is reflected in their structure and tissue heterogeneity. Within all tissues, the individual cell types are each characterised by different thicknesses of the cell walls, the sclerenchyma for example contains thick and lignified cell walls in order to provide structural support for the plant.
In this work, the focus was set on the crop plants rapeseed (canola), wheat and barley. Further plants, such as pea, soybean, maize, and olives have also been investigated via MRI, yet the plant's structure will be explained in detail for the crop plants.
The **rapeseed** (*Brassica napus*), also known as rape, oilseed rape or canola, is one of the most important crops worldwide [Bor13b]. This plant's yield contains about forty percent oil and serves as a high-protein animal feed, rendering it an important plant for the agricultural industry. It is also used for the human nutrition, e.g. in the production of vegetable oils.
The rapeseed plant (Fig. 2.1 A) consists of the roots in the soil, the stem with the

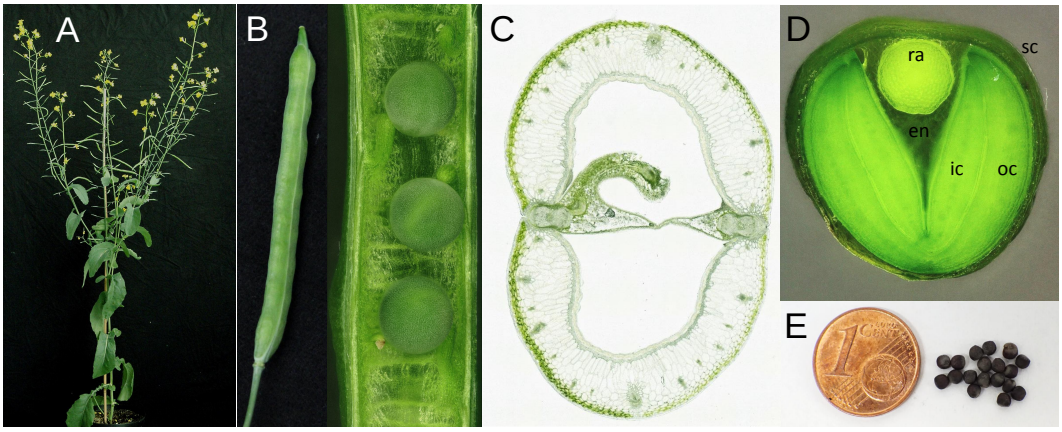

Figure 2.1: **A** The rapeseed plant, first siliques are growing while flowers are blooming at the top of the branches. **B** A closed silique and three seeds in a silique, attached to the replum via the funiculus. **C** Section through a silique, showing two halves divided by the replum and a funiculus. In the silique's tissue, the vascular bundles for nutritional support of the silique can be seen. **D** Section through a maturing rapeseed. The seed coat (sc) protects the embryo growing in the liquid endosperm (en). The embryo consists of the radicle (ra) and two pairs of cotyledons, the outer (oc) and the inner (ic). **E** Mature rapeseeds.

leaves and the fruit-producing branches. In this plant, the first siliques are already growing while the plant is still producing flowers at the end of the branches. The rapeseed silique (Fig. 2.1 B and C) consists of two halves that are divided by the replum, a thin layer in the centre of the silique. The seeds are maturing inside the silique (see Fig. 2.1 B, right), they are connected via the funiculus to the replum. Depending on the number, size and features of the seeds, the yield is determined [Ayt08; Che07; Die00].

The rapeseed (Fig. 2.1 D) exhibits a seed coat protecting the embryo during and after maturation and the embryo itself;the aleurone, a small lipid-rich layer, is located between them. The embryo is already equipped with the parts essential for starting a new life; it consists of two pairs of cotyledons (leaves), the inner and the outer, and the radicle (root). During maturation, the embryo grows inside the liquid and sucrose-rich endosperm that can still be detected in Fig. 2.1 D. Mature rapeseeds are shown in Fig. 2.1 E.

The **crops** wheat (*Triticum aestivum*) and barley (*Hordeum vulgare*) are two of the most cultivated cereals in Germany, with a per capita consumption of more than 65 kg in 2014 [Bun16]. Both cereals originate from wild grasses. The present-day cultivated species have been bred by humans since approximately 8,000 B.C. [Kis84].

The hollow stem of the **wheat** plant is enveloped by the long and narrow leaves, the

Figure 2.2: **A** Stem of a wheat plant with leaf and ear. **B** Section through a maturing seed, the embryo is located at the bottom tip. **C** Cross-section through a seed, the indentation is relatively deep. **D** Mature wheat seeds, the shape is round and short. **E** Cross-section through a wheat stem with a leaf wrapped around.

ear is located at the top of the stem (see Fig. 2.2 A and E). The seeds are produced in the ear, short photosynthetically active awns are attached to the seeds. Figures 2.2 B and C show sections through a maturing seed, its volume is mostly defined by the starch-containing endosperm. The small embryo in Fig. 2.2 B (bottom tip of the seed) contains the majority of the seed's lipid-reserves.

The seed's appearance is (compared to the barley seed) round and short. In Fig. 2.2 C, the relatively deep indentation of the seed is distinct.

The vascular bundles in the wheat leaf are visible in Fig. 2.2 E (light green spots), in the stem tissue they can be identified by the larger cell size.

The **barley** plant's structure is similar to the wheat plant (Fig. 2.3 A), noticable differences are the long awns attached to the seeds (Fig. 2.3 B) and the shape of the seeds, which are longer and thinner than the wheat seeds. Fig. 2.3 C shows sections through maturing barley seeds. The indentation of the seed is smaller than in the wheat seed.

The lipid-rich embryo is visible in the section of Fig. 2.3 C. It is located at the top of both seed halves. Here, two mature barley seeds are shown.

In a section through a barley stem, the vascular bundles in the stem tissue can be identified (dark green spots), in the leaf they appear as holes close to the dark green regions (Fig. 2.3 D).

Two representatives of the **legumes** are pea (*Pisum sativum*) and soybean (*Glycine max*). While both legumes are mostly cultivated for their high protein content, the soybean also possesses a high oil content.

Figure 2.3: **A** Barley plant **B** Stem of a barley plant, the awns are relatively long. **C** top: Cross-section through a seed, the indentation is relatively small. Bottom: Section through a maturing seed, the embryo is located at the top tip of the halves. **D** Cross-section through a barley stem with a leaf wrapped around, the vascular bundles are distinct. **E** Mature barley seeds.

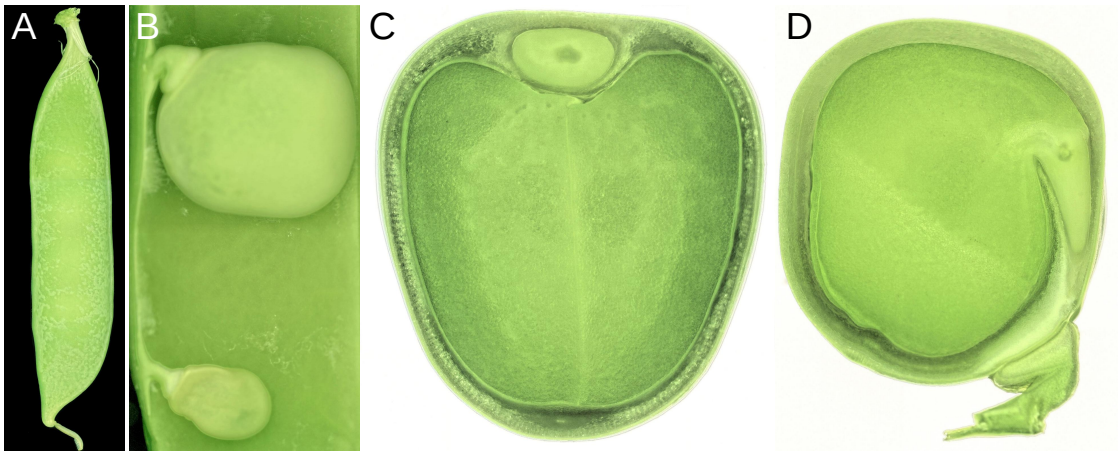

Figure 2.4: **A** Pod of a pea plant and **B** cross-section through a developing pod, showing two pea seeds connected vie the funiculus to the pod. **C** Cross-section through a pea seed, showing the seed coat, the radicle (top) and the cotyledon. **D** Cross-section along the radicle and the funiculus (bottom).

Fig. 2.4 A shows an intact pod of a **pea** plant. In Fig. 2.4 B a section through the pod is presented. The developing seeds grow inside the pod. Both are connected to the pod via the funiculus.
The section in Fig. 2.4 C shows the pea embryo, surrounded by the seed coat. The embryo is divided in the radicle (top) and the cotyledon, which is also visible in Fig. 2.4 D.

2.2 Lipid in Plants

Plants convert light through photosynthesis into chemical energy in the form of the complex organic compounds proteins, carbohydrates, and lipids. In the plant cell, carbohydrates are present in the form of polysaccharides (starch within the plastids, and cellulose in the cell wall). Storage proteins and lipids are accumulated in specialized inclusions, separated from the cytoplasm by a single layer membrane [Cha12].

2.2.1 The accumulation of lipids in plants

The energy density of the fully reduced carbon bonds present in lipid molecules is higher than that of the partially oxidized carbon bonds common in carbohydrate and protein molecules. Lipid molecules contain few carbon-oxygen bonds, making them weight for weight more energy dense than carbohydrates. Many plants have evolved the capacity to store energy in the form of lipids, particularly in the seed, since the lipid molecules require a smaller volume to store the equal amount of energy. In most plants the storage lipid content is present in the form of triacylglycerides [Hil93], but also waxes can be encountered [Sim16].
The lipid content of seed varies tremendously; it can reach up to 70 % in some nut species. For the germinating seed, a ready source of available energy is particularly important as a support until it has established its own photosynthetic apparatus. During the germination process, triacylglycerides are converted into carbohydrates through the uptake of water.
Mature seeds typically consist of three major components: carbohydrates (sugar), proteins and lipids, the residual moisture of seeds is low. In liquids, proteins and carbohydrates can be detected via NMR, while in dry seeds, the signal decays too fast for imaging applications.
The highest amount of lipid is found in the embryo, serving as an energy resource during the early growth phase, and in the aleurone, a thin layer directly underneath the seed coat, protecting the embryo like a barrier from external influences. Typically, the concentration of lipid is higher in the cotyledons than in the radicle.
Lipids are located in small lipid bodies in the plant tissue [Wan81], in these the lipid accumulates in liquid form. Thus, its relaxation times are long enough for high-resolution imaging, as will be further explained in Chap. 4.

2.2.2 The value of lipid imaging in plants

Destructive sampling has long dominated plant sciences and advances in technology have concentrated on tissue dissection and extraction methodology. The achieved levels of chemical resolution and sample throughput of these analytical methods are impressive, yet the reconstruction of a living environment from data derived from destructive sampling can be extremely difficult and is based on a set of suggestions [Bor12].
For the manipulation of oil content and the composition in vegetative and seed tissues of plant, various metabolic engineering strategies were developed [Nap14]. The progress in at least three different areas requires the implementation of a non-invasive measurement of lipids in plants:
Technical improvements in the productivity of established oil crops, in particular oil palm (*Elaeis guineensis*), soybean (*Glycine max*), oilseed rape (*Brassica napus*) and sunflower (*Helianthus annuus*), will increase the interest in a more detailed understanding of how the accumulation of lipids is regulated. The generation of such data prohibits a disturbing of the metabolism and structure of living plant tissue caused by sampling.
The promotion of new candidate plant species as lipid factories, especially targeting growing environments not used for arable crop production. This includes drought tolerant plant species such as *Jatropha curcas*, but also various algae which can be grown in a closed system [Hu08] and species such as *Camelina sativa* which produce unusual forms of lipids in their seed [Ban16].
Advances in molecular biology create opportunities to design entirely novel cropping systems: Plants could be engineered to accumulate lipids in their vegetative tissue, not only in their seed [And10; Dur11]. An alternative is the redirection of assimilates from their deposition (for example as starch or proteins) into the synthesis and deposition of lipids [Bar12]. The study of lipid synthesis and deposition will require a complete approach in order to evaluate the success of these strategies, especially the tracking of these processes in living tissue.
Driven by the medical sector, the need to develop the means to non-invasively detect lipids led to the elaboration of a number of NMR based protocols [Ber04]. The challenge is located in the adaption of those for plant applications.

Chapter 3
The basics of MRI

This chapter aims to provide the reader with a basic understanding of the principles of nuclear magnetic resonance imaging. After the introduction and explanation of the chemical shift, NMR pulse sequences suitable for chemical shift imaging are presented. A more detailed explanation of the basics of magnetic resonance imaging can be found in [Lev08; Bro14].

Preface

In this work all experiments were performed on ^{1}H-nuclei. For reasons of simplicity they will be denominated as spins. There are NMR applications for detection of other nuclei, such as ^{2}H, ^{13}C, ^{15}N etc. Whenever a measurement of that kind is spoken of, the so-called "X-nucleus" will be mentioned explicitly.

3.1 From spin to signal

The sample contains a large number N of nuclear spins that possess a magnetic moment $\vec{\mu}$. Their individual orientations in space are equally distributed in all directions [Han08].
In most experiments based on magnetic resonance, the sample is placed in the isocentre (the homogeneous area of the magnetic field $\vec{B}_0 = B_0\hat{e}_z$, created by the superconducting coils of the NMR scanner) of the magnet.
When looking at the behaviour of individual spins, the following property can be observed: each spin precesses around the magnetic field vector $\vec{B}_0$ with its individual Larmor frequency ω_L, which is dependent on the external field strength $\vec{B}_0$ and the spin's gyromagnetic ratio $\gamma = \gamma/2\pi$ (for protons: 42.57747892 MHz/T [COD17b] [1]):

$$\omega_L = -\gamma \cdot B_0 \tag{3.1}$$

[1] or $\gamma = 2.675221900 \cdot 10^8$ rad/s·T [COD17a] respectively

In the magnetic field of the NMR scanner, the sum of all magnetic moments, the magnetization $\vec{M}_0$ of the sample builds up and alligns parallel to the external field. The individual orientation of single spins is no longer equally distributed, a slight abundance towards the direction of the external magnetic field is present [Han08]. By looking at a large ensemble of spins (approximately $10^{23}/\text{cm}^3$ in water), the transversal components of the spins' magnetic moments cancel out, only the net magnetization $\vec{M}_0$ remains.
This magnetization is the basis for all consecutive NMR experiments. The NMR coil can, by applying adjusted RF- (radio frequency) pulses, tip the magnetization out of its initial state and thus create a transversal magnetization $\vec{M}_{xy}$ (orthogonal to the main magnetic field $\vec{B}_0$). At the end of the so-called excitation pulse, the transversal component of the magnetization vector precesses in the x-y-plane (which is orthogonal to the external field $\vec{B}_0$) with the Larmor frequency ω_L. The rotation of the magnetization induces a voltage in the NMR coil: the NMR-signal, also referred to as the FID or free induction decay (see Fig. 3.1).

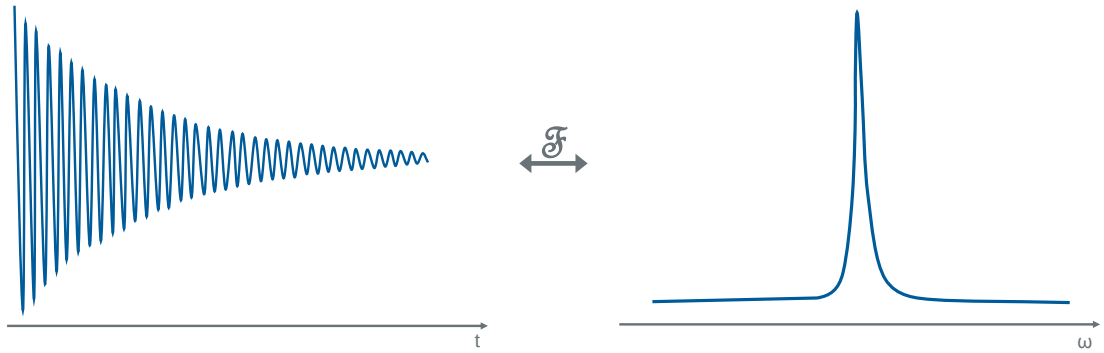

Figure 3.1: NMR signal: FID (left) in the time domain and spectrum (right) in the frequency domain. Both are linked via the Fourier transform.

A fast Fourier transform (FFT) of the FID signal acquired in the time domain reveals the spectral information about the sample: the spectrum. Its centre frequency is the Larmor frequency of the spins in the sample, the bandwidth of the spectral peak is proportional to their transverse relaxation parameters.
The proper selection of the centre frequency ω_{B_1} of the excitation pulse and its bandwidth BW_{B_1} determines the chemical compounds being subject of manipulation. The pulse's strength (B_1) and duration determine the flip angle of the magnetization.
The application of magnetic field gradients during the RF pulses leads to spatially dependent Larmor frequencies of the spins in the sample [Lau73], thus the RF pulses can selectively excite a predetermined slice within the object [Man73]. For the spatial encoding of the NMR signal within the excited slice, further magnetic field gradients

have to be applied. After the excitation pulse, phase encoding gradients encode the spatial information in the phase of the spins, during data acquisition, a read encoding gradient alters the frequency of the precessing spins depending on their location in the sample [Kum75]. In imaging sequences, the read gradient's strength remains constant while the phase encoding gradients are stepped through during the experiment. For the acquisition of a 128 $\times$ 64 matrix, 128 points are sampled during read encoding and 64 phase encoding steps are applied, one within each repetition interval TR. The sampled data is stored in the so-called k-space, a 2D-FFT applied on the k-space yields the associated image.

3.2 Relaxation

The precession frequency of an individual spin depends on two values: the constant gyromagnetic ratio γ and the magnetic field B_{loc} at the location of the spin (see Eq. 3.1). In an ideal experiment, the magnetic field is completely homogeneous and the interaction of the spins is zero, thus the magnetization vector would precess infinitely in the transversal plane.
From experimental observations the decay of the transversal magnetization vector with the simultaneous return of the longitudinal components to equilibrium are known. Both processes are caused by two factors: (1) the coherences between the spins are not infinite, they decay to zero, and (2) the populations of the spins in the two eigenstates are not time independent [Lev08].
The sample itself consists of a large amount of molecules at a certain temperature T, leading to various thermal motion processes of the molecules. Spins included in these molecules are subject to this thermal motion - they change location and orientation continuously. Each of the spins contributing to the magnetization $\vec{M}$ possesses its own magnetic moment $\vec{\mu}$. Thus, each spin also acts as a source of magnetic dipole field which is seen by the neighbouring spins, and since the spin is moving in space, its magnetic field is not static. These time-dependent dipolar fields are limited to spins in close vicinity, yet have a large contribution (called *non-secular*) to the relaxation of the magnetization [Kee11].
Additionally, local field inhomogeneities are present in most samples, e.g. caused by air inclusions in the tissue or caused by the dia- or paramagnetic ions (e.g. after application of a contrast agent). They are called the *secular* contribution to transverse relaxation.
For all spins, the experienced local magnetic field B_{loc} differs slightly from the external magnetic field B_0, in direction, amplitude and also over time.

3.2.1 Spin interactions

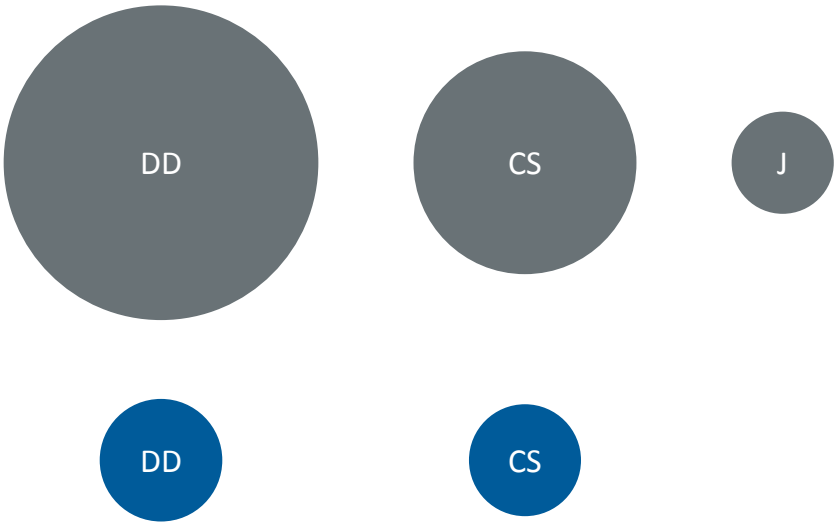

Figure 3.2: Overview of relative magnitudes of spin interactions, describing intramolecular (gray) and intermolecular (blue) components. Abbreviations: **DD** dipole-dipole, **CS** chemical shift, **J** J-coupling. Sizes according to [Lev08], p. 189

The non-secular variations of the local magnetic field B_{loc} originate from different effects and interactions of spins. In Fig. 3.2 the different relative magnitudes of each effect contributing to the transverse relaxation are represented. In the following the interaction mechanisms will be examined in more detail.

The **direct dipole-dipole coupling** describes the interaction of a spin's magnetic moment $\vec{\mu_A}$ with the magnetic moment $\vec{\mu_B}$ of a second spin. This interaction may be either intramolecular or intermolecular. The magnetic field created by spin A interacts with the magnetic moment of spin B and vice versa

The interaction energy of both spins $\hat{I}_A$ and $\hat{I}_B$ via dipole-dipole coupling can be represented by the following term [Lev08]:

$$\hat{\mathcal{H}}_{AB}^{DD}(\theta_{AB}) = d_{AB} \cdot (3\hat{I}_{Az}\hat{I}_{Bz} - \hat{I}_A \cdot \hat{I}_B) \tag{3.2}$$

d_{AB} is the secular coupling constant, given by:

$$d_{AB} = b_{AB}\frac{1}{2}(3cos^2\theta_{AB} - 1) \tag{3.3}$$

where θ_{AB} is the angle between the unit vector $\hat{e}_{AB}$ parallel to the line connecting both

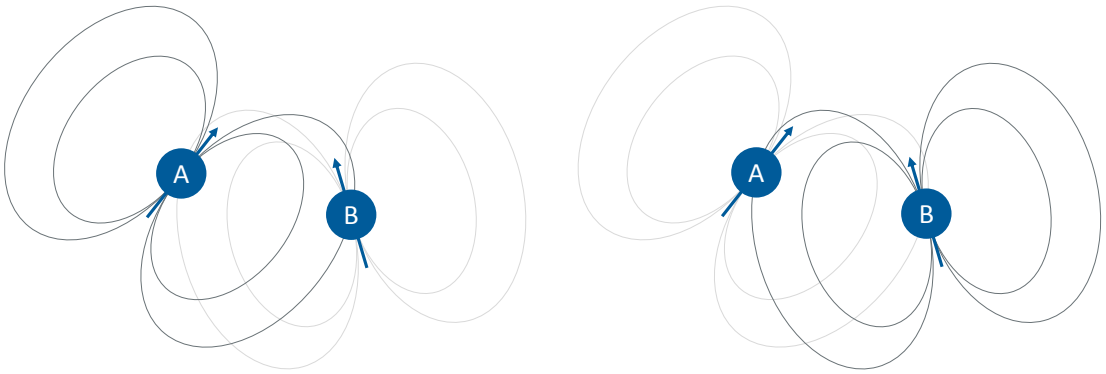

Figure 3.3: Dipole-dipole interaction of two spins $\hat{I}_A$ and $\hat{I}_B$. The interaction is mutual, the magnitude of the interaction between both spins is identical.

spins and the external magnetic field, i.e.

$$cos\theta_{AB} = \hat{e}_{AB} \cdot \hat{e}_z \tag{3.4}$$

and with the dipole-dipole coupling constant b_{AB}

$$b_{AB} = -\frac{\mu_0}{4\pi}\frac{\gamma_A\gamma_B\hbar}{r_{AB}^3} \tag{3.5}$$

which is independent of orientation of the spins. γ_A and γ_B are the gyromagnetic ratios of the nuclei, μ_0 the vacuum permeability and r_{AB} the distance between the spins. The energy of the two coupling spins is minimized when the orientation is parallel. The direct dipole-dipole coupling is used for estimation of the internuclear distance r_{AB} and also the geometric form of the molecule [Lev08].
The relaxation caused by the dipolar coupling is proportional to the square of the coupling itself, thus it goes as [Kee11]

$$\gamma_A^2\gamma_B^2\frac{1}{r_{AB}^6} \tag{3.6}$$

The secular dipole-dipole coupling is exactly zero, when the angle θ_{AB} between the axis through both spins and the magnetic field vector satisfies the equation [Lev08]

$$3cos^2(\theta_{AB}) - 1 = 0 \tag{3.7}$$

thus when its solution, the magic angle θ_{magic} is exactly [Lev08]

$$\theta_{magic} = arctan\sqrt{2} \cong 54.74° \tag{3.8}$$

This solution finds its application in the so-called magic angle spinning (MAS), where the sample is rotated at relatively high frequencies (up to 111 kHz [Bru17]) around an axis tilted by the magic angle θ_{magic} away from the magnetic field. This leads to a minimization of relaxation effects caused by dipolar coupling and thus maximizes the transversal relaxation times, which furthermore causes a narrowing of the spectral linewidths $b_{1/2}$ of the NMR active components [Fri13]:

$$b_{1/2} = \frac{1}{\pi T_2^*} \tag{3.9}$$

In isotropic liquids, the secular components of the dipole-dipole coupling average to zero, meaning it is uniform in all directions. This leaves the MAS technique an important tool for solid state spectroscopy.
The **J-coupling** (also scalar coupling) is an indirect dipole-dipole-coupling. It is transmitted via the electrons inside of a molecule. This coupling mechanism is strongly dependent on the number of chemical bonds between the coupling nuclei.
In contrast to the previously described interaction mechanisms, the J-coupling is independent of the molecular orientation and independent of the field strength, the interaction energy of the isotropic J-coupling is proportional to [Lev08]

$$\hat{\mathcal{H}}_{AB}^{J} = 2\pi J_{AB} \hat{I}_A \cdot \hat{I}_B \tag{3.10}$$

J_{AB} is the coupling constant, also referred to as the isotropic J-coupling or the scalar coupling, it is mutual for both nuclei ($\mathrm{J}_{AB} = \mathrm{J}_{BA}$). It is always reported in Hz, thus describing the distance of the two coupling peaks in a spectrum.
A detailed explanation of the origins and applications of the **chemical shift** can be found in chapter 3.3. In brevity, the electrons in a molecule produce a small local field at the nucleus. The spatial field variation induced by the chemical shift is anisotropic for most molecules, which means, it is dependent on the orientation of the molecule (chemical shift anisotropy) [Kee11].
In liquid molecules the tumbling rates are high enough to produce an average field for the NMR active spins, thus an average or isotropic chemical shift is observed. Nevertheless, for a single spin, its local magnetic field B_{loc} is not time-dependent, this effect increases the loss of coherence after the excitation pulse and thus causes transversal relaxation.

3.2.2 The transverse relaxation

The above-mentioned effects all influence the local magnetic field $\vec{B}_{loc,i}$ of a single spin $\hat{I}_i$. This leads to a decrease of the precessing magnetization's coherence, since the temporally and spatially varying magnetic fields affect the spins' Larmor frequency directly (Eq. 3.1).
The signal acquired immediately after an excitation pulse is called free induction decay (FID), as seen in Fig. 3.1. The overall decay of the transverse magnetization M_{xy}, thus the loss of coherence, over time t can be summarized by [Kee11]

$$M_{xy}(t) = M_{xy}(0) \cdot e^{-t/T_2^*} \tag{3.11}$$

with the transversal relaxation time T_2^*. In some cases the transversal relaxation rate $R_2^* = 1/T_2^*$ is used.
In detail, the transversal relaxation time constant consists of two components [Kee11]:

$$\frac{1}{T_2^*} = \frac{1}{T_2} + \frac{1}{T_2'} \tag{3.12}$$

whereby T_2 describes the internal field variations, which are related to the local (and random, *non-secular*) time-dependent field variations, and T_2' is related to the external influences, such as the field inhomogeneities (*secular*).
The effects caused by the random field fluctuations are irreversible, as discussed in section 3.2.1. The static contribution of the field inhomogeneities is constant over time, enabling the user to compensate this signal loss by application of suitable pulse sequences (as for example the spin echo, discussed in section 4.2.1).

3.2.3 The longitudinal relaxation

The previously described local fields vary randomly in their magnitude and orientation, interacting with the individual spin's orientation. The spectral density function $J(\omega)$ describes the amount of motion at a certain frequency experienced by a spin [Kee11]:

$$J(\omega) = \overline{B_{loc}^2} \cdot \frac{2\tau_c}{1 + \omega^2 \tau_c^2} \tag{3.13}$$

If the spectral density contains frequencies at the Larmor frequency ω_0, the direct dipolar interaction between the spins causes them to interact and change orientation. The correlation time τ_c describes the average amount of time required for a spin to

achieve an orientation 1 radian away from its starting position [Kee11].
Over time, the bulk magnetization is driven back to the equilibrium state $\vec{M}_0$ by the transverse components of the spectral density.

3.2.4 Image contrast

For the analysis of an MR image, the applied sequence parameters always have to be regarded. Each setting of imaging parameters (e.g. the repetition time TR and the echo time TE) can suppress or highlight signal from compounds, depending on their relaxation rates.
In MRI, three major contrasts or weightings (and various compositions of them) can be adjusted:

- The $\mathbf{T_2}$ **weighting** is induced by a relatively long TE, thus enabling the spins to interact (T_2 relaxation). After this time interval, regions with high spin-spin interaction (short T_2, dark) and with low spin-spin interaction (long T_2, bright) show a high contrast in the acquired image.

- A $\mathbf{T_1}$ **weighting** is achieved by reducing TR. Regions with different T_1 values differ in their relative signal intensity, since their individual magnetizations are driven in different steady states by the excitation pulses. A T_2 weighting is minimized by setting the shortest possible echo time.

- **Proton density weighting** reveals information about the spin density in the sample, thus both previously described weightings have to be avoided: This is achieved by minimizing the echo time and maximizing the repetition time, typically in the range of 2-5 times the sample's T_1 time.

While in living plant samples, a T_2 weighting can help separate different tissues, in dry objects (seeds) the relaxation times are typically relatively short. For avoidance of signal loss, the echo time and thus the T_2 weighting is usually minimized.
For improvement of the SNR in the microscopic images, signal averaging has to be applied. In order to avoid overlong measurement times, the repetition time TR is usually set in the range of 1-2 times TR, thus inducing little or no T_1 weighting.

3.3 The chemical shift

The assumption, that all ^{1}H-nuclei possess the same Larmor frequency, only holds true in first approximation. In different substances (e.g. water and lipid), the resonance frequencies of the spins are not equal.

3.3.1 Origin of the chemical shift

The origin of the peaks is the direct molecular environment of the observed nucleus, mostly caused by the presence of electrons. The electrons in a molecule contribute to local variations of the magnetic field. Currents induced by the external magnetic field B_0 in the electron cloud of the molecule generate a magnetic field $\mathrm{B}_{ind} = \delta^A \cdot \mathrm{B}_0$. Its strength is directly proportional to the external field.
The chemical shift tensor δ^A is a 3x3 matrix of real numbers, it takes into account that the external field and the induced field have different orientations [Lev08]. In isotropic liquids, the tensor δ^A is isotropic, mostly being simply referred to as the chemical shift. Its principal values δ^A_{XX}, δ^A_{YY}, and δ^A_{ZZ} are identical.
The electronic contributions to the magnetic field can be of diamagnetic nature: if the electrons are in the ground state (preferably s-electrons) or of paramagnetic nature, if they are in excited electronic states. Since most electrons occur paired in the electron shells, their paramagnetic contributions cancel out and only the diamagnetic property remains. This is the reason for the attenuation of the external magnetic field at the location of the nucleus, thus resulting in an altered Larmor frequency, see Eq. 3.14.
Usually, this frequency shift is represented in Eq. 3.1 by including the shielding constant σ in the term for the local magnetic field B_{loc}=B_0·(1−σ) [Fri13]

$$\omega_L = -\gamma B_0 \cdot (1 - \sigma) \tag{3.14}$$

The parameter σ is independent of the external magnetic field. For better handling in calculations, its unit is given in ppm (parts per million).
When looking at the individual Larmor frequencies of two different substances, one can observe that the higher the magnetic field strength used for magnetic resonance experiments, the larger the Larmor frequency differences between the substances become. Even when looking at a single substance (lipid), several NMR peaks may be distinguished within the NMR spectrum [Vig03].
The typical value for the chemical shift between water and fat (to be exact: the $(\mathrm{CH}_2)_n$ components of the fatty acid in the lipid molecule, see Fig. 3.4) equals 3.5 ppm [Cal93]. This means, that at a magnetic field strength of 1.0 T and thus a Larmor frequency of 42.58 MHz, the maximum of the lipid signal is shifted by 149 Hz from the maximum of the water signal.
The effect of the chemical shift becomes even more distinct, the higher the magnetic field strength is: at 17.6 T the chemical shift $\Delta\omega$ between water and fat rises to approximately 2,600 Hz. This enables the chemical selective investigation of objects containing more than one compound (e.g. water and lipid), and thus the acquisition of chemical

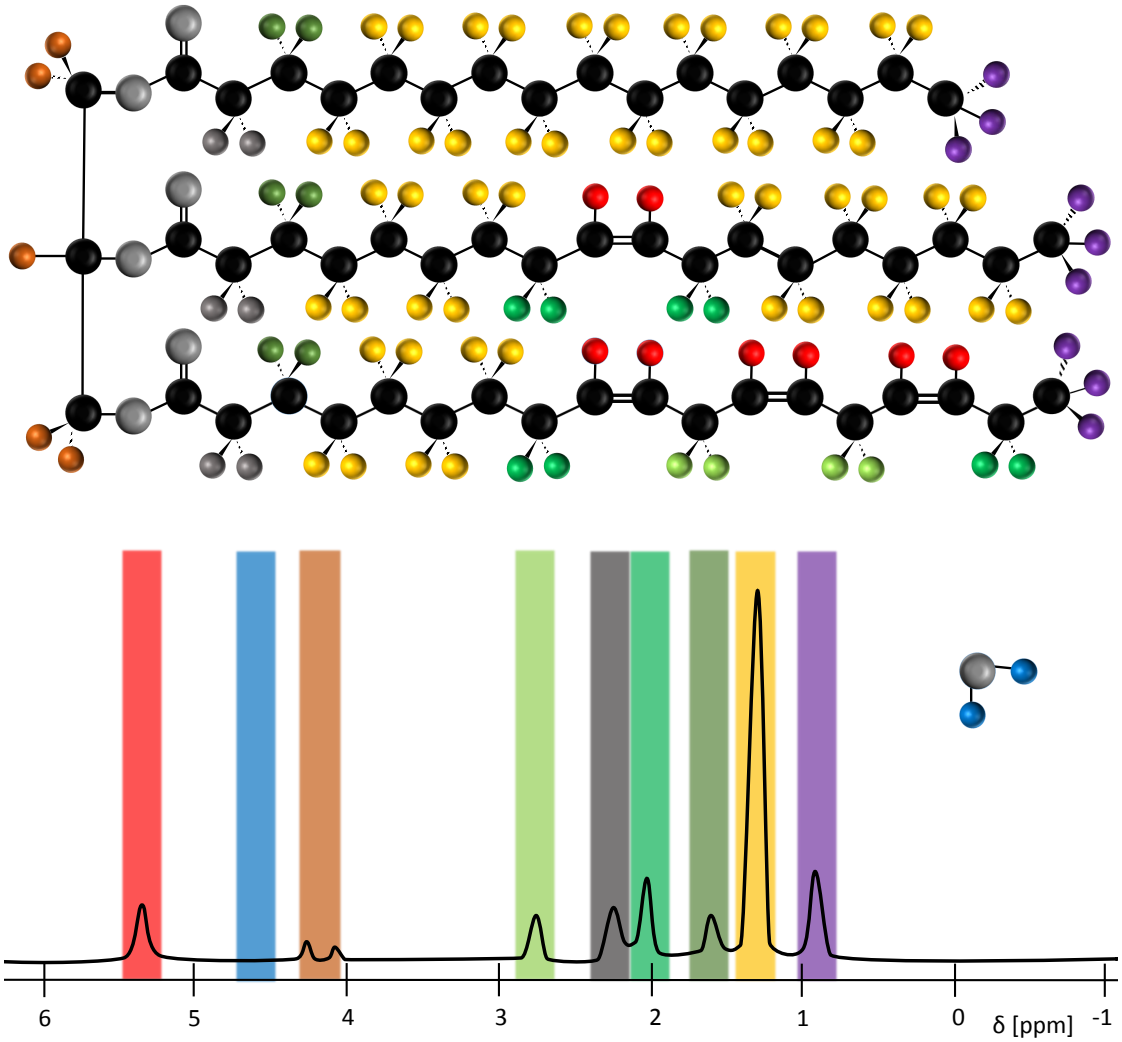

Figure 3.4: **Top**: Schematic visualization of the TAG molecule (lipid) and a water molecule. The strength of the shielding effect of the electrons in the molecule is dependent on the electron distribution. Thus the resonance frequency of the individual ^{1}H nuclei within the molecule differs.
Bottom: NMR spectrum of vegetable oil. The individual resonance peaks are highlighted as the molecular components in the molecules. The resonance peak of the water molecule would appear at position -4.7 ppm (blue).

shift selective datasets.

When an NMR spectrum is acquired, the convention is that the axis of the chemical shift is assigned from right to left. The reference for each measurement is the frequency of the TMS molecule (tetramethylsilane) [Lev08], leading to the definition of the absolute chemical shift δ:

$$\delta_{substance} = \frac{\omega_{substance} - \omega_{TMS}}{\omega_{TMS}} \tag{3.15}$$

This value is used to distinguish several NMR-active components.

3.3.2 The chemical shift in plant MRI

Plants mostly consist of water and, to some extent, they contain lipids. These are, as in the human body, primarily a storage compound reserved for future processes requiring a large amount of energy. Especially in oilrich seeds (such as for example rapeseed seeds, olives, and soybeans), these lipids are present in large quantities. Two NMR spectra, acquired in soybean oil and a soybean seed, are shown in Fig. 3.5.

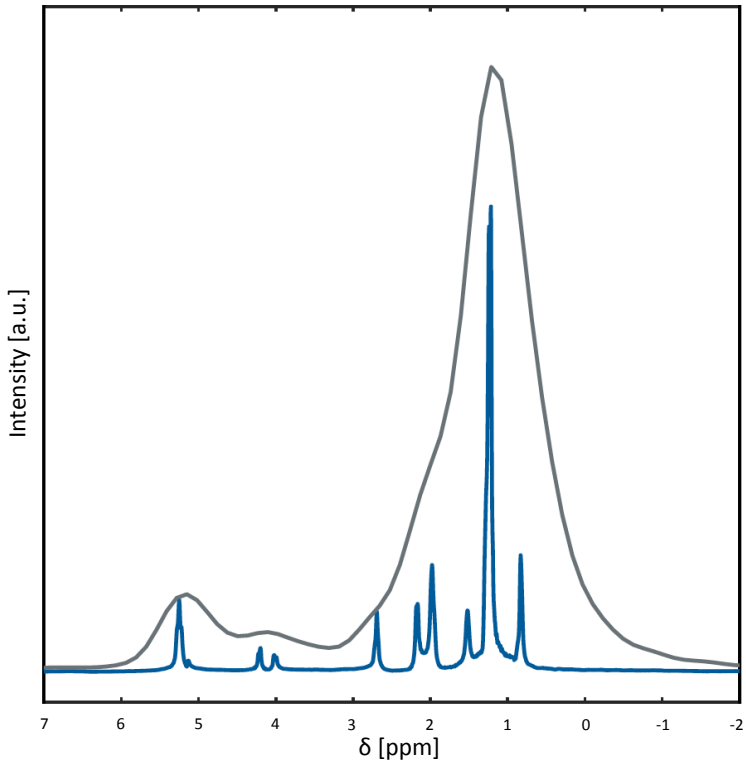

Figure 3.5: NMR spectra of soybean seed (gray) and soybean oil (blue). The local inhomogeneities in the soybean seed broaden the linewidths of the individual peaks. Amplitudes were scaled for better visualization.

In each spectrum, the different molecular components at certain chemical shifts provide a semi-quantitative visualization of their portion within the molecule. The resonance peak of the water protons can be found at -4.7 ppm, the protons attached to the $(CH_2)_n$-components are found at -1.2 ppm. Around this lipid peak, further components of the TAG molecule are located: The protons attached to the CH_3-group of the fatty acid and also the protons close to those being attached to a double-bond in the alkene-chain

[Vig03], see Fig. 3.4.
In the range of the increased Larmor frequencies (related to the water resonance) the resonance of the protons attached to a double-bond HC=CH can be found.
Depending on the homogeneity of the sample and the relaxation parameters, the individual lipid peaks can be merged into one single, broadened peak. In this case, a further distinction of the components is inhibited, see Fig. 3.5 and [Bor13a].

Chapter 4
Plant Imaging via MRI

The major challenges of plant NMR imaging are explained in this chapter. Since the focus of this work was the investigation of the lipid distribution and metabolism of plants and seeds via MRI, the major adaptions and developments for the detection of lipid in plants within the last decade are presented to provide a detailed overview of the current state of the art of lipid imaging.[1]

4.1 Challenges for MRI posed by plant tissue

The focus of the development of nuclear magnetic resonance still lies on clinical diagnostics, although MRI is gradually finding uses in food science [Can16]. Plant biology is a relatively new field for both MRI analysis and associated computer visualization [Bor12; VA13]. The monitoring of the entire developmental cycle is an application unique to plants.

4.1.1 Biological challenges

The means of acquiring MR datasets is similar for both plant and non-plant subjects, yet a direct application of most protocols developed for animal/medical subjects on plants is not possible.
First, plants are **immobile** organisms, requiring the NMR user to either bring them into the MR scanner or the build an NMR spectrometer around the plant.
The demand of living plant objects for the continuing support with **light and water** has to be considered for the experimental setup. As long as the plant is supported with those, it will remain intact. Hereby the plant must remain capable of respiration and in some cases of photosynthesis. Otherwise, dehydration may occur which can cause a loss of tension in the plant tissue during the experiment, which leads to an undesired movement of the plant sample.

[1] This section refers to the article "The potential of nuclear magnetic resonance to track lipids in planta" previously published in Biochimie 130 (2016): 97-108 by Munz et al. [Mun16]

The **metabolism and growth** of the plant is significantly slower than in humans, thus functional measurements (e.g. flow) are planned on longer time scales (hours or even days). Unfortunately, growth and movement can lead to a failure of the experiment, if these occasions are not considered. Plant samples have to be fixated in order to suppress the possible movement, caused by slow descent due to gravity or the previously mentioned dehydration.
The **diversity** of plants in size and shape requires the adaption of the NMR scanner's hardware to the measured object. Small seeds in the size of approximateley 1 mm have to be measured in small coils, while large fruits with diameters in the range of several 10 cm can be measured with NMR coils designed for human applications. The choice of the NMR spectrometer used for the experiment is also dependent on the sample size, since the NMR coils of ultra-high field scanners typically have relatively small diameters, see Chap. 10.4.2.
A major difference between the human and the plant organism can be found in the **chemical composition**: Plant tissue contains chlorophyll which is required for the photosynthesis. Its product, the sucrose, is the main solute in the plant's vascular system.
In the plant, a large amount of **dead tissue** is present, e.g. in the stem as a supportive tissue (chlorenchyma) or in seeds as the seed coat. Within lengths in the submillimetre range the tissue composition changes rapidly and in addition, many plant tissues contain a significant intracellular space filled with either air or fluid. The homogeneity of the magnetic field suffers from the air inclusions in the tissue, which can give rise to artifacts during NMR experiments [Cal94].

4.1.2 MRI related considerations

A high flexibility is provided by chemical shift protocols to the experienced user, but where the presence of more than one NMR visible component is ignored, **chemical shift artifacts** can compromise image quality. The water and the lipid images overlap in the frequency encoding direction (read direction), the lipid signal is slightly shifted, as can be seen in several publications [Hon09; Bor13a; Maz15] and [Mun16].
The relatively long T_2 value associated with liquid compounds leads to high intensity MR images in tissues which have a high water content. As a result of high spin-spin interactions and a high longitudinal relaxation rate, the imaging of tissues with a low water and/or low lipid content is hindered by a too **rapid decay** in signal. For imaging these tissues, short echo time sequences and signal averaging may be necessary.
The aforementioned **heterogeneity** of the plant is also present on the macroscopic

scale, for instance in the fruits of crop plants. Siliques are characterized by a distinct structure - their seeds are attached to the septum, the inner wall in a silique. While the pod tissue protects the maturing seeds from external influences, the seeds themselves are surrounded by air. Thus, the measurement of a complete silique is impeded by its structure's heterogeneity which strongly deforms the local magnetic field B_{loc}.
The **shim procedure** before each experiment is supposed to compensate this influence, yet in measurement of siliques, this tool reaches its limits. Chemical shift selective measurements of seeds within a silique can be performed, yet are restricted to relatively small regions along the elongation direction of the fruit.
Chemical shift selectivity is achieved by longer RF pulses, yet, when elongating the echo time, the resulting image contains a **reduced SNR**. Therefore, the bandwidth of the pulses has to be set in a rational range, mostly 500 to 2,000 Hz, in order to keep the echo time as short as possible.
In general, magnetic resonance imaging of plants is limited by the heterogeneity of the tissues. Adjusted pulse programmes can compensate influences of local inhomogeneities, e.g. air inclusions, but some tissues require advanced imaging techniques. When the combination of NMR hardware, NMR protocol and the object of interest are well-considered, in vivo resolutions close to the cellular level have been reached in lipid imaging (6 μm in-plane resolution in the *M. flabellifolia* plant [Sch03]).

4.2 Plant imaging: MRI pulse sequences

For the successful MR imaging of plants the diligent selection and adaption of pulse sequences to the sample is required. For coping with the challenges posed by the inhomogeneous tissue of plants, the spin echo sequence is usually the method of choice for standard imaging.

4.2.1 Spin echo

In Fig. 4.1, an example for a slice-selective spin echo sequence is provided, recognizable by the gradients in slice direction during application of the pulses. The initial excitation pulse, usually a 90° pulse, tips the magnetization (of the selected slice) into the transversal plane. After the end of the pulse, the precessing magnetization dephases (FID) with the time constant T_2^*, caused by the inhomogeneities in the sample. This FID is not acquired, but for reasons of completeness, it is mentioned.
The rephasing component of the slice selection gradient is supposed to compensate phase effects on the magnetization induced by the gradient.

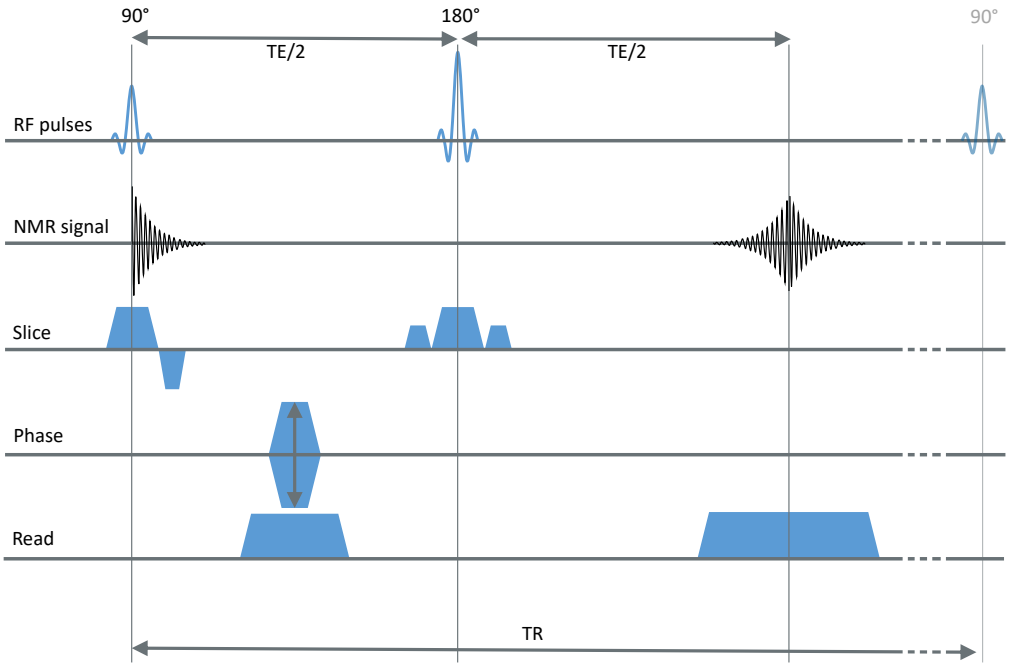

Figure 4.1: Scheme of the 2D spin echo sequence. Both RF pulses are applied in combination with a slice selection gradient. The induced NMR signals are shown, although only the spin echo at time t=TE is relevant. For image acquisition, a phase encoding gradient and a read gradient are necessary. The latter gradient, as well as the slice selection gradients, require a dephasing component.

During the interval TE/2, a phase gradient (in phase direction) is applied, encoding the magnetization with locally dependent phase information required for image reconstruction.
At the time t=TE/2, a refocusing pulse (180°) is applied, inverting the complete magnetization of the sample. Notably and in contrast to the gradient echo sequence, for each spin the phases induced by local field inhomogeneities are also inverted by the pulse.
At the time t=TE, the spin echo can be acquired, the gradient required for read encoding (and its dephasing component for compensation of phase effects) is applied in such a way, that at the time of the echo formation, the phase induced by the gradient is zero. A signal loss due to spin-spin-interactions has appeared, but the signal intensity of the echo depends on the transversal relaxation time constant T_2, which is always larger than or equal to the previously mentioned time constant T_2^*.
This sequence is repeated for each phase encoding step with an individually calculated phase gradient. Three-dimensional datasets require a second phase gradient applied orthogonally to the first phase gradient and the read encoding gradient.

4.3 Tracking lipids in plants via nuclear magnetic resonance

The focus of this work was the detection and localization of chemical compounds in plants, especially referring to the separation of the almost omnipresent water from the lipid. As will be shown in chapters 5 and 6, the adjustment of the RF pulses is required for the acquisition of chemical selective datasets. Over the years, the variety of MRI applications in lipid imaging in plants has grown, a complete overview cannot be given in this work. Nevertheless, the following sections provide the reader with a review of the major advances and application in plant lipid imaging performed in the last decade. A more detailed review was published under the title "The potential of nuclear magnetic resonance to track lipids in planta" in Biochimie 130 (2016): 97-108 by Munz et al. [Mun16]

The application of magnetic resonance imaging on plants started in 1986, more than a decade after the first publications of MR imaging [Lau73; Man73]. First experiments of plant imaging concentrated on the water distribution in root systems of *Vicia faber* under undisturbed and light stress conditions, the uptake of water by using a contrast agent was also observed, the in-plane resolution was 600 μm [Bot86]. Further experiments also focused on the water content in roots of *Pelargonium hortorum*, the three-dimensional images were acquired with an in-plane resolution of 100 μm [Bro86]. The changes in pixel intensity during the period of relatively rapid transpiration were assigned to changes in water content, the authors also discussed the possibility of a change of the relaxation parameter T_1 instead of spin density ρ.

In the following year, in measurements of stems of *Pelargonium hortorum*, T_1-values and spin density ρ in transpiring plants were determined, differences in proton density and apparent spin lattice relaxation time T_1 enabled the distinction of tissues within the stem [Joh87]. The 3D measurement reached a resolution of 100 μm in-plane with a slice thickness of 1,250 μm.

An improvement of resolution (50 μm in-plane, slice thickness 560 μm) was reached on the imaging of seeds, roots and stems of maize (*Zea mays*) [Con87]. Within the experiments, uptake of a contrast agent (Mn^{2+}) was monitored, enabling the detection of the xylem vessels in the root. The illustration of structural changes in a germinating mung bean (*Phaesolus aureus*), first implications to the separation of the compounds water and lipid via chemical shift selective imaging were given.

4.4 Applications of NMR spectroscopy to plants

The requirements for a successful isolation of the lipid signal from the "background" signal necessitates the knowledge of the overall constitution of the sample in the NMR experiment. This information can be acquired non-invasively after the setup of the sample in the NMR scanner with spectroscopic NMR methods.
NMR Spectroscopy started after the discovery of the NMR effect by Bloch and Purcell [Blo46; Pur46]. Since then a variety of spectroscopy sequences have been developed. All spectroscopic sequences have in common: excitation pulses with relatively high bandwidth that manipulate the magnetization and that signal is acquired without a gradient required for imaging. Before excitation and signal acquisition, various preparations and manipulations of the magnetization are possible. While their description fills complete books [Fri13], a closer look on basic spectroscopic NMR applications in regard to plant imaging is given in the following sections.

4.4.1 Global spectroscopy

The optimal choice for deriving the chemical constitution of a sample is global spectroscopy. The experiment can be performed within a short period of time and provides the information about the NMR active compounds present in the sample. An estimation of the global relaxation times can also be performed when sequence parameters such as TR and TE are modified. This information is the basis for the selection of appropriate NMR protocols for further measurements. The settings of the excitation pulse determine the content of the global spectrum, which can show both, water and lipid, or water only and lipid only. Further components, such as sucrose and amino acids, typically are not visible in the globally acquired spectrum.
The experimental design enables the detection of several nuclei, recent applications have featured ^{1}H NMR [Vig03; Sat09], ^{13}C NMR and ^{31}P NMR [Day08].
A system for assessing the quality of oilseeds, based on a continuous wave free precession ^{1}H NMR sequence, was proposed several years ago [Col07]. Hundreds of large and heterogeneous seeds carrying a range of lipid content, from soybean (*Glycine max*) (22% lipid) through physic nut (*Jatropha curcas*) (35%) and peanut (*Arachis hypogaea*) (45%) to the macadamia nut (*Macadamia integrifolia*) (65%) could be monitored. The non-invasive quantification of lipids of up to 24,000 seeds per hour was enabled by a short measurement time of ca. 150 ms. The only limiting factor for analysis of differently sized seeds was the size of the NMR coil (in this case 18 mm). In principle, this method does not require a high field or large bore magnets, and could be easily adapted to measure classes of compounds other than lipids in either seeds/fruits or

food/feed.
With pulsed-field gradient (PFG) techniques, where a short timed pulse of spatially-variable field intensity is applied, the estimation of the diameter of oil bodies harboured by a range of seeds by assessing the extent of diffusion of lipids was enabled [Gro15]. The determined values agreed well with conclusions based on optical methods.
The study of lipid accumulation and composition in the *J. curcas* seed via PFG-methods revealed various free fatty acids, fatty acid methyl esters and triglycerol esters, along with small quantity of sterols [Ann08]. The initial stage of lipid accumulation and an estimation of the proportion of the different compounds present could be defined.
The potential of ^{13}C NMR was demonstrated in an in vivo metabolite profiling experiment carried out on conifer seeds [Ter05a]. An accurate quantification of the seeds' lipid content and the fatty acid composition of the major storage lipids present was provided. During both germination and early seedling growth, free amino acids (arginine and asparagine) were detectable. The prediction of seed viability and the detection of the presence of developmental aberrations in conifer seed was successfully performed by ^{1}H and ^{13}C NMR.
When the sample is a solid material, the magic angle spinning (MAS) NMR technique is a frequent choice. In highly heterogeneous structures (such as seeds), the NMR spectrum tends to comprise a number of broad, overlapping spectral lines, thereby obscuring the isotropic chemical information. Magnetic anisotropies within the sample are dealt with in MAS NMR by rotating the sample at high frequencies, see Chap. 3.2.1. This leads to a reduction of the line broadening and an improvement in spectral resolution. Spinning frequencies typically lie in the range a few hundred to 70,000 Hz [Lev08].
Differentiation of *Arabidopsis thaliana* wild type plants with a cellulose-deficient mutant was enabled by the application of ^{1}H and ^{13}C MAS NMR [Whe15].The identification of signal from molecules with restricted diffusion, such as lipids, was carried out on basis of diffusion-weighted spectra. The acquisition of two dimensional HSQC (heteronuclear single quantum coherence) spectra delivered information about the molecular connectivity between ^{1}H and ^{13}C, and provided a metabolite fingerprint. A comparison of the fatty acid composition of the wild type vs mutant seeds could be produced by combination of these methods, and also revealed differences in the way in which stored energy was processed. The use of further NMR methods (e.g. 1D ^{13}C Cross Polarization and 1D solid-state ^{13}C NMR spectroscopy, both for detection of the rigid compounds such as starch, cellulose, and lignin), the identification of differences in the content of glutamine, phenylalanine, starch, lignin, methanol, and nucleic acid

was enabled.

4.4.2 Localized spectroscopy

Plant samples usually consist of several distinct components and organs; a seed consists of seed coat, endosperm and embryo. Each organ influences the seed's size, composition and metabolism/growth, and each also has its specific set of functions. It is of both fundamental and applied interest to observe the behaviour of these discrete structures in vivo (e.g. distinct pattern of lipid accumulation in embryo and endosperm) during the course of the seed's development, germination and response to environmental influences. The necessary data cannot be supplied by global spectroscopy, instead, the selective excitation of a defined portion of the sample is required for a localized spectrum.

Single pulse

The single pulse sequence consists of one single excitation pulse and an immediately started acquisition window for the NMR signal. The parameters of the pulse (e.g. bandwidth, pulse shape and flip angle) can be adjusted. The resulting FID contains the spectroscopic information about the sample. Usually, this sequence is used for a simple overview of the sample, regarding its chemical composition.
In the endosperm of a pea seed (*Peasum sativum*), several metabolites, such as sucrose, alanine, glutamine and lactate could be detected [Mel09b]. In further experiments, these metabolites could be further quantified.

PRESS: Point-resolved Spectroscopy

For obtaining a localized spectrum from a sample, the point-resolved spectroscopy (PRESS) method is commonly used [Bot84]. In this method, the signal originates from the intersection (typically a cube) of three orthogonal slices. After the excitation of a single slice in the sample, the following two refocusing pulses are applied to each single slice orthogonal to the previous slice(s).
The PRESS method is applied when a spectroscopic comparison of different regions in a sample is desired and the measurement time has to be kept short, in contrast to Chemical Shift Imaging.
By applying Point-resolved spectroscopy (PRESS), consisting of one slice excitation pulse and two orthogonal slice refocusing pulses, voxel-specific spectra can be acquired. This method enabled the tracking of lipid content in the embryo of the areca palm fruit

(*Areca catechu*) and demonstrated its increase over time [Sri16]. Simultaneously, data regarding the water, sugar and alkaloid content of the seed were acquired.

Chemical Shift Imaging (CSI)

Unlike the other imaging sequences, Chemical Shift Imaging (CSI) relies on phase encoding only [Poh97] (in combination with a slice selection gradient during the pulse application), as is shown in Fig. 4.2.

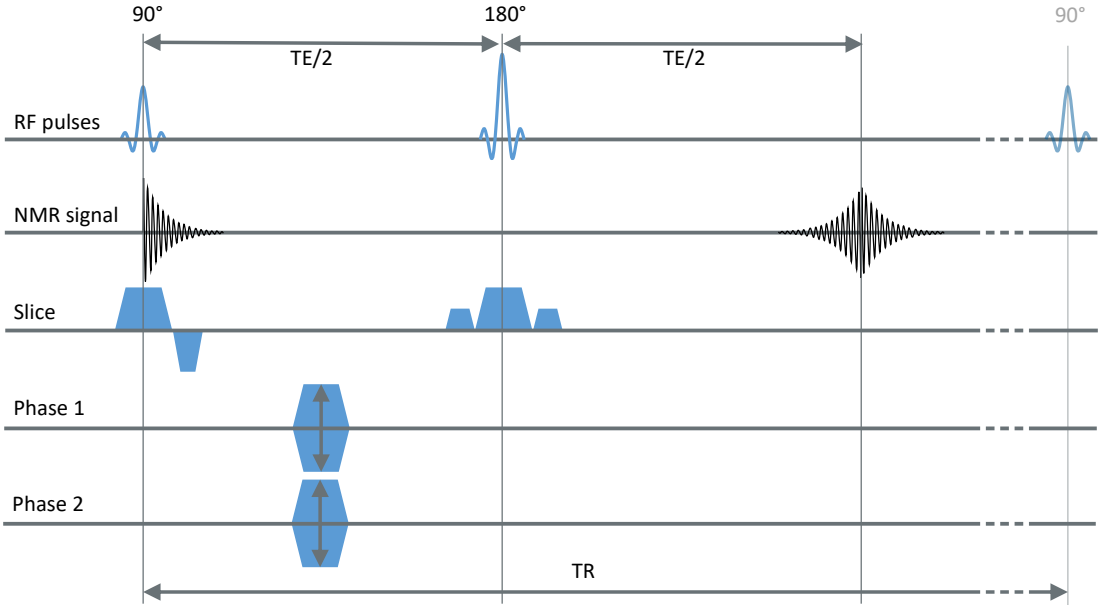

Figure 4.2: Scheme of the CSI sequence, which relies (except for the slice selection) on phase encoding only. The course of the pulse programme is in this case analogue to the spin echo sequence.

In the reconstructed images, each voxel contains the NMR spectrum of said voxel. This enables the user to decide after the acquisition of the dataset, whether to select a single voxel (or region) and analyze the associated spectrum - or to select a spectral region in all spectra and analyze the associated distribution within the sample.
This advantage is paid for with a highly increased measurement time, typically the acquisition of a 2D CSI dataset with a matrix of 128 x 64 is as time-consuming as a 3D spin echo dataset with a matrix of 128 x 128 x 64; if a repetition time TR of 2000 ms is assumed, the duration is 4 h 33 min for both experiments.
Chemical shift imaging can be performed in two acquisition modes: in the “FID mode”, the signal is acquired after the excitation pulse with a hardware-dependent delay. Here, the signal is T_2^*-weighted.
In the “spin echo mode”, a second refocusing pulse generates an echo which then is

acquired. A CSI experiment on plants benefits from utilization of the "spin echo mode", since at the time TE the signal loss caused by the T_2^* relaxation is compensated.
On plants, several experiments were performed with the CSI sequence: Quantification of metabolites in the endosperm of pea seeds was achieved by using a CSI sequence in combination with a water suppression scheme. A gradient of sucrose within the seed's embryo, falling from the inner regions down to the outside was detected [Mel09b]. In the endosperm vacuole, the distribution of the metabolites sucrose, alanine and glutamine was homogeneous.
A CSI sequence adjusted to measure the allocation of ^{13}C-labelled sucrose enabled the visualization of the distribution of the sucrose within a barley caryopsis [Mel11]. The labelling front's velocity inside the imaging plane was determined to be 145 μm/h in dorso-ventral direction and 72 μm/h in lateral regions of the pericarp. An anatomic ^{1}H image of the seed was captured by using a double-resonant coil.
The monitoring of a barley grain's development via CSI enabled the generation of separate images for water, lipids and sugars [Gli06]. At a series of developmental stages and focused on specific regions of the caryopsis, NMR spectra were captured. They showed the accumulation of lipid in the embryo over time, while the content of soluble carbohydrate declined in the endosperm. It was possible to model the distribution of water and lipids over the course of the grain's development, by combining the data with three-dimensional images illustrating the local water content.

4.5 Chemical shift selective imaging of plants

When the detailed chemical information about the NMR spectrum is not available or required, the Chemical Shift Selective Imaging (CSSI) method can provide a high-resolution dataset from the compound of interest within a moderate measurement time. In contrast to the previously described spectroscopic sequences, the chemical shift selective imaging (CSSI) relies on the setting of the excitation and the refocusing pulses. They are adjusted in such a way that only the spins of a chosen chemical compound (e.g. water or lipid) are selected.
This technique requires a sufficiently large chemical shift between the desired compound's spins and the spins of other present compounds. For this reason, this imaging technique is usually restricted to high field MR experiments. A requirement of the chemical selection is the absence of slice selection gradients, thus global RF pulses have to be used. A read encoding gradient is applied during data acquisition, which separates this imaging technique from the localized spectroscopy techniques.
3D CSSI datasets of a complete seed or a large portion of a plant can be imaged in

approximately the same time as a 2D CSI dataset with similar in-plane resolution, first applications in plants started in 1991 [Pop91]. Chemical shift selective imaging

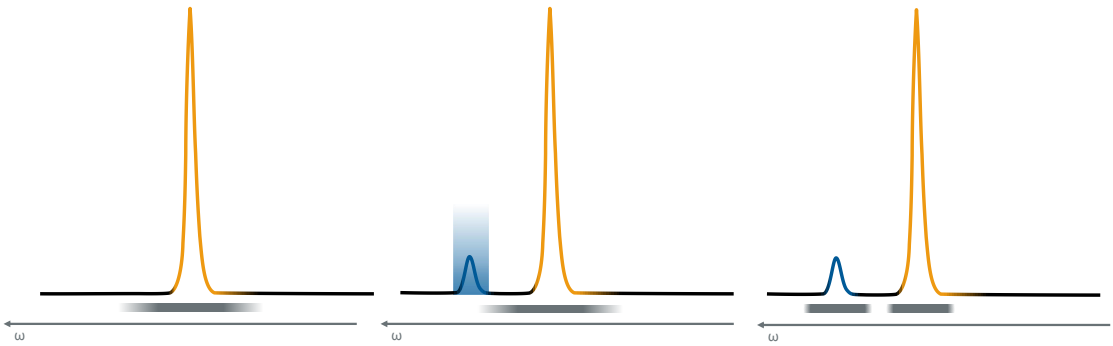

Figure 4.3: Scheme of CSSI techniques:
Left: Only one component is NMR active, the pulse bandwidth (gray) can be chosen freely. In this case, no preparation is required.
Centre: Solvent suppression. The undesired component (blue) is subject to a solvent suppression scheme (highlighted blue) before excitation of the desired component is performed.
Right: Interleaved CSSI. Both substances (blue, orange) are excited in an interleaved acquisition scheme. For avoidance of combined excitation, the bandwidths of the pulses have to be diligently adjusted.

(CSSI) can be achieved with a variety of pulse sequences, the most important imaging schemes, visualized in Fig. 4.3, are exemplified in the following sections.

4.5.1 CSSI without preparation module

A simple way of detecting and imaging one component only can be achieved when the other NMR-active components are present in small amounts or not detectable due to short relaxation times (Fig. 4.3, left). In dry plants, bound water does not contribute to the resulting images since its relaxation time is very short (in the order of 1 ms and below). This enables the data acquisition of lipid without any major preparation, since it is the predominating signal source in the plant object. With this method, the highest in-plane resolution in lipid-imaging in plants (6 μm) was achieved when analysing the lipid distribution in the xylem tissue of the resurrection plant (*Myrothamnus flabellifolia*) [Sch03].
The examination of assays of several seed lots of the western red cedar (*Thuja plicata*) indicated that non-viability is associated with a markedly reduced "liquid" lipid content, a conclusion which could not be drawn from X-ray images [Ter08].The germination capacity seems to be dependent of the "liquid" lipid content, since when the

seed is damaged, the oxidation of the "liquid" fraction tends to promote lipid polymerization.
The influence of ageing on the lipid distribution in the barley and wheat grain showed no perceptible effect on either the spatial distribution or the quantity of lipid present. For the standard spin echo sequence, no suppression of water or chemical shift selection was needed because the moisture content of the grain was low [Bor11].
Virtual models of the tobacco seed (*Nicotiana spp.*) could be derived based on measurements made from more than 200 seeds from both a wild type cultivar and a transgenic line [Fuc13]. The seeds were measured in bulk using a standard spin echo sequence. This was possible as no water signal was detectable in the dry seeds. Clear differences in the pattern of lipid accumulation in the seeds, both the endosperm and the embryo, were revealed by the comparison of the lipid models of the wild type and transgenic seed. Furthermore, a correlation between seed size and lipid content was detected in the transgenic, but not in the wild type line.

4.5.2 Selection via solvent suppression

The utilization of an adjusted solvent suppression scheme is necessary when more than one compound is NMR active (Fig. 4.3, centre). Especially the detection of sugars or the measurement of protons attached to lipid molecules within fruits requires a reliable suppression of the water signal. Signal from the other compound(s) is suppressed by saturating the particular protons prior to excitation of the desired magnetization, e.g. with a CHESS suppression module [Haa85]. This facilitates the acquisition of a CSSI dataset more rapidly than is possible by using CSI, but only one component can be detected during the experiment. A scheme of this imaging sequence is shown in Fig. 4.4. In an exploration of soybean and groundnut seeds, without an adjusted solvent suppression scheme, the image quality was severely deteriorated due to phase cancellation created by the sum of the two complex signals (in the overlapping regions of water and lipid signal) and "shadow" artifacts. These artifacts could be reduced by the inclusion of the suppression scheme [Hon09].
The NMR imaging of a tobacco capsule [Fuc13] could produce both an improved level of resolution over light microscopy-derived ones, while also providing a semi-quantitative measure of the capsule's and seeds lipid content. Datasets were acquired by applying a solvent suppression scheme able to produce both water- and lipid-selective images

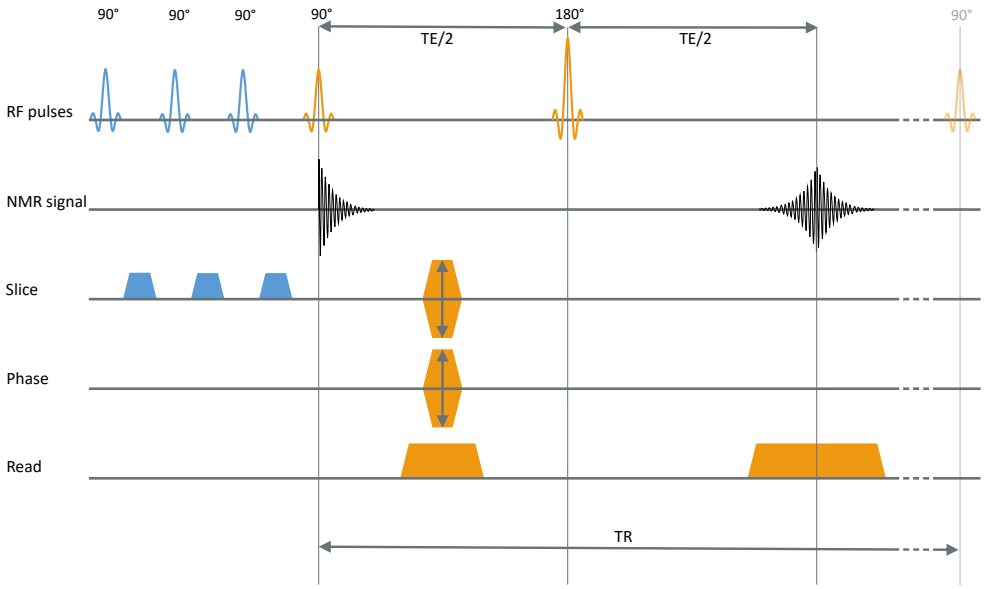

Figure 4.4: Scheme of a CSSI sequence combined with a CHESS module. The solvent suppression module (blue) is applied with selective RF pulses prior to (global) excitation of the desired compound (orange)

4.5.3 Improved CSS-imaging techniques

The ultra-high magnetic fields used in some NMR imaging experiments allow the user to include frequency-selective excitation and refocusing pulses. A requirement for this method is an accurate shim of the magnetic field, thus an optimization of its homogeneity.

Depending on the sample's composition, each compound's spectral peak bandwidth typically is in the range of 100 Hz (wet sample) to 1.000 Hz (dry sample). For the successful selective excitation of one single component, the centre frequency and the bandwidth of the RF pulse have to be adjusted to match the component's resonance frequency and bandwidth.

The pulse's duration depends on the bandwidths of the pulse. For this reason, narrow and thus chemical shift-selective pulses increase the minimal echo-time. In most imaging experiments, this restriction has no major effect on image quality.

Simultaneous CSSI measurement of multiple components

When applying the CSSI technique with component-selective pulses, only the magnetization of one chemical component is affected. Thus, during the setup of the MRI experiment, additional imaging volumes with identical sequence parameters (spatial and temporal) can be included in the measurement protocol, but each with an individ-

ually selected offset frequency (O_1) for the RF pulses, as is shown in Fig. 4.3 (right). Typically, in plant imaging this technique is used for the simultaneous measurement of two different chemical compounds for monitoring dynamic processes in plants. A scheme of an interleaved CSSI spin echo sequence is shown in Fig. 4.5.

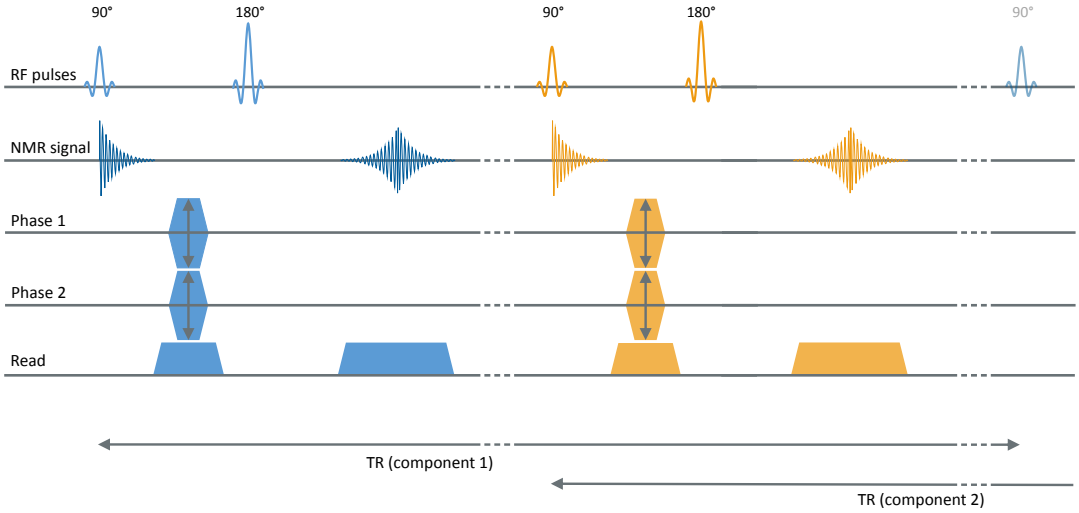

Figure 4.5: Interleaved CSSI spin echo sequence. The utilization of the interleaved option in the measurement protocol enables the simultaneous acquisition of two chemical compounds. Here, two spin echo sequences for two different compounds (blue and orange) are applied in succession. The chemical selective RF pulses are applied without slice selection gradients.

The use of (interleaved) CSSI measurements in seeds enables the assay of the lipid content and at the same time, it provides information about the overall seed topology. Furthermore, this imaging technique has a number of potential applications: among other things providing a means to test and optimize transgenic strategies aimed at the manipulation of seed size, seed number, and lipid content in fruits of various species. Two chemical-shift selective images of a maize seed are shown in Fig. 4.6
By imaging the distribution of water and lipids using frequency-selective pulses, the ripening process of olive fruits has been studied. While the lipids accumulated in the pulp, water movement from the inner to the outer mesocarp was detected [Bre07]. Using CSSI, the development of the barley grain has been characterized through independently acquired water and lipid datasets [Neu08]. The internal anatomy and the mechanics of lipid storage of the grain could be clarified based on the resulting high resolution images. For selected dissected areas of a target seed a calibration procedure involving the gas chromatography could be achieved. The complete 3D dataset then could be used for quantification regarding the absolute lipid content of the whole sample, assessing lipid concentrations in the micromolar range within the grain. Transfer-

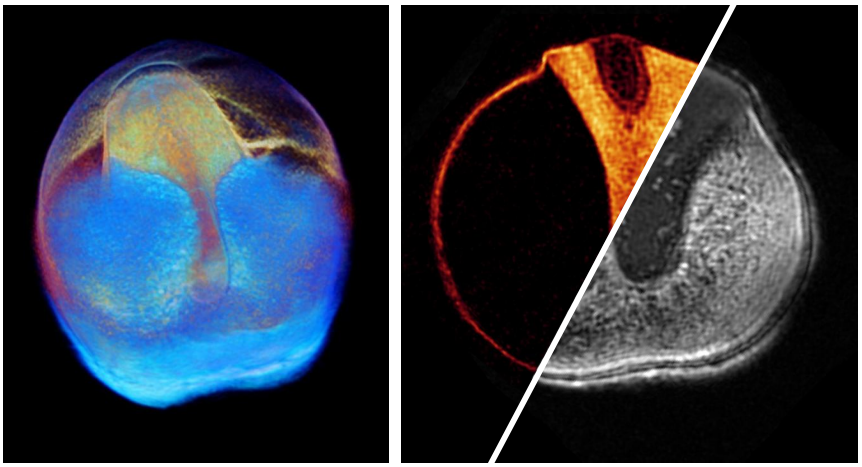

Figure 4.6: Chemical shift selective imaging of a maize seed. Left: 3D-visualization of water (blue) and lipid (orange) distribution in a maize seed during maturation. Right: Selected 2D-slices of the 3D dataset, showing the lipid (orange) and water (gray) in the maturing seed (previously published in [Mun16]).

ring this approach to a soybean resulted in a high level of agreement with the outcome of destructive gas chromatography.
The identification of the endosperm of the oat grain as being the predominant site for lipid accumulation was performed using a frequency-selective CSSI sequence [Hay11]. The spatially resolved MRI could distinguish between two closely related oat cultivars which differed in their grain lipid content.
Results previously acquired with mass spectrometric imaging (MSI) were compared with three dimensional MR imaging of lipids in cotton seeds. Against expectations, the obtained distribution of the lipids was found to be non-uniform [Hor12]. A comparison with the output of matrix-assisted laser desorption/ionization (MALDI)-MSI analysis showed that ion suppression may occur in mass spectrometry, thereby weakening the reliability of any quantitative conclusions.
When aiming to visualize lipid distribution in *C. sativa* seeds at a high level of resolution in 3D, some putative differences between genotypes with respect to metabolic processes underlying lipid production within the embryo were identified [Hor13].
The application of a water-suppression scheme prior to the high resolution lipid imaging of oilseed rape (*Brassica napus*) enabled the visualization of steep gradients in oil deposition within the tiny embryo under in vivo and in vitro growth conditions [Bor13b]. The spatial and temporal relations of lipid topology were defined to those established for the accumulation of starch and storage proteins, cellular growth, photosynthetic

activity, and metabolite pattern. By this study it was shown how the embryo is able to make local metabolic adjustments to its environmental and growing conditions, and a mechanistic view on the role of seed architecture for embryo metabolism in living seed was provided.
The three dimensional distribution of lipids in the oat grain was determined by using a frequency-selective spin echo sequence [Rol15]. Volume and lipid content of the various seed organs could be estimated on basis of the data.A further comparison between the lipid fraction in both the embryo and endosperm of a single bread wheat grain (*Triticum aestivum*) showed that the embryo and aleurone layer together represent the major storage site for grain lipids.
Differences in the distribution of lipids as well as in grain organ size between a wild type and a transgenic barley could be detected; these alterations were associated with metabolic perturbation induced by the presence of the transgene [Kov16].
The interleaved measurement of two or more components is an elegant use of the CSSI method. By applying component-selective pulses in a distinct time sequence, which is designed so that one component is excited during the interval reserved for the relaxation of other component, measurement time can be saved. With this method, high resolution MR imaging provided interleaved selective measurements of water and lipid. Analyzing the imbibition and germination of seeds (see also chapter 5) represents a major application of frequency-selective pulses in combination with interleaved volume acquisition.
In hourly intervals, imbibed seeds of *Pinus monticola* were imaged. The water uptake and changes in the lipid content both inside and at the surface of the megagametophyte could be studied [Ter05b].
The interleaved CSS imaging of a tobacco capsule delivered information regarding the hydration of the capsule and identified the vascular bundles, along with the placental stalk and bundles, as being the most strongly hydrated portions of the capsule in the water dataset. The high resolution lipid dataset in addition, containing hundreds of simultaneously imaged seeds, provided the means to non-destructively estimate the number of seeds harbored by the capsule, and to assess lipid gradients inside of individual submillimetre seeds [Fuc13].

Advanced Imaging Techniques

The requirement for short measurement times of high-resolution datasets can only be fulfilled when the signal to noise ratio (SNR) is sufficient. An improvement of signal can be reached with different approaches, e.g. by shortening the echo time, TE, or

elongating the repetition time, TR. Typically, these parameters are already optimized as a compromise between measurement time, chemical selectivity and matrix size.
Thus, the noise acquired in an MRI dataset has to be reduced, which can be achieved by the application of a cryo probehead: An NMR coil combined with a closed cycle helium cryocooler. Here, the NMR coil(s) as well as the electronic circuits are cooled down to a very low temperature for reduction of noise contributions resulting from the random thermal motion of electrons in the conductors. Also, the resistivity of the metal components is reduced at lower temperatures, which additionally leads to a decrease of noise. Further components, such as the preamplifier, the filters, and the transmit-receive-switch are also cooled for reduction of noise.
Subsequently, the sample inside the NMR coil hast to be tempered to an ambient temperature; this is achieved by an additional air conditioning of the sample during the experiments.
The NMR scanner recently installed at the IPK Gatersleben (see Data 10.4) is equipped with a double resonant ^{1}H-^{13}C-CryoProbehead (see Data 10.12) which is cooled down to a temperature of approximately 18 K. Compared to non-cryogen cooled NMR coils, an improvement of SNR by a factor of 7 to 8 can be reached with this experimental setup (data based on the manufacturer's specifications).

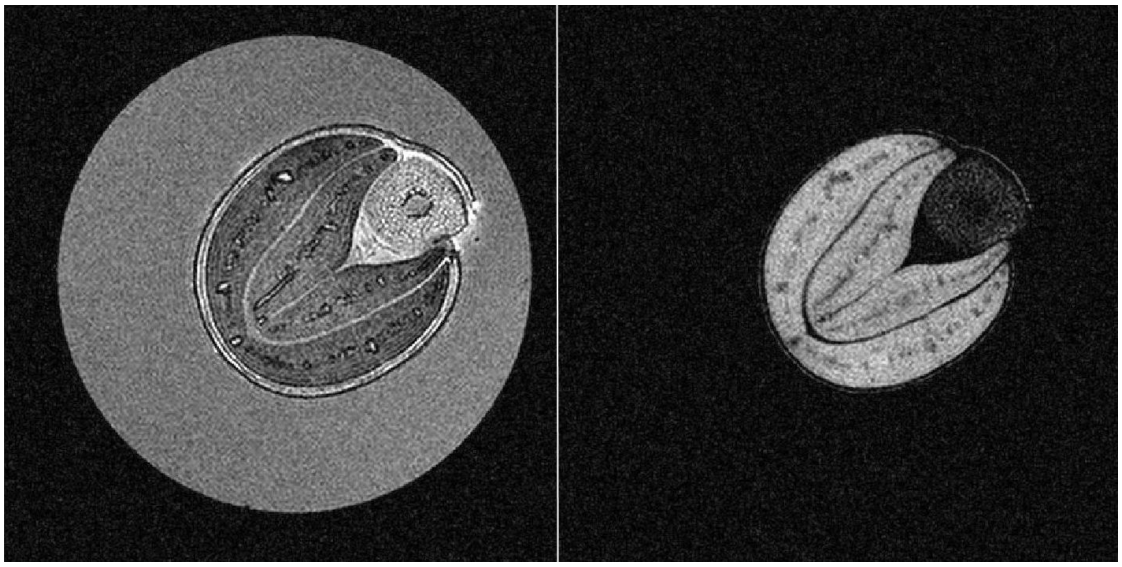

Figure 4.7: Chemical shift selective dataset (left: water, right: lipid) of a germinated rapeseed, acquired with a cryogen cooled probehead. The isotropic resolution of 20 μm was only reachable due to reduction of the noise created by the hardware.

This coil was used for high-resolution chemical shift-selective datasets of a germinated rapeseed (see Fig. 4.7). An isotropic resolution of 20 μm could be achieved with the

measurement parameters shown in Tab. 4.1.

TR	750 ms	FoV	4.5 x 4.5 x 4.5 mm^3
TE	10.1 ms	Matrix	225 x 225 x 225
NA	2		
NE	1	T_{Acq}	21 h 5 min

Table 4.1: Measurement parameters for the cryoprobe experiment of a germinated rapeseed. Abbreviations: **TR**: Repetition Time, **TE**: Echo Time, **NA**: Number of Averages, **NE**: number of Echoes, **FoV**: Field of View, $\mathbf{T}_{Acq}$: Total duration of the experiment.

The experimental setup is more complicated when a cryogen cooled probehead is utilized for signal acquisition, yet the advantages gained in signal and/or image resolution are obvious: With the cryoprobe, the image resolution could be doubled in all three dimensions, compared to typical image resolution of germinated rapeseeds acquired with standard room temperature coils. This NMR coil will also be used for the detection and localisation of ^{13}C-labelled molecules in plant samples, as was performed by Melkus et al. [Mel11].

4.6 Outlook

In the following part, the four major projects of this PhD-thesis are presented:

In chapter 5, a chemical shift selective imaging technique was developed for the monitoring of a germinating rapeseed and the visualization and localization of the water entry point in the seed coat. Both temporal and spatial resolution, as well as the chemical selectivity of the RF pulses had to be adjusted to acquire high resolution MRI datasets, which could be further analyzed with 3D rendering software tools. Based on the MRI experiments, further experiments were performed to underline the obtained results.

Chapter 6 focuses on the spatial distribution of saturated and unsaturated fatty acid components, visualized in seeds and fruits with an adjusted CSS-Imaging technique. Developmental and species-typical differences were found in the investigated plant samples. The method can be used for the monitoring of the seed status under different storage conditions and may be used as a characterization for seed phenotyping.

With the development of a plant imaging method based on a sequence typically used in clinical imaging, the fast-relaxing compounds in plants and seeds (starch, bound water) were visualized for the first time. In chapter 7 the advantages of this non-invasive method are presented, it provides new insights into plant objects at the microscopic level.

The transport characteristics of a contrast agent in living plant samples was investigated in chapter 8: A method was developed to acquire information non-invasively about dynamic features of the contrast agent. Its concentration in the living plant tissue and translocation velocity could be determined with this approach.

Chapter 5
Fat- & water-selective dynamic microscopic imaging of germination

Since one of the first studies of MRI on plants, the germination of seeds was of interest to both, the physicist designing MRI methods, and the biologist, now getting new insights into the beginning of a new life [Con87]. Here, a novel approach was developed to investigate the restart of life in a germinating rapeseed. By combining a non-invasive, compound-selective imaging technology and the invasive, but high-resolution analytical tools microscopy, mass spectrometry, and respiration mapping, the pathway of water in the germinating seed could be tracked and the restart of a new life in each of the seed's organs could be correlated to the presence of water. Simultaneously, the restart of the embryo's metabolism could be tracked in the residual endosperm, being located underneath the seed coat and between the cotyledons - opposed to previous assumptions of a metabolism in the seed's organs. A predetermined gap in the aleurone layer, being permeable for the water and thus working as an entry-point of the water into the seed, was identified.[1]

Preface and Motivation

The germination, the process of a dormant seed springing to life, has been a focus of plant biologists for many years. Yet still, the early events of the water uptake (imbibition), during which's the embryo's metabolism restarts, remain unknown. By adopting a comprehensive in vivo approach designed for characterization of both the structural changes occurring during germination and entry and redistribution of water, and the the catabolism of the lipids, the source for the rebooting in oilseed rape/canola (*Brassica napus*) seed has been investigated. The capacity of dynamic MRI to show non-invasively provided insight into the imbibition process, showing that the seed's architecture and especially the embryo's vasculature directly determine the temporal

[1]This chapter refers to the article "A functional imaging study of germinating oilseed rape seed" previously published in New Phytologist 216 (2017): 1181-1190 by Munz et al. [Mun17]

pattern. In the endosperm, the respiratory oxygen consumption is initiated first and only later spreading in the embryo. by capturing the metabolic signatures and imaging of lipids together is was possible to to resolve where and when specific metabolic pathways are re-activated. The whole germination process is guided by the spatiotemporal sequence of tissue hydration.

5.1 Introduction and Overview

Crop establishment strongly depends on seed germination [God10; FS15]. The imbibition (the uptake of water) marks the beginning of the process, it ends with the protrusion of the seedlings radicle (root) [Bew97; FS06]. The physiological, molecular, and biochemical basis of the process has been elucidated by the long-standing interest of the plant biologists in germination [Wei11; Née17; Raj12]. The rate and timing of germination are influenced by endogeneous (hormone status, dormancy, genotype) and exogeneous (availability of oxygen, moisture, and ambient temperature) factors. During the process, storage proteins and other nutrients are catabolized.The more complete the picture of the germination is becoming, the more attention is turned to the processes and events occurring in vivo in the seed.
Many attempts to trace the water into and within the germinating seed have been made, mainly because the the rebooting of the seed's metabolism requires water. in conventional experiments, this is achieved by imbibing the seeds in the presence of tracers, which can be dyes or compounds small and inactive enough to eliminate a disruption of the imbibition process [Sal11; Mus05]. Non-invasive imaging of the germination process was promoted at a high level of spatial resolution by radiation platforms which either rely on neutron beams [MAT97] or X-rays [Nie17]. However, such platforms are rendered unusable for long-term observations by the excessive energy intruduced into the sample. The nuclear magnetic resonance technology does not rely on high energy radiation, it was designed to capture many of the physical, dynamic, and biochemical properties of living tissue. The potential of NMR to monitor living objects such as plants over long periods of time has been shown [Bor12; VA13]. A number of novel insights have been produces by it's application to the non-invasive study of germination, as can be seen in in Tab. 5.1.
The conclusion was that the permeability of the seed's coat (testa) plays a central role to the control of water uptake. Furthermore, the process of imbibition differs significantly between different seed tissues and between species [Ste16]. The dynamic visualization of the germination process in any of the leading crop species is a challenge due to the relatively small size of most seeds and due to the heterogeneity of the tissue

Object	FoV	time [min]	dyn. model	Components	Voxel [nl^3]	B_0 [T]	Author (Year)
Barley(*hordeum vulgare*)	2D	n.p.	no	water	2.5	6.3	Ishida (1996) [Ish96]
Soy bean(*glycine max*)	2D	n.p.	no	water	0.44	8.4	Pietrzak (2002) [Pie02]
Pea (*Pisum sativum*)	2D	n.p.	no	water	1.74	9.4	Wojtila (2006) [Woj06]
Lupin (*Lupinus luteus*)	2D	n.p.	no	water	1.8	9.4	Garnczarska (2007) [Gar07]
Walnut (*Juglans nigra*)	2D	17	no	not selective	n.p.	4.7	Vozzo (1996) [Voz96]
barley (*hordeum vulgare*)	2D	17	no	water	0.91	8.4	Gruwel (2002) [Gru02]
Wheat(*Triticum aestivum*)	2D	20	no	water	2.9	7.0	Rathjen (2009) [Rat09]
Pepper(*Capsicum annuum*)	2D	132	no	water & lipid (consecutively)	0.54	9.4	Foucat (1993) [Fou93]
Tobacco(*Nicotiana tabacum*)	3D	110	no	not selective	0.03	9.4	Manz (2005) [Man05]
Castor Bean(*Ricinus communis*)	3D	34	no	water	n.p.	9.4	Morris (1990) [Mor90]
Pine (*Pinus monticola*)	2D	17	no	water	3.04	8.4	Terskikh (2005, 2011) [Ter05b; Ter11]
Mung bean (*Vigna radiata*)	2D	52	no	water	2.89	4.7	Connelly (1987) [Con87]
Bean (*Phaseolus vulgaris*)	3D	5	no	water	1.6	7.0	Kikuchi (2006) [Kik06]
Soy Bean(*Glycine max*)	3D	5	no	water	3.8	11.7	Koizumi (2008) [Koi08]
Bean (*Vicia faba*)	3D	5	no	water	102.5	7.0	Koizumi (2014) [Koi14]
Rapeseed(*Brassica napus*)	3D	27	yes	water & lipid (simultaneously)	0.10	11.7	Munz (2017) [Mun17]

Table 5.1: Overview of germination experiments conducted via MRI. Abbreviations & Explanations: **time:**: temporal resolution, thus time per dataset; **Voxel**: Voxel volume **n.p.**: not provided.

within them.

5.2 Material and Methods

5.2.1 Experimental setup and preparation of seeds

In all experiments seeds of oilseed rape (*Brassica napus L. var. Reston*) grown in greenhouse were used. By placing seeds inside of 5 mm NMR-tubes containing either agar or water, or on wet filter paper in Petri dishes germination was tested. For destructive assays, the seeds were taken at regular intervals for each particular experiment.

5.2.2 Long time MRI experiment

For the MR-imaging experiments of the germination, 2 % agar (Agar-Agar, danish, Carl Roth GmbH, Germany) with a firm, fine texture was used. It provided good seed-to-exterior contact, minimization of seed displacement during the experiment and it allowed for oxygen/water-supply during the long time monitoring of the germination process.
Materials like teflon as a holding device could not be used, since the transition water-teflon could cause artifacts in the resulting images. Tissues like cotton wool or sponges tend to include small air bubbles or can cause their formation. The Bruker AMX NMR scanner[2] and a custom made Helmholtz-type resonator[3] were used for the long time monitoring of the germination. For the simultaneous measurement of the alteration of water and lipid a Multi-spin echo sequence was adjusted (see Fig. 4.5) with frequency selective hermite pulses (2,000 Hz bandwidth). The detailed measurement parameters for achieving a temporal resolution of 27 min and an isotropic spatial resolution of 94 μm are presented in Tab. 5.2.

TR	400 ms	FoV	12.0 x 6.0 x 6.0 mm^3
TE	7.2 ms	Matrix	128 x 64 x 64
NA	1	N_{Exp}	110
NE	8	T_{Acq}	50 h 03 min

Table 5.2: Measurement parameters for the long time monitoring experiment. Abbreviations: **TR**: Repetition Time, **TE**: Echo Time, **NA**: Number of Averages, **NE**: number of Echoes, **FoV**: Field of View, $\mathbf{N}_{Exp}$: Number of individual experiments, $\mathbf{T}_{Acq}$: Total duration of the experiment.

[2]For details see Data 10.1 in the appendix
[3]For details see Data 10.5 in the appendix

5.2.3 Localization of water gap

The microscopy measurements for analysis of the water gap in the aleurone layer were performed with the hardware as described above and with the measurement parameters as in Tab. 5.3.

TR	1,000 ms	FoV	10.0 x 5.0 x 5.0 mm^3
TE	8.2 ms	Matrix	200 x 100 x 100
NA	4	N_{Exp}	1
NE	1	T_{Acq}	11 h 06 min

Table 5.3: Measurement parameters for analysis of the water gap in the aleurone layer.

5.2.4 Imaging of non-germinating seeds

The measurement of the non-germinating seeds was performed with the measurement parameters shown in Tab. 5.4. The experiment was performed on the Bruker 750er[4] and with an in-house built saddle coil (i.d. 5mm).

TR	250 ms	FoV	12.0 x 6.0 x 6.0 mm^3
TE	5.2 ms	Matrix	128 x 64 x 64
NA	1	N_{Exp}	70
NE	1	T_{Acq}	19 h 54 min

Table 5.4: Measurement parameters for measurement of the non-germinating seeds.

5.2.5 Microscopy of the vascular tissue

In order to validate the in vivo-imaging, high resolution microscopy experiments were performed on an Agilent 400 MHz NMR scanner[5] and the custom-built ceramic resonator with an inner diameter of 5 mm[6]. At different stages of imbibition/germination, seeds were fixed and immersed in fully-fluorinated liquid (FC-43, 3M, St. Paul, MN, USA) for susceptibility-matching. For imaging, a standard spin echo sequence with an adjusted solvent CHESS [Haa85] suppression scheme was used, the sequence was set up to acquire signal from the protons attached to the $(CH_2)_n$ molecules only. The global T_1 value of the sample was measured for adjustment of the repetition time TR. Minimization of the echo-time TE was performed for suppression of influence of

[4]For details see Data 10.2 in the appendix
[5]For details see Data 10.3 in the appendix
[6]For details see Data 10.9 in the appendix

the transverse relaxation. The use of a partial-Fourier-acquisition scheme, the measurement time could be reduced by 25% to approx. 21 h. The detailed measurement parameters are shown in table 5.5.

TR	683 ms	FoV	21.0 x 4.5 x 4.5 mm^3
TE	7.6 ms	Matrix	526 x 84 x 112
NA	12	N_{Exp}	1
NE	1	T_{Acq}	21 h

Table 5.5: Measurement parameters for the long time monitoring experiment. Abbreviations: see table 5.2

5.2.6 Data processing

The processing of all raw NMR data was performed using in-house written Matlab scripts (MathWorks, Natick, MA, USA). A zero-filling by a factor of 2 was performed, after Fourier-transformation to image-space, the multiple echoes (if acquired) were used for T_2-correction of the measured datasets. The relative proton density was calculated, based on a Least-Squares-Algorithm, for each voxel individually thus minimizing the transverse relaxations influence.
The 3D-visualization and segmentation of the resulting image data was performed using AMIRA software (FEI Visualization Sciences Group, Mérignac, France).
Furthermore, the 4D monitoring data was used for dynamic modelling.

5.2.7 Non-MRI Methods

The descriptions of non-MRI methods supporting the work in this chapter can be found in the Appendix, Chap. 10.3.

5.3 Results

5.3.1 Location of water entry and hydration pattern

The embryo, consisting of the radicle and the two cotyledons, is encased by the testa (Fig. 5.1), between its outer surface and the testa a few air-filled spaces can be found. As a result of tissue shrinkage occurring during tissue dehydration, additional spaces can sometimes form in the centre of the seed. After maturation, only the lipid-rich aleurone layer remains from the endosperm, it is located between the testa and the embryo and in contact with the radicle and the inner cotyledon. like a “second skin”,

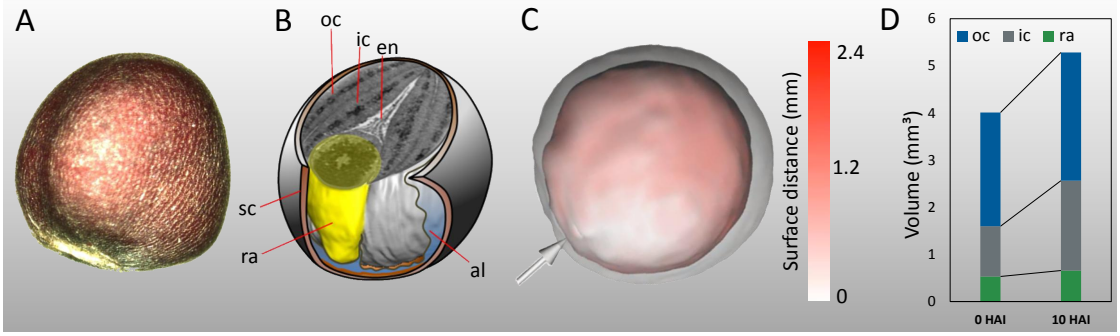

Figure 5.1: Seed expansion during imbibition. (A) Mature rapeseed. (B) Schematic view of a mature and dry seed, showing the individual organs: **en** endosperm, **ic** inner cotyledon, **oc** outer cotyledon, **sc** seed coat, **al** aleurone, **ra** radicle. (C) Volume of embryo at the start (red) and end (gray) of the germination process. (D) Volume of selected organs at time of imbibition and 20 h after imbibition.

the embryo is enveloped by the oil-containing endosperm. During the imbibition, the volume of the seed increases rapidly due to the rise of the seed's water content from ∼5% to ∼30%. This swelling leads to the rupture of the testa by the expansion of the radicle.

An explanation of the oberserved pattern of swelling can be given due to the time-lapsed images Fig. 5.2. Water enters the seed at a very small region of the testa (0.07 mm^2, representing less than 1% of the overall seed surface) in close proximity to the hilum, indicated by the arrow. During the process, water entered neighbouring regions of the testa and hydrated them from the inside. Meanwhile, the embryo remained dry, since it was protected by the lipid-rich aleurone layer.

Only in the region around the micropyle, a hydration front moving in the centripetal direction was formed. The first water signal could be detected at the radicle apex, most of its flow was present in the central stele (asterisk in Fig. 5.2) and can be assigned to xylem vessels. Meanwhile, water was moving into the space formed between the axis and the inner cotyledon thereby filling the centre hole in the embryo. Until both the endosperm (micropylar and central portion) and the radicle had become fully hydrated (Fig. 2G and H), the water content of the parenchyma tissue in both cotyledons did not increase. After that the flow of water through the central stele of both the radicle and the hypocotyl increased further reaching first the inner and eventually the outer cotyledon. This pattern was observed in other measurements and it occurs in an almost fully synchronized fashion within seedlots in the same experiment (see supplemental movies in [Mun17]).

The micropylar region was found in seeds of other species as the location of the water

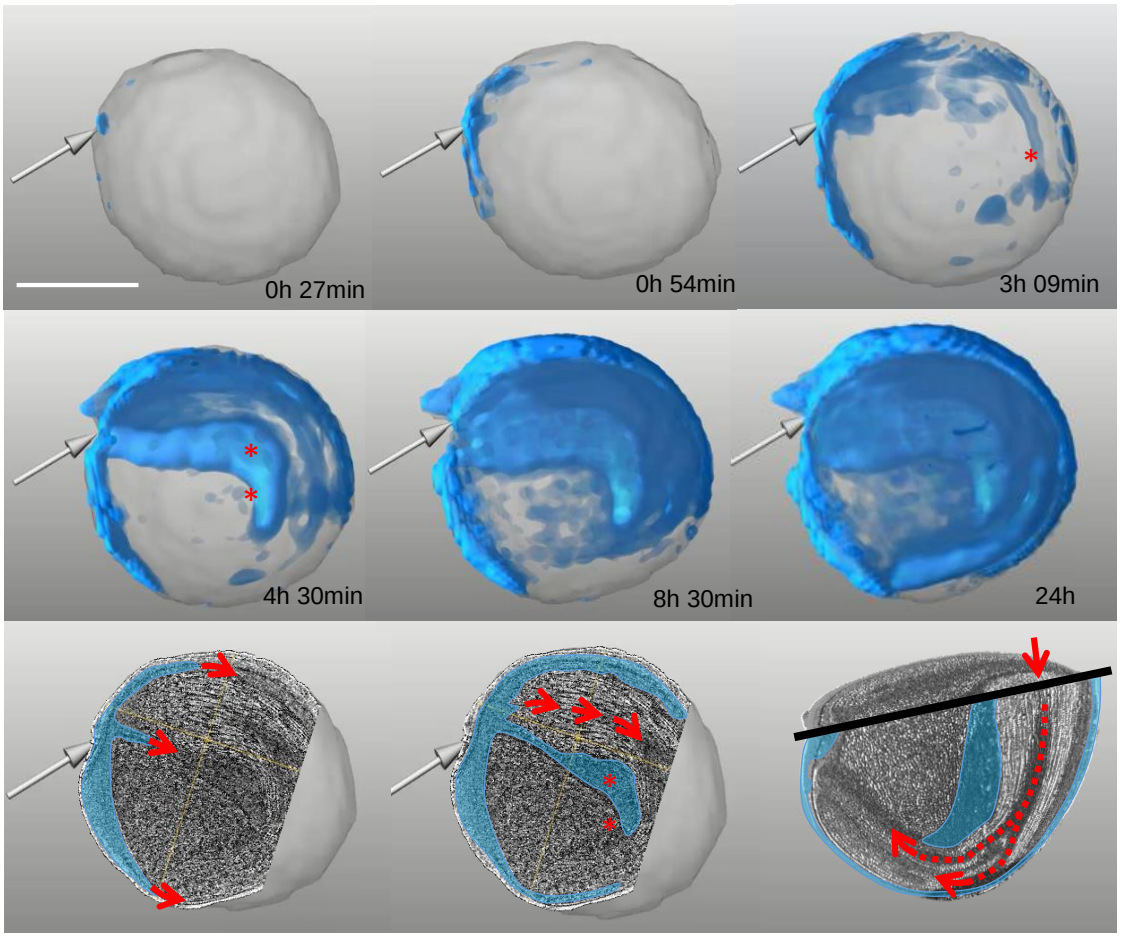

Figure 5.2: 3D Visualization of the water uptake in germinating *B. napus* seed based on continuous MRI-monitoring. The top and centre line show 3D-models of water uptake taken at distinct time intervals during imbibition; The bottom line shows the scheme of water allocation for subsequent stages of imbibition with blue colour indicating local high water level and red arrows indicating direction of water movement; gray arrow indicates the place of radicle protrusion

entry, which was attributed to an apparent water gap in the seed coat [Ste16]. By investigating the lipid-selective 3D datasets an additional control point could be found: generally, the lipid-rich aleurone layer serves as a hydrophobic barrier between the embryo and the seed coat. In the region of the radicle apex, the lipid deposits are partially reduced (Fig. 5.3), thereby forming a water gap which channels the water directly towards the radicle apex. This leads to the conclusion that the pattern of water uptake during imbibition cannot be described as a continuous process of diffusion through the testa from the outside to the inside. Apparently, it is controlled by features of the seed's architecture. The permeability of the testa is not uniform, the water

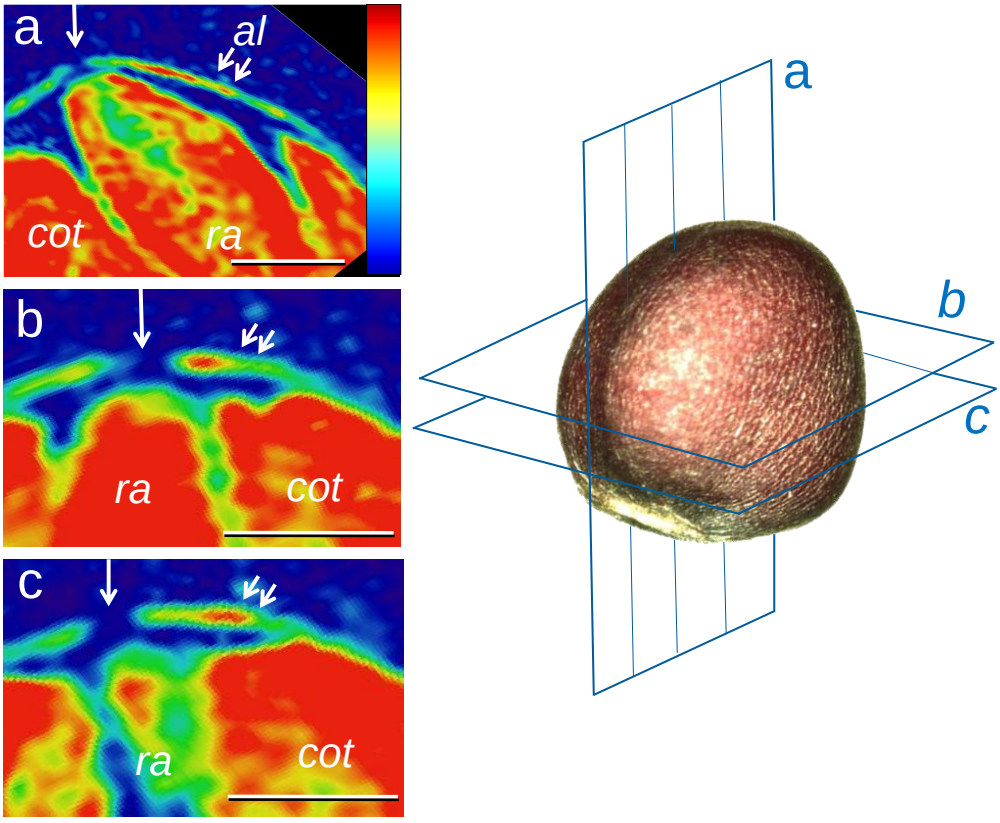

Figure 5.3: Localization of lipid-gap in the endosperm of mature, dry seed. Left panels show lipid distribution within the micropylar region of seeds measured using non-invasive MRI. Scheme on the right shows visualization plane (a, b, c) used for lipid imaging across the seed. The lipid-rich aleurone layer (double arrowed) covers the cotyledons. The white bold arrow indicates aleurone where lipid deposits are omitted, leaving a water gap in close proximity to the radicle's tip. Abbreviations: al – aleurone; cot – cotyledon; ra – radicle. Bars: 500 μm

can only enter the seed through a narrow gate which is located at a region in direct proximity to the radicle's tip. The hydration of the seed is triggered by the radicle's hydration.

5.3.2 Vascular arrangement in embryo

The water-conducting tissues inside the could be reconstructed based on the high-resolution MRI datasets. As described above, the water entered the seed through a predetermined passageway in the seed coat and was guided through the radicle via separate vessels towards the inner and outer cotyledons, see Fig. 5.4. The observed properties of the vascular tissue correspond well with the reconstructed vascular ar-

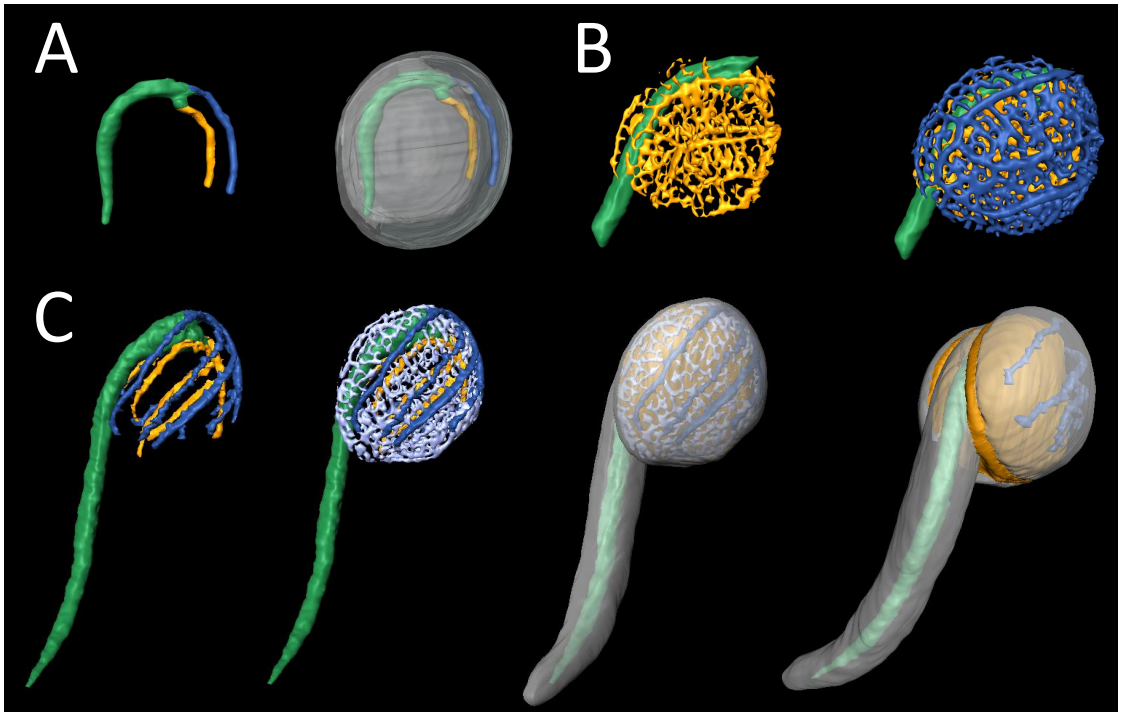

Figure 5.4: 3D reconstruction of vascular tissue inside rapeseed embryo, as revealed by MRI. (A) Location of vascular system inside of imbibed seed (left), and its three main strains (right): the central vein within radicle branches in two supplying the two cotyledons; (B) Vascular arrangement just after radicle emergence; vasculature of both inner (left) and outer (right) cotyledon has evolved into network structures; (C) Vascular arrangement approximately two days after germination: location inside of seed and branching.

rangement. The analysis of the model revealed a doubling in volume of the vascular system between the initiation of imbibition and the protrusion of the radicle. A highly anastomosed structure had formed within both cotyledons at the end of the germination, which later developed into the familiar vascular system in the expanded cotyledon with its central and secondary veins (Fig. 5.4). In the mature embryo of seeds of many plant species, the predetermined vascular architecture is already in place [DR16]. Thus, any subsequent expansion of the vascular system requires only the extension and maintenance of an existing vascular network. During imbibition, the preformed vascular system was activated, allowing the embryo to perform the same mode of water and assimilate transport which can be observed in the adult plant: water is directed “upwards” (towards the cotyledons), metabolites are simultaneously transported “downwards” (towards the hypocotyl and the radicle).

5.3.3 Lipid dynamic during germination

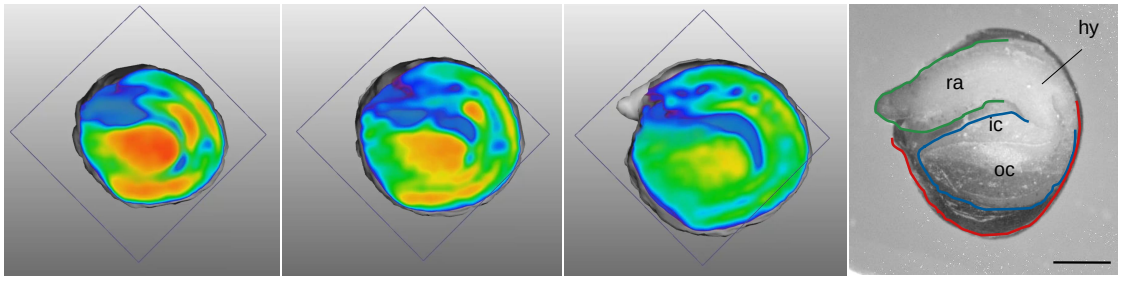

Figure 5.5: Changes in the lipid content of the oilseed rape seed during germination, for full sequence see Supporting Movie in [Mun17]. MRI-based visualization of the distribution of lipids before, during and 23 h after imbibition. The lipid level is colour-coded. The gray arrow indicates site of the radicle's protrusion. The gray shaded region indicates the outer seed structure. **Right**: The various components of the seed. Abbreviations: ra-radicle; hy-hypocotyl; ic-inner cotyledon; oc-outer cotyledon. Bar: 1 mm.

In the *B. napus* seed, lipids (triacylglycerols) are an even bigger carbon source than sugars [Bor13b]. The localization of the lipid degradation within the germinating seed was the focus of this experiment. The high-resolution 3D datasets were acquired to display the 3D dynamic of lipid distribution during germination. The mature and dry seeds have their lipid deposits in cotyledons and less in radicle/hypocotyl [Bor13b]. A fast, local decrease in lipid levels within all embryo tissues could be observed during the first hours of imbibition (lipid maps in Fig. 5.5). The watering of the tissues lead to a drop in lipid signal intensity, which was not caused by by lipid degradation but due to swelling (volume increase of tissue).
Measuring the total lipid levels in dissected embryo organs confirmed that lipid content per organ was not changed (Fig. 5.6). A statistically significant reduction in lipid content was first detectable after germination, starting in hypocotyl/radicle and followed later on by cotyledons. The lipid degradation in the lipid-rich endosperm-seed coat fraction of seed showed a continuous decrease of lipids, which started already during imbibition (Fig. 5.6). This suggests, that the mobilization of lipids starts here, as was evidenced by the lipid mapping, showing that lipid disappears from endosperm first (Fig. 5.6). The degradation of lipid has an organ-specific sequence starting at imbibition in endosperm, later on followed by hypocotyl/radicle and eventually cotyledons.

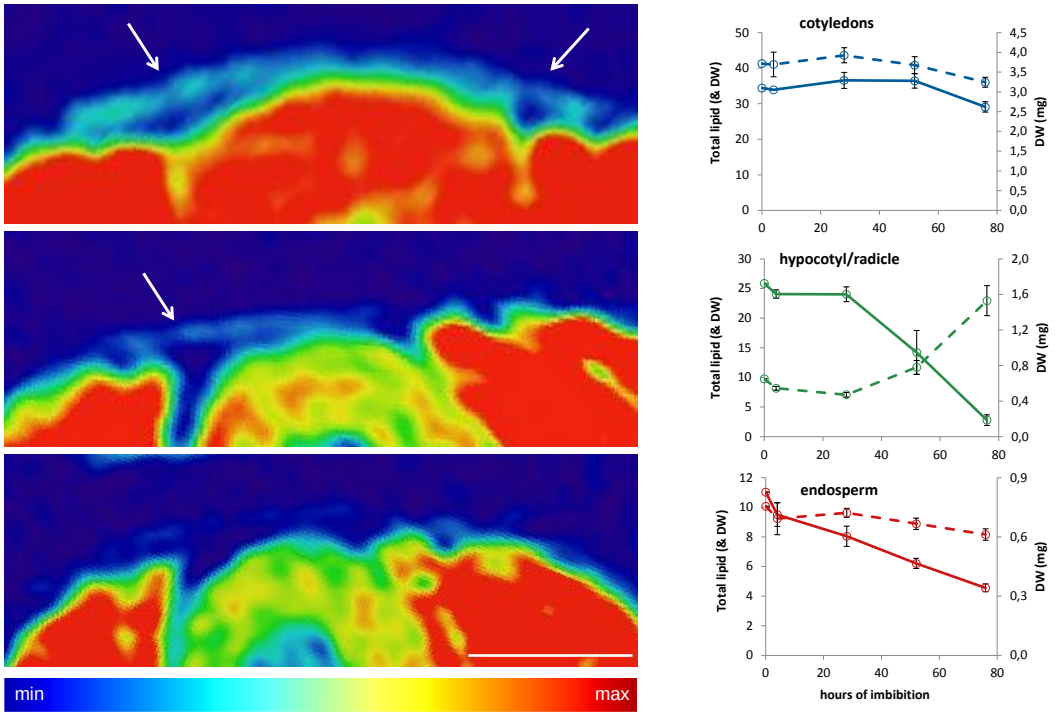

Figure 5.6: **Left**: MRI-based imaging of lipid distribution at (top) the early stages of imbibition, (middle) germination, (bottom) root elongation. Lipid levels are colour-coded and the arrows point to the lipid-containing endosperm. **Right**: Changes in lipid and biomass during imbibition and subsequent seedling growth phase. Component-specific changes in lipid content (solid line) and biomass dry weight (DW, dotted line). Values given as mean ± SD (n=5). Abbreviations: ra-radicle; c-cotyledon. Bars: 250 μm

5.4 Summary

In the years since domestication by intensive breeding, the seed quality of oilseed rape has been greatly improved, yet still yields are compromised by uneven crop establishment and uneven seedling vigor. Improving the understanding of the events occurring during the germination process of this important oilseed crop could be a contribution to improve its productivity. The seeds, measuring only a few millimetres in diameter, take up the water unlike a sponge, its mode rather resembles that of a water clock. Via the premature vasculature bundle, a structure which goes on to develop into the seedling's vascular system, the water enters the embryo. The rehydration of the embryo is an organized procedure and largely predetermined by the seed's architecture. The spatiotemporal sequence of tissue rehydration is followed by metabolic re-activation, starting the full range of molecular and metabolic processes required for germination [Non10; Wei11]. The initial energy and intermediates required for respiration and

localized metabolic rebooting (e.g., 3-PGA around the vasculature) are provided by carbohydrate pools, until the mobilization of lipids is initialized. This leads to the question whether the lipids deposited in tissue are also involved in directing the flow of water. This behaviour is known from certain resurrection plants such as *Myrothamnus spp.* in which a rapid switch from a dehydrated and quiescent state to a fully hydrated one occurs [Can00]. It was proposed, that the lipid-rich key transport tissues in *M. flabellifolia* and their spatial arrangement influence water movement [Sch03]. It seems plausible, that seeds and resurrection plants have much more in common regarding their strategic orientation. Current genome studies on *Xerophyta viscose* strongly support the hypothesis that by redirection of genetic information from desiccation-tolerant seeds the vegetative desiccation tolerance arose [Cos17].

For many years, germination, the process whereby a dry, quiescent seed springs to life, has been a focus of plant biologist. Nevertheless, the early events following water uptake, during which metabolism of the embryo is restarted, remained enigmatic. In this chapter, the nature of the cues required for this re-awakening process in oilseed rape (*Brassica napus*) seed has been investigated.

A non-invasive in vivo approach was designed to visualize the link between the entry and allocation of water, metabolic events and structural changes occurring during germination. For this, functional magnetic resonance imaging was combined with Fourier transform infrared microscopy, fluorescence-based respiration mapping, computer-aided seed modelling and biochemical tools.

An endospermal lipid gap, which channels water to the radicle tip, from whence it is distributed via embryonic vasculature toward cotyledon tissues, was discovered. The resumption of respiration restarts first in the endosperm, only later spreading to the embryo. Sugar metabolism and lipid utilization are linked to the spatiotemporal sequence of tissue rehydration.

As a conclusion, this imaging study provides insights into the spatial aspects of key events in oilseed rape seeds leading to germination. It demonstrates how seed architecture predetermines the pattern of water intake, which sets the stage for the orchestrated restart of life.

Chapter 6
Localization of unsaturated fatty acids by chemical shift selective imaging

In this chapter, a method was developed for the non-invasive detection and visualization of the spatial distribution of saturated and unsaturated fatty acid components in plants via chemical shift selective MRI. The method can be used for the non-invasive evaluation of storage conditions of seeds, for seed profiling and phenotyping.

6.1 Unsaturated fatty acids in plants

Lipids generated in the plants mostly consist of triglycerides (or triacylglycerols, TAG), which are three fatty acids connected as an ester derived from glycerol (Fig. 3.4). Each of these individual fatty acids is a chain of carbon atoms with hydrogen atoms attached to it. The metabolic function of the plant influences the number of carbon atoms in a fatty acid. TAGs made of identical fatty acids are called 'simple' while TAGs which are a combination of different fatty acids are called 'mixed'. One further detail enabling a differentiation between the various fatty acids, besides their length, is the number and position of double bonds between the carbon atoms. Fatty acids that contain one or more double bonds between carbon atoms are referred to as unsaturated fatty acids, with the differentiation between mono- (one double bond) and poly- (more than one double bond) unsaturated.

Due to the incapability of the human body to produce a sufficient amount of unsaturated fatty acids, they represent an important component in the human diet. The determination of the content of unsaturated fatty acids, also referred to as ω-3, ω-6, and ω-9 fatty acids, in a lipid-containing seed or fruit provides the knowledge about its **dietary value**.

For many years, the influence of the composition of human diet on the fatty acid composition in adipose tissue has been a research topic [Gru70; Tho96; Hwa03]. New

insights for medical examinations are provided by the capability of MRS and MRI to acquire information about the amount and distribution of unsaturated FACs in human tissue. By using Chemical Shift Imaging (CSI), the visualization of unsaturated fatty acid components in vivo can be performed. Due to its non-invasiveness, the acquired data can be used for mapping of the FACs [Lun01] or as an indicator for oncolytic adenovirus treatment [Hem14]. By using two-dimensional MRS, the correlation of tumor grade and mitotic activities with the accumulation of unsaturated lipid in leiomyosarcoma has been shown [Sin96]. Localized magnetic resonance spectroscopy was applied to detect a lowered level of unsaturated fatty acids in human breast carcinoma, in coincidence with histology, ultrasound and mammography [He04; He07].
A variety of information can be provided by the localization and quantification of unsaturated fatty acids. Both ^{1}H and ^{13}C magnetic resonance spectroscopy (MRS) provide the means to determine the fatty acid composition of vegetable oils and thus to classify them [Shi89; Miy98; Vig03]. Furthermore, the fatty acid profile and the free fatty acid content of oils could be performed by using MRS [Kno04; Sat09].
When single-component acquisition is desired, the broadened resonances of the protons attached to the individual components in plant tissue such as seeds and fruits can lead to challenges [Gus93]. Through application of chemical shift selective pulses, the direct imaging of olefinic protons in an *Afzelia cuanzensis* seed could be performed [Gus94]. By using static and Magic Angle Spinning (MAS) ^{13}C spectroscopy on different seedlots of western redcedar (*Thuja plicata Donn ex D. Don*) seeds, a correlation between germination capacity and the amount of unsaturated FACs in the seeds was detected [Ter08]. The monitoring of the lipid profiles of *Jatropha curcas* seeds during their development revealed that the percentage of unsaturated FA increased during maturation. A more detailed distinction between mono- and polyunsaturated FAC showed an increase of the monounsaturated and a decrease of the polyunsaturated FACs [Ann08]. While growing a rapeseed embryo in planta but in darkness, the absence of light had an influence on the photosynthetic contribution of lipid accumulation: the contribution of the unsaturated fatty acids was lowered [Bor13b].
The **natural diversity** of seeds of one plant type is tremendous and breeding even further increases the variety of seeds. The ratio of unsaturated:saturated fatty acid components is a characteristic that can be used for seed phenotyping.
The investigation of the plant object should be performed within a short range of time or non-invasively, since oxidation of the lipid leads to a deterioration of the lipid quality and a destruction of the double bonds in the lipid chains.
Thereby, the degree of unsaturation in the TAG chains can help determine the **storage condition** of the seed, i.e. the **seed quality**, since the double bonds can be affected

by oxidation when the plant part is damaged and oxygen can enter through the seed coat. The genebank at the IPK Gatersleben requires non-invasive **monitoring** of the stored seeds; the determination of the oxidation status would be a meaningful method for evaluation of storage conditions and germination capability; about its age or the seed coat's integrity.
The noninvasive localization of the spatial distribution of unsaturated fatty acids in plant objects can support the screening procedure and **analysis** of transgenic seeds. Spatial variations in the lipid distribution, regarding both saturated and unsaturated fatty acid components between transgenic and wildtype seeds may occur and can be visualized non-invasively via CSS-MRI.

6.2 Material and methods

The NMR spectra containing the required information about the chemical compounds present in plant fruits and seeds were acquired at the beginning of each experiment. The spectrum's characteristics (i.e. the individual peaks and their respective linewidth) helped determine the appropriate measurement protocol for each plant object.

6.2.1 Analysis of vegetable oils and olives

Both analysis of the chemical constitution and visualization of the spatial distribution of saturated and unsaturated fatty acid components in a sample can be performed with the CSI sequence (see Chap. 3). With this technique, the chemical composition of a selection of plant oils, i.e. coconut, olive, rapeseed, and soybean oil, was analysed in detail. Commercially available oils were filled in 5 mm NMR tubes and placed in a 5 mm saddle coil (see Data 10.7) in the Bruker Avance 750 MHz (see Data 10.2) spectrometer.
After the tuning/matching procedure of the NMR coil and the shimming of the B_0 field, the measurements were performed with the following parameters as shown in Tab. 6.1.
In objects with a high degree of liquid compounds (as for example in fruits), the CSI sequence provides high resolution datasets with narrow linewidths in the spectral dimension. Inhomogeneities of the local B_0 field which result in a lineshift of the spectral peaks can be corrected in the data processing and analysis step, thus for each chemical compound, a spatial distribution can be calculated.
For the visualization of the unsaturated FACs in a fruit, an olive was chosen. The CSI sequence parameters were adjusted to the spectral resolution desired for resolving

TR	1,500 ms	FoV	10.0 x 10.0 x 1.0 mm^3
TE	22.75 ms	Matrix	13 x 13 x1 (reco: 128 x 128 x 1)
NA	4	N_{slices}	1
NE	1	BW_{RF}	15,000 Hz
SpecMatrix	2024	SpecRes	7.35 Hz
SWH	14,881 Hz	T_{Acq}	16 min 54 s

Table 6.1: Measurement parameters for CSI experiment of oils. Abbreviations: **TR**: Repetition Time, **TE**: Echo Time, **NA**: Number of Averages, **NE**: number of Echoes, **SpecMatrix**: Spectral points, **SWH**: Spectral bandwidth, **SpecRes**: Spectral Resolution, **FoV**: Field of View, $\mathbf{N}_{slices}$: Number of slices, $\mathbf{BW}_{RF}$: Bandwidth of the RF pulses, $\mathbf{T}_{Acq}$: Total duration of the experiment.

the resonance peaks of the compounds in the fruit. The CSI sequence was applied in the "spin echo mode" to compensate T_2^*-induced signal cancellation in the plant tissue. The spectral resolution was set to 29 Hz, sufficient for distinction of several compounds. The detailed sequence parameters are listed in Tab. 6.2.
Measurements were performed at room temperature and in the dark. A birdcage resonator (i.d. 20 mm) (see Data 10.8) was used for imaging the olive in the Bruker Avance 750 MHz (see Data 10.2) spectrometer.

TR	2,000 ms	FoV	20.0 x 20.0 x 1.0 mm^3
TE	28.16 ms	Matrix	32 x 32 x1 (reco: 128 x 128 x 1)
NA	4	N_{slices}	3
NE	1	BW_{RF}	8,000 Hz
SpecMatrix	504	SpecRes	29.52 Hz
SWH	14,881 Hz	T_{Acq}	2 h 16 min

Table 6.2: Measurement parameters for CSI experiment on an olive. Abbreviations as in Tab. 6.1.

Since this sequence is typically applied for the acquisition of 2D datasets (see Chap. 4.4.2), further experimental approaches were performed.

6.2.2 Chemical Shift-selective Imaging

As mentioned before, the linewidths of the NMR signal peaks in a dry seed are too broad for a detailed analysis (see Fig. 3.5). Via the CSS- (chemical shift-selective) Imaging (see Chap. 4.5), the acquisition of 3D datasets of one chemical compound is enabled.
For the distinct acquisition of the unsaturated FACs, a CSSI sequence combined with

a CHESS solvent suppression module [Haa85] was chosen, as shown in Fig. 4.4. Compound-selective datasets of saturated and unsaturated FACs were acquired by setting the RF pulses of a 3D spin echo (SE) sequence to be compound-selective (narrow bandwidth), i.e. without slice selection gradients during the pulses. A proper chemical selectivity of the solvent suppression and compound excitation pulses was achieved by adjusting the suppression pulses prior to the start of the experiment during the setup procedure. For this, the sample's spectrum was acquired and the effect of the solvent suppression module and of the selected RF pulse parameters was immediately discernible.
The solvent suppression module is applied compound-selectively, thus most of the unwanted signal can be eliminated. Local inhomogeneities in the B_0 field impede a perfect solvent suppression, yet for the broad resonance peaks of the present compounds, this suppression method is sufficient.
In the dataset of the saturated FACs, the solvent suppression was adjusted to suppress the signal from the residual water and the unsaturated fatty acid components. This was furthermore supported by a component-selective excitation of the proton spins in the methyl- and $(CH_2)_n$-groups. Likewise, in the dataset of the unsaturated FACs, the signal from the water protons and the spins in the $(CH_2)_n$- and the methyl-groups was suppressed, the spins in the HC=CH-groups were excited with frequency selective RF pulses.
This imaging scheme was applied to a variety of seeds, to present a method for:

- a large seed model (soybeans)
- a small seed model (rapeseeds)
- the diversity of fruits (coconut flesh and pine nut)
- the storability of seeds (soybeans)

The measurement parameters of the FAC-selective measurements are shown in Tab. 10.1 and Tab. 10.2 in the appendix.
Measurements were performed with resonators fitting to the sample geometry: A solenoid coil (see Data 10.10) for the rapeseeds and the nuts; a saddle coil (see Data 10.11) for the two soybeans of different developmental stage; a Helmholtz coil (see Data 10.5) for the two soybean seeds stored for 1 and for 36 years (same developmental stage). Furthermore, the measurements were conducted on two different NMR scanners, a Varian 600 MHz (see Data 10.3) and a Bruker Avance 500 MHz (see Data 10.1) spectrometer.

The samples were fixated in the resonators, either within an NMR glass tube or a sample holder. The measurements were performed at room temperature and in the dark.
The nuts (coconut and pine nut) were too large to fit into the resonators, thus small pieces of the fruits were cut in shape to be measured simultaneously in one NMR coil. In all experiments all measurement parameters, including the hardware settings "'receiver gain"' and the power of the pulses, was identical for both measurements (sat. and unsat. FACs), thus a direct comparison of both datasets was enabled.
In the experiment of two soybeans from different developmental stages, the images were acquired with different spatial resolutions. Here, the resolution of the "unsaturated" dataset was deliberately decreased in order to avoid a loss of SNR within the voxels. The matching image resolution of both datasets was achieved by conducting a zero-filling by a factor of 2 for the "unsaturated" dataset only.

6.2.3 Data processing

Prior to the CSI dataset, a B_1 mapping was performed for the olive measurement, based on multi-spin echo imaging with additional bipolar Bloch-Siegert pulses applied before the echo train [Stu12]. With an in-house written script, the B_1-map of the resonator could be calculated and was used for correction of the signal amplitudes. For the CSI dataset, an implemented data interpolation was used (available in the sequence protocol), the resulting CSI dataset was imported into MATLAB.
In the olive CSI dataset, the peaks were localized and quantified via a peak-fitting algorithm [O'H12] using Lorentzian shape peaks. After this procedure, the individual peaks were automatically identified and based on the location of the $(CH_2)_n$-peak. The lineshift of all peaks induced by local field inhomogeneities in the plant tissue was retrospectively corrected.
As a result, the area of the peaks from the sat. and unsat. FACs was stored in individual distribution maps. The ratio of both components was calculated in MATLAB, a mask was applied for suppression of the noisy background.
The CSSI datasets were Fast Fourier-transformed via in-house written scripts in MATLAB as during the procedure, a zero-filling (factor 2) was applied. The resulting 3D datasets were exported to AMIRA for an advanced 3D visualization and adjustment of oblique slices through the object. Identical slices within each seed or tissue were selected and exported.

6.3 Results and Discussion

6.3.1 Chemical composition of plant oils

The spectra of the plant oils acquired with the CSI sequence are shown in Fig. 6.1. The main peak, located at -1.2 ppm is attributed to the saturated FACs of the triglyceride molecules. As was explained in Chap. 3.3, the relative intensity of the individual peaks permits an identification and evaluation of the plants oils. The coconut oil is rich in

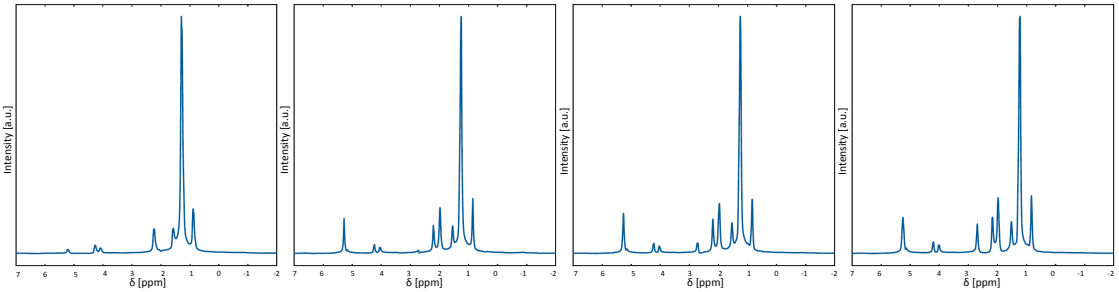

Figure 6.1: CSI spectra of plant oils, from left to right: Coconut, Olive, Rapeseed, Soybean. The saturated fatty acid components are mostly located in the region of -1.2 ppm, the unsaturated components can be found at -5.4 ppm.

saturated FACs and the amount of unsaturated FACs is very low. The content of saturated fatty acids was determined to 92 % [Vig03], thus the peak of the unsaturated FACs at -5.4 ppm is barely distinct.
For the remaining plant oils, the amount of unsaturated FACs is higher than in coconut oil. The amount and type of the fatty acids determines the peak value of the FAC peaks in Fig. 6.1.
In Vigli et al. [Vig03], the Iodine value, IV, was calculated as a measure of the degree of unsaturation. In detail, Tab. 6.3 shows the determined IV values for the four presented oils.

$\mathrm{IV}_{coconut}$	$= 6.12 \pm 0.47$	IV_{olive}	$= 80.58 \pm 1.93$
$\mathrm{IV}_{rapeseed}$	$= 112.99 \pm 0.88$	$\mathrm{IV}_{soybean}$	$= 127.35 \pm 2.27$

Table 6.3: Iodine values of plant oils, determined by [Vig03].

In Fig. 6.1 the peak of the unsaturated FACs, located at -5.4 ppm, increases from the left spectrum to the right. Furthermore, the signal of the protons adjacent to the double bond, located at -2.1 ppm also increases from left to right, underlining the low degree of unsaturation in coconut oil and the high degree of unsaturation in the soybean oil. The protons located between two double bonds in a fatty acid molecule

appear at -2.8 ppm in the NMR spectrum. Polyunsaturated fatty acids contain more than one double bond. The peak at -2.8 ppm reflects the degree of polyunsaturation of the lipidmolecules, in Fig. 6.1 this peak increases significantly from left to right. Here, the soybean oil is the plant oil with the highest amount of unsaturated fatty acids and concurrently with the highest degree of polyunsaturation.

6.3.2 Degree of unsaturation in different seed types

Both MRI datasets ("'saturated"' and "'unsaturated"' FACs) provide spatial information about the particular fatty acid component, enabling a direct comparison between individual seed organs or between simultaneously measured seeds. The ratio map utilizes the previously mentioned datasets to calculate a quantitative parameter ("'ratio"') which can be used to compare ratio-maps acquired in different experiments.
For analysis and comparison of the seeds, in the following the spatial distribution of the saturated and unsaturated FACs are shown, as well as the ratio of both, wherein the ratio of unsat./sat. was calculated.
The distribution of the fatty acid components in the **olive** follows a distinct pattern: From the outside of the fruit towards the seed in the centre, the amount of both FACs rises. In an outer ring of the olive, the signal from the FACs is slightly increased. The signal from the unsaturated FACs is significantly lower than the saturated FACs' signal, but for reasons of visualization, both distribution maps are scaled individually in order to contain the full range of the signal (see Fig. 6.2).
The ratio of both FACs in contrast shows a rather homogeneous distribution of values: no gradient within the fruit is detectable. In the centre region of the fruit a few spots with a decreased ratio (thus less unsaturated FACs) appear, however they are only visible on the left side of the seed.

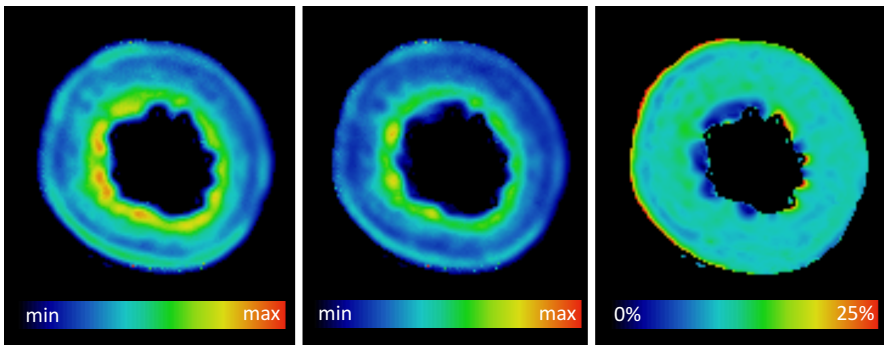

Figure 6.2: Distribution of saturated (left) and unsaturated (centre) FACs, and ratio of both (right) in an olive. Units of colourbar of ratio represent signal ratio of unsaturated to saturated FACs.[1]

In the **soybean** seeds, the lipid is mostly concentrated in the cotyledons, with a distinct gradient towards the centre of the bean. In the radicle, the lipid concentration is reduced compared to the cotyledons, whereby the vascular tissue strand in the radicle posseses a higher concentration of lipid. This distribution holds true for both components, the saturated and the unsaturated FACs, as can be seen in Fig. 6.3.
While the ratio of both components is rather homogeneous within the cotyledons, the developmental stages "premature" (top) and "mature" (bottom) can be distinguished by the higher ratio of unsaturated FAcs in the radicle. The soybean from the "'mature"' developmental stage can be clearly identified by a completely homogeneous ratio of both FACs in the whole bean.

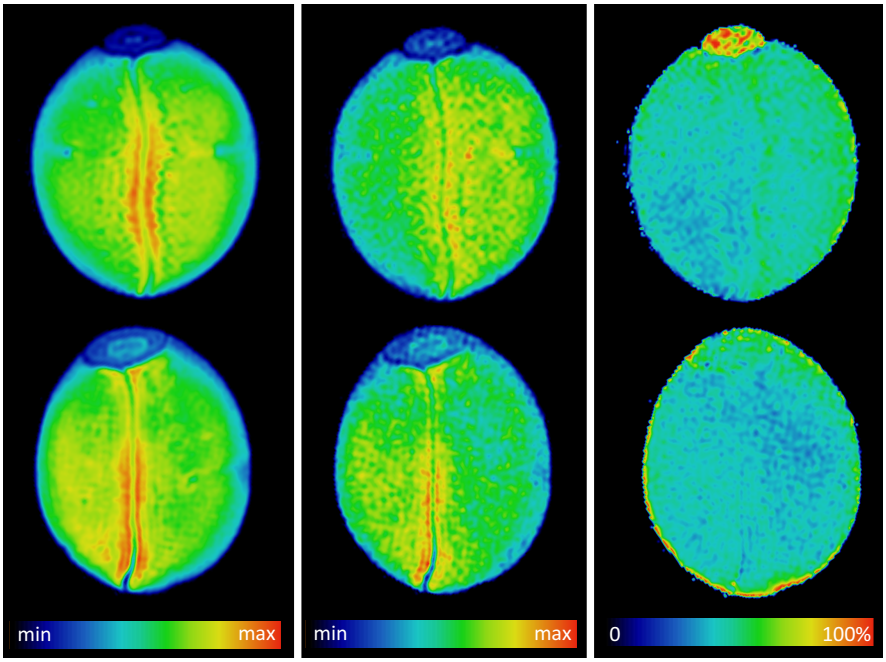

Figure 6.3: Distribution of saturated (left) and unsaturated (centre) FACs, and ratio of both (right) for two soybean seeds of different developmental stages (top: "premature", bottom: "mature". Units of colourbar of ratio represent signal ratio of unsaturated to saturated FACs.[1]

In direct comparison of two **rapeseeds**, the different amount of lipid in both seeds is visible in both datasets of the components (see Fig. 6.4). Within both seeds, the amount of FACs in the outer cotyledons is higher than in the inner cotyledons. The radicle contains typically less or an equal amount of lipid as compared to the inner cotyledon.
Within the individual seed, the ratio of both FACs is constant. Deviations at the edges

[1]The colour range of the unsat. FACs was adjusted for a better visualization.

of the seeds can be attributed to small imhomogeneities of the magnetic field being caused by the change of susceptibility at the transition seed to air.
The ratio of the FACs differs clearly between both seeds, enabling a clear distinction of both seeds in these parameters.

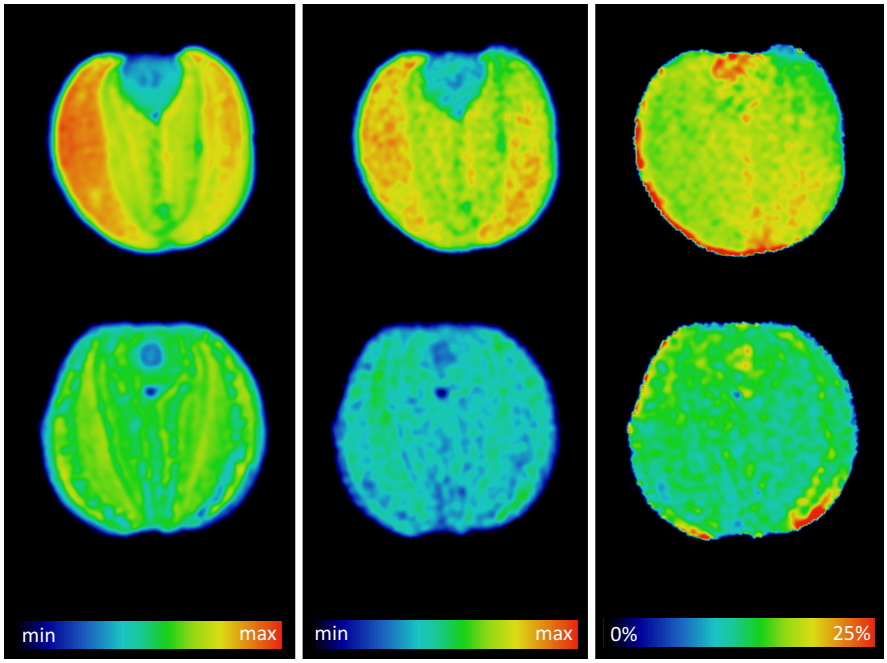

Figure 6.4: Distribution of saturated (left) and unsaturated (centre) FACs, and ratio of both (right) for two different types of rapeseed seeds. Units of colourbar of ratio represent signal ratio of unsaturated to saturated FACs.[1]

The overall amount of saturated fatty acid components in both **coconut** and **pine** are comparable, as can bee seen in Fig 6.5. In contrast, the amount of unsaturated FACs in the pine nut is significantly higher than in the coconut tissue, which can be seen best in the ratio map of both components. While the degree of unsaturation is on a constant level in the pine nut, in the coconut it is close to zero.
The fact that coconut oil contains a fairly reduced amount of unsaturated FACs can also be seen in the NMR spectrum of coconut oil (see Fig. 6.1). Thus, in the calculated ratio map, the pine nut possesses a higher ratio of unsaturated to saturated FACs.
The parameter "Ratio" enables the distinction of different seed types (e.g. coconut & pine nut) and **seeds from different lines** (e.g. two different rapeseeds). When storing seeds, as is done for example in the genebank of the IPK Gatersleben[1], the seeds may be exposed to disturbances such as light, temperature, and moisture, leading to a deterioration of the seed quality. Investigating the seed quality and its germination

[1]IPK Gatersleben, Corrensstraße 3, 06466 Gatersleben

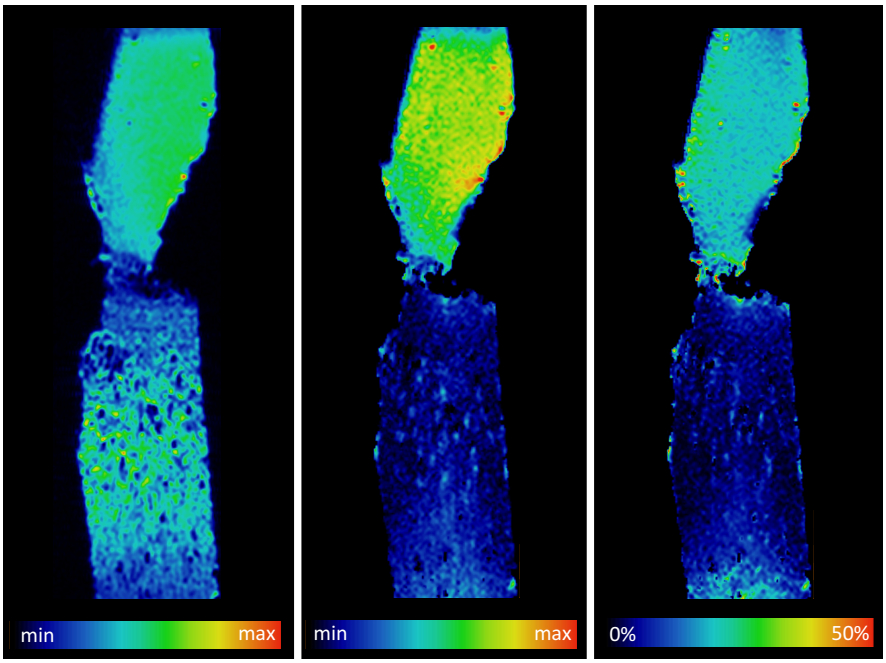

Figure 6.5: Distribution of saturated (left) and unsaturated (centre) FACs, and ratio of both (right) in coconut (bottom) and pine seed (top). Units of colourbar of ratio represent signal ratio of unsaturated to saturated FACs.[1]

capability non-invasively is a major concern of the storage facility.
For the investigation of the **storage condition of seeds**, two soybean seeds taken from the genebank at the IPK Gatersleben: one harvested in 1980 and since then stored in the genebank, and a second seed harvested in 2015. Both seeds were individually measured as described above and their individual FAC distribution maps are shown in Fig. 6.6. Within each soybean two different ROIs were used for further calculations. One ROI was selected in the centre region of the bean (i), where a high concentration of lipid is present. The second region of interest was selected in the cotyledon (o). In both ROIs, the mean ratio (of unsaturated to saturated FACs) was calculated with standard deviation.

$$R_{1980\_o} = 0.1921 \pm 0.0512 \qquad R_{2015\_o} = 0.1936 \pm 0.0418$$

$$R_{1980\_i} = 0.1968 \pm 0.0366 \qquad R_{2015\_i} = 0.1878 \pm 0.0350$$

The results indicate, that no significant change of the ratio unsat:sat FACs has appeared over the range of 35 years. The genebank of IPK Gatersleben is supposed to store the seeds at optimized storage conditions, regarding moisture, air pressure, temperature etc. Thus, the fact that the ratio is unchanged, leads to the conclusion that the storage conditions for this soybean seed had been ideal.

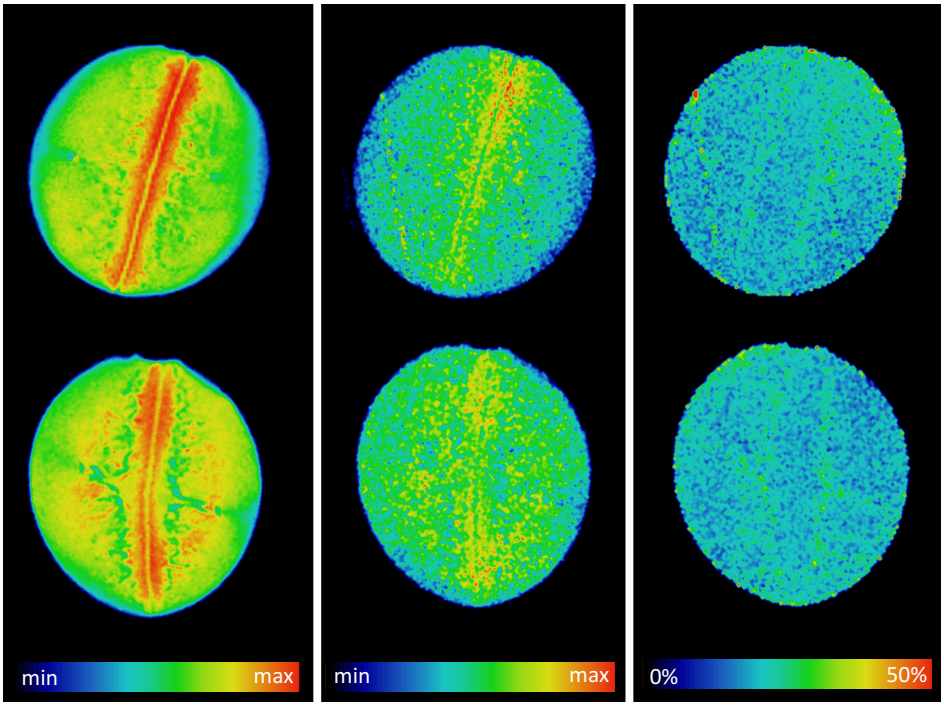

Figure 6.6: Distribution of saturated (left) and unsaturated (centre) FACs, and ratio of both (right) in old (top) and recently harvested (bottom) soybean seed. Units of colourbar of ratio represent signal ratio of unsaturated to saturated FACs.[1]

6.4 Summary and Outlook

Magnetic resonance imaging based on the chemical shift enables a detailed non-invasive analysis of oils, fruits and seeds. The chemical shift selective imaging of the saturated and unsaturated fatty acid components was performed on different seeds and fruits, varying both in lipid content and in size. High-resolution maps of both fatty acid compounds were generated. Within these maps, gradients of both FACs are distinct. Except for the olives, all datasets were acquired in 3D, enabling an analysis of the entire plant object.

The individual FAC maps were used for calculation of the ratio-maps which illustrated the homogeneous ratio of unsaturated:saturated FACs in mature plant tissues. It could be shown that the relative amount of the unsaturated FACs differs in different maturation states of soybean seeds. This fact indicates that the degree of unsaturation of the TAGs is determined during the last maturation stage of the seeds.

The direct comparison of two types of rapeseed seeds uncovered an unequal total lipid amount in both seeds. The more detailed look at the distribution of the FACs revealed that one type exhibits a significantly lower ratio of unsat:sat fatty acid components,

which indicates this property as a characteristic applicable for phenotyping of seeds. The same explanation holds true for the comparison of two small pieces of fruits, pine nut and coconut, both containing a high amount of total lipid. However, the amount of unsaturated FACs differs strongly between both fruits, which is a relevant information about the nutritional value.

The presented method for determining the ratio-maps was used to evaluate the storage conditions of seeds. Identical ratios in long-term stored seeds and recently harvested seeds confirmed ideal storage conditions, since no oxidation of the unsaturated FACs could be detected.

Determining the relative amounts of saturated and unsaturated FACs in plant tissue via chemical shift selective MRI is a technique that provides both nutritional value and information about the sample's storage condition. The calculated ratio map may serve as a phenotypical characteristic since it can be acquired non-invasively. Depending on the plant tissue's composition, different levels of chemical selectivity can be achieved as the linewidths of the spectral peaks correlate with the relaxation times and thus the homogeneity of the plant tissue.

In plant samples with very short relaxation times, different imaging approaches have to be used, as are described in the following chapter.

Chapter 7
Plant imaging with ultrashort echo-times

MRI imaging of plant tissue in ultrahigh magnetic fields is impeded by the short relaxation parameters of some compounds, thus in most imaging sequences they remain unseen. The utilization and adaption of an ultrashort echo-time pulse sequence provided the means to acquire signal from dry and magnetically inhomogeneous plant samples. A variety of new information could be accessed; applications are found, amongst others, in the non-invasive analysis of the starchy endosperm of cereal grains and the imaging of a living venus flytrap.[1]

7.1 Introduction

The water content in various living tissues can be different: some tissues of the human body, such as muscles and kidneys, comprise 79 % of water, whereas bones have only 31 % [Mit45; Piv94].
With the start of clinical imaging it was apparent that tissues with short transverse relaxation times, e.g. the lung tissue, tendons, bones, etc. bear a challenge for magnetic resonance imaging. Little or no signal was accessible with standard NMR protocols such as gradient echo or spin echo, thus these tissues contribute no signal to the MR image acquired with these protocols. The UTE sequence's fast signal acquisition scheme allows for the immediate detection of components with fast transverse relaxation rates. After the publication of the UTE sequence (ultra-short echo time) [Ber91] with its first breakthrough in lung imaging, further applications were soon found in the characterisation of atherosclerosis in the human aorta [Gol93], tendons [Gol95], the human brain [Nay00], the liver [Cha03] and many more organs. The focus in clinical imaging lies on tissues with transverse relaxation times below 2 ms, such as tendons, the cortical bone,

[1] This chapter refers to the article "Insect hapto-electrical stimulation of Venus flytrap triggers exocytosis in gland cells" previously published in Proceedings of the National Academy of Sciences 114.18 (2017): 4822-4827 by Scherzer et al. [Sch17]

dentine and protons bound in proteins [Rob06].
In the department of Experimental Physics V of the University of Würzburg, the UTE-sequence was successfully applied and enhanced for the imaging of the human lung, see [Hem15; Tri15b; Tri15a].
Living plants have relative water contents of around ∼85 % to 100 % under actively growing conditions and do not survive if the water content falls below ∼59 to 30 % [Höf41]. Within the same organism, the tissue water content can differ 10-fold, while at the same time the plant–water relations are tightly controlled [Phi66; Lan12]. Changes in water content of tissues represent physiologically relevant processes, occurring for example during tissue differentiation, development, ageing and seed maturation. While the young plant seed comprises ∼ 80% of water, it dries toward maturation (e.g. mature healthy grains of wheat possess 14.5 %, pea 14.0 % and clover 11.0 % of water). Seeds can dry out without dying [Lep17].
MRI is one of the best technologies for investigation of seed development [Bor12]. In the last three decades since the first imaging of plants via MRI [Bot86], a variety of clinical protocols have been transferred to plant imaging. These always required minor or major adaptations. However, reduction of water content, high tissue heterogeneity and other plant features (e.g. cell walls, gaseous inclusions) cause various susceptibility artifacts. Thus, imaging of seeds at a mature stage is nearly impossible or less informative, if using standard MRI protocols. A diligent approach is required for the successful imaging of such tissues and for detection of metabolites in the living plant at any developmental stage [Mel11; VA84].
The development of a technology which is capable of looking inside dry seeds could provide solutions for various problems in seed science. **Seed quality control**, for example, is an important issue for breeders. An intact seed coat, a well-developed endosperm and the embryo inside of a seed are important prerequisites for high seed quality. Seed quality is largely dependent on the **seed's internal structure and composition**. In the dormant seed, the focus so far has been on the detection and quantification of lipid in the embryo and endosperm [Neu08; Fuc13]. Crossing between breeding lines can cause substantial alterations and disproportions in seed structure, affecting yield and seed quality. Seed quality is also an important issue for ex situ gene banks (which are large stocks of seeds with different genetic backgrounds stored in cold storage rooms). Such gene banks represent an important component for food security for the human population as well as feed stock for animals. Thus, relevant MRI technology could both, **assist breeding** and contribute to **seed quality control in gene bank**s.
Plant productivity is greatly affected by abiotic stress [Boy82]. A relevant approach in

breeding and biotechnology is therefore the generation of stress-resistant crops [Ale12]. For example, a large proportion of yield from wheat, barley and rye is lost due to logging, and the mechanisms involved are still unknown. Application of non-invasive technology, like MRI, could be a great support for approaching architecture and physical properties of **logging-resistant** versus sensitive plants, thereby to identify key aspects of logging resistance. Some plants are able to survive adverse environmental conditions. For example, resurrection plants can lose over 95 % of their water content and return to full activity upon rehydration [Far11]. Development of methods, like UTE, could contribute to study of **mechanisms of resurrection** and improvement of **drought tolerance** [Fit15] by visualization of structural and dynamic processes in these plants.
On account of imaging of very fast-relaxing compounds, a technique capable of acquiring the fast decaying NMR signal was required. A reduction of the echo time, compared to spin echo sequences (with echo times of approximately 3 to 7 ms), can be achieved by applying a gradient echo sequence (TE approx. 1 to 3 ms). Nevertheless, for the imaging of dry components such as starch, the echo time has to be further reduced. By omitting time-consuming components in the NMR pulse programme (e.g. phase encoding and read dephasing gradients), the echo time can be reduced towards the limits of the hardware, typically in the range of 10 to 100 μs.

7.2 Material and methods

The need for spatial encoding during data acquisition results in an imaging technique with the data acquisition starting immediately after the excitation pulse. At the same time the imaging gradients are turned on and rise to their respective amplitude, see Fig. 7.1. The read encoding is now applied radially, thus data acquisition in k-space starts in the centre and it is only limited by the echo time TE.
The contrast in the UTE images can be T_1- or spin density weighted. Different to the implication by the name UTE, no echo is generated by pulses and/or gradients and the acquisition is focused on the fast-decaying NMR signal. Typically, the TE is ranged between 10 to 100 μs, depending on the hardware specifications. Signal suppression from compounds with relatively long relaxation times (moisture, lipid, etc.) is achieved by selecting a repetition time of about 50 to 100 ms, thus inducing a strong T_1-weighting for those compounds.
Multiple applications for the UTE sequence are found, in clinical imaging, the sequence is mostly used for the investigation of tissues with short relaxation times due to strong spin-spin-interaction (e.g. bones [Rob03]) or in magnetically rather inhomogeneous tis-

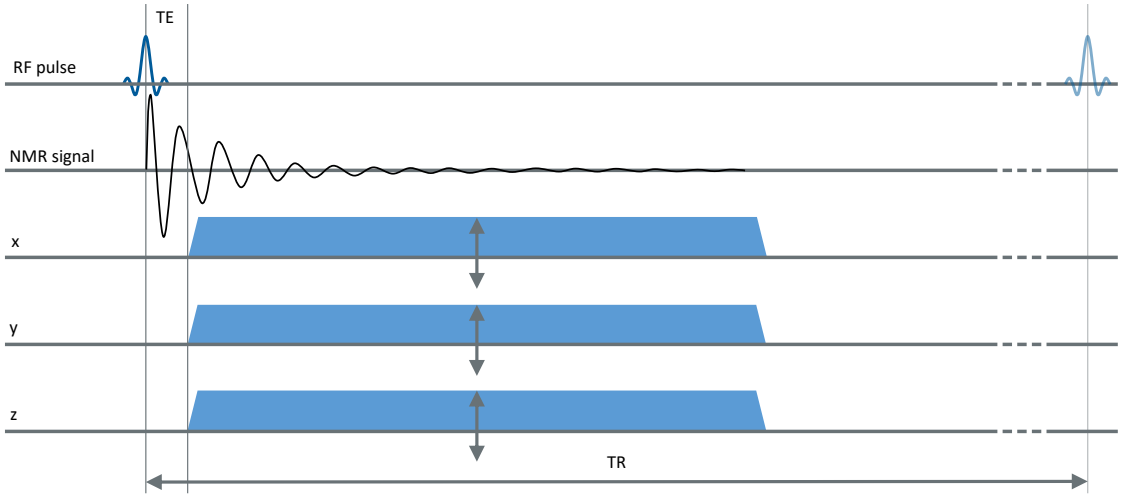

Figure 7.1: Pulse programme of the UTE sequence. After a hardware dependent echo time TE, the gradients required for spatial encoding acquire the fast-decaying NMR signal created by the excitation pulse.

sues, caused by susceptibility changes due to air inclusions (e.g. lung [Ber91; Tri15a]). A disadvantage of the UTE sequence is its non-selectivity: The excitation of fast-decaying components requires a relatively short pulse in the time domain, so the magnetization is not decaying while the pulse is being applied, as would be the case with component-selective pulses which are typically applied to compounds with low relaxation rates. Thus, the short RF pulse is wide in the frequency domain.
On the other hand, the imaging with UTE offers a variety of possibilities, the application of the UTE sequence to the imaging of plants is presented in this chapter.
The UTE experiments were performed on the Bruker 500 MHz scanner[2]. The measurements were conducted with custom-built coils (5 mm Helmholtz coil (see Data 10.5) and 15 mm birdcage coil (see Data 10.6)) suitable for the sample's dimensions.

7.2.1 Sample preparation

The UTE sequence is capable of acquiring an NMR signal from fast decaying components, thus the handling and the fixation of the sample has to be well-considered. Undesired artifacts can be caused by the utilization of adhesive tapes for fixation of the sample, since the adhesive component is visible in the UTE dataset. Even some plastics and rubbers, depending on their treatment with softeners, may contribute to the NMR signal [Fab14].
Fixating the sample in the coil requires dry materials such as paper or cotton wool.

[2]For details see Data 10.1 in the appendix

The dry samples (wood, seeds, powders) were placed in glass NMR tubes and plastic tubes that were found to cause no severe image degradation. Experiments were conducted with the 5 mm Helmholtz coil in the Bruker AMX spectrometer.
While the seeds were simply placed within dry materials, the venus flytrap was taken out of the soil and the other flytrap leaves were removed from the stem. The separated venus flytrap then was placed in a 15 mm i.d. plastic tube filled with a nutrient solution to avoid dehydration of the living plant. After the application of coronatine, a hormone capable of triggering the plant's closing and digestion mechanism, a reference spin echo experiment and the consecutive UTE measurements were started. In this experiment, the 17 mm Birdcage coil and the Bruker AMX spectrometer were used.

7.2.2 Method adjustments for application in plants

The implementation of the UTE sequence on the Bruker scanners in the Department of Experimental Physics 5 at the University of Würzburg was performed by P. Winter during and after his diploma thesis [Win11].
The sequence features an anisotropic Field of View, enabling a reduction of the measurement time for elongated objects. To achieve an effective coverage of k-space data a cone-based trajectory designed for anisotropic FoVs was used [Lar08].
Detailed information about the applied sequence parameters are shown in Tab. 10.3, Tab. 10.4, and Tab. 10.5 in the appendix.
Measurements were conducted using a custom UTE sequence with a 10 μs block pulse and an TE of 0 μs or 10 μs delay time between the excitation and the start of the acquisition. For excitation, a flip angle α of 15° was used. The frequency encoding was conducted by acquiring 128 readout points with a sampling bandwidth of 200 kHz and a repetition time of TR=50 ms. Depending on the sample geometry a set of 54,500 (barley seed) to 63,000 (pea seed) radial projections was acquired. The ramp time of the encoding gradient was 100 μs.
3D images of the plant material were reconstructed at a resolution of 65 μm (barley seed) to 125 μm (proteins and starch) with convolution gridding [Fes03] using the toolbox proposed by Fessler et al. [Fes17]. For this, the radial trajectory was measured before all experiments [Duy98].
The measurement time of one dataset was in the range of 1.6 h (Venus flytrap) to 19.5 h (wheat seed).
For the separation of components in the barley seed based on the calculation of a two component T_2^* map, multiple datasets with varying TEs were acquired, ranged between 20 μs and 1250 μs. Here, the repetition time, TR, was set to 100 ms and the number of

averages, NA, was set to 2.
Spin echo datasets for comparison to UTE-imaging were acquired with a standard Multi-Slice Multi-Echo (MSME) spin echo Sequence with the following parameters: TR = 500 ms to 1,000 ms, TE = 4.4 ms to 9.3 ms, isotropic resolution 65 μm to 120 μm. The measurement time was in the range of 1.4 h (Venus flytrap) to 12.5 h (Thistle stem).
All reconstructions were done in MATLAB (The Mathworks, Inc., Natick, MA, USA) and zero-filled in order to provide a higher effective spatial resolution. The three-dimensional segmentation of the wood was achieved with Amira (Mercury Computer Systems, Chelmsford, USA). The bi-exponential T_2^* fit was performed based on a least-squares-algorithm, the resulting datasets were visualized in AMIRA.

7.3 Results

In this section, the datasets acquired with the UTE sequence are presented. As a comparison to the standard imaging capabilities, spin echo datasets with comparable measurement parameters (measurement time and/or image resolution) are shown. The spin echo datasets represent the 'gold standard' of plant imaging, since the least amount of plant imaging experiments are performed with gradient echo sequences. Accelerated sequences, such as the RARE[3] [Hen86], which use the following echoes after the first spin echo for imaging, suffer from the relatively short relaxation times in plant tissue and thus are rarely used.

7.3.1 Seed imaging at quiescent stage

The magnetic resonance imaging of seeds has been performed since 1987 [Con87], yet most experiments concentrate on the localisation of the distribution of water or lipid within the seeds. In the latter experiments, the acquired information about the relative amounts of lipid in the embryo, the endosperm, and the aleurone layer was sufficient for comparisons between wildtypes and cultivars [Kov16] or different developmental stages [Woo17]. Further substances (starch, sugars, proteins, etc.) could not be imaged directly and were thus ignored.
The UTE sequence is now capable of detecting more information originating from the sample, as is demonstrated in Fig. 7.2. The gain of information is clearly visible: the structure of all seeds is now distinct and accessible in the three-dimensional dataset.

[3]Rapid Acquisition with Relaxation Enhancement; also: Turbo Spin Echo, TSE; Fast Spin Echo, FSE; or Rapid Spin Echo, RSE

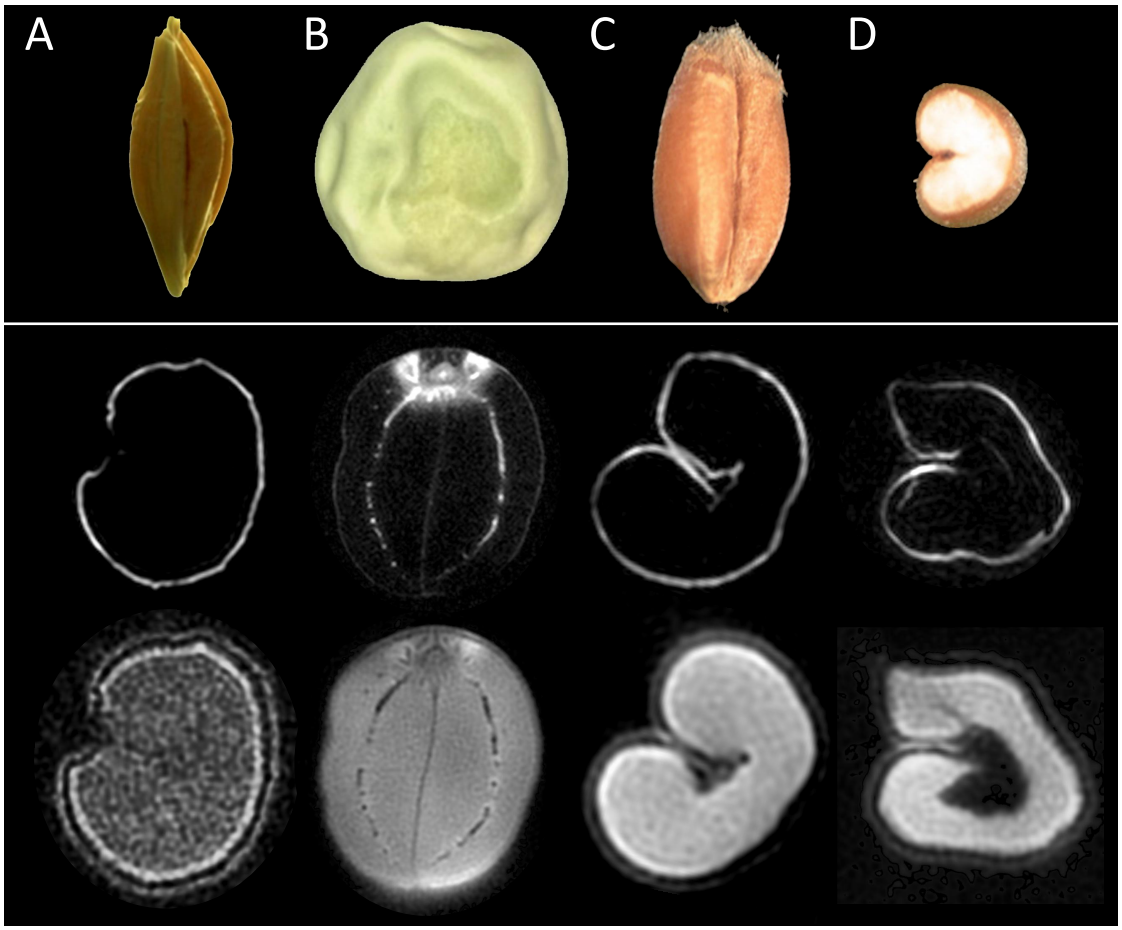

Figure 7.2: Dry seeds (top row), acquired with spin echo (center row) and UTE (bottom row) sequence. **A** Barley seed, **B** pea seed, **C** and **D** wheat seed (section shows normal wheat seed and cross section). The spin echo sequence can only detect and visualize the lipid-rich tissues, while the UTE sequence can acquire signal from the endosperm and the seed coat.

Even though the 3D spin-echo (SE) sequence was set up for the shortest possible echo-time TE (wheat: TE = 4.3 ms), in the SE-images (see Fig. 7.2, top row) only the lipid stored in the seed's embryo and the aleurone layer is visible. The endosperm and the pericarp contribute no detectable signal to the final image. A quantification of the lipid is possible [Neu08] but further analyses cannot be performed. Information about the volume of the seed, the inner structure or the seed's organs are inaccessible and require other analytical methods like mass spectroscopy imaging, histological staining procedures etc.

The UTE sequence in contrast delivers a detailed insight to the dry seeds' anatomy (Fig. 7.2, bottom row). The images show the endosperm of the seeds, which mostly consist of starch. The seeds' outer layers are recognizable and rich in contrast to the

background. In all seeds, the individual components (endosperm, aleurone layer, and the seed coat) are distinct.
The advantage of the acquisition with ultra-short echo times is most clearly observed, when analysing the wheat seed with a cavity: this seed was selected for the NMR experiment, since it attracted attention in routine seed analyses. Its volume is significantly increased as compared to other *Triticum* seeds, yet the weight and thus the density were both too low compared to the expected values. The spin echo imaging, focusing on the lipid distribution in the seed, revealed no interesting details, except of the unusual shape.
The non-destructive application of the UTE sequence uncovered the cavity inside the seed's endosperm. This was created during the maturation process, whereby the seed ripens from the outside towards the centre. Since this seed was from a special breeding, the starch producing process was terminated prematurely, thus the cavity inside the seed remained. This feature was inaccessible for most analytical methods, since this seed was not supposed to be destroyed. In this case, the non-invasiveness of the MRI method could reveal the effect of an unfinished ripening process in the seed.

7.3.2 Leave dynamics of carnivorous plant

The utilization of the UTE sequence in the imaging of living plants was required for the venus flytrap (*Dionaea muscipula*). Although impressive high-resolution datasets of plants can be acquired with MRI, some tissues cannot be imaged with a standard sequence such as spin echo or gradient echo. As previously mentioned, the imaging of plants is impeded by susceptibility artifacts caused by the inhomogeneous tissue. The magnetic inhomogeneity in the plant's trap leaves is responsible for the deteriorated image quality in the spin echo dataset, see left image in Fig. 7.3. After adaption of the UTE sequence, the full structure of the venus flytrap is distinct, even the hair-like cilia at the end of the trap's leaves can be seen (see right image in Fig. 7.3).
With this sequence at hand, the digestion process of the venus flytrap was monitored. Over the course of the experiment (in total 11 days), the closing of the flytrap and the filling of the trap cavity with the digestive fluid were monitored, as seen in Fig. 7.4. Since this process was not triggered by a living insect but through application of a hormone, the closing of the trap leaves starts after approximately two days and is completed after approximately three days after the start of the experiment. The secretion of the digestive fluid start after the closing procedure and fills the cavity of the trap. The venus flytrap was continuously monitored for the duration of 11 days.

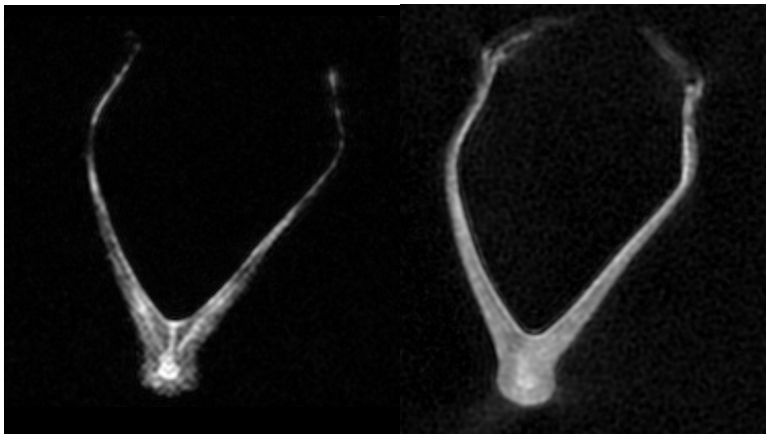

Figure 7.3: MSME (left) and UTE (right) images of a venus flytrap plant. The spin echo image suffers from the fast signal loss in the plant tissue. The hair-like cilia at the outer end of the leaf are only distinct in the UTE dataset.

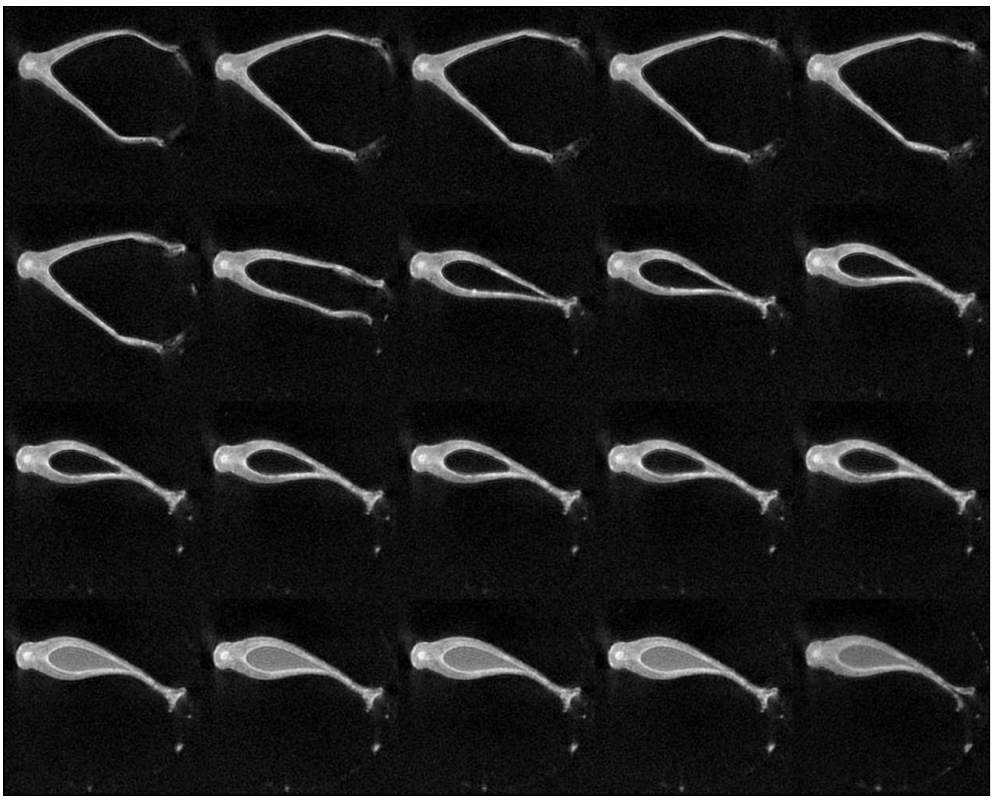

Figure 7.4: Axial images of a closing and digesting venus flytrap, acquired with the UTE sequence. After the complete closing of the trap leaves, the digestive fluid fills up the cavity. The time-lapse images comprise a period of 11 days. A video of the digestion sequence was published in [Sch17].

7.3.3 Wood imaging

The potential of the UTE sequence can be demonstrated on the imaging of a piece of dried wood taken from radiata pine (*Pinus radiata D. Don*). The wood was cut in a cubic shape in order to fit into the sensitive volume of the coil. For demonstration purposes, a hole was drilled in one side.
While the Spin Echo sequence was not able to acquire an image of the dry piece of wood, the UTE sequence can display its complete structure, see Fig. 7.5.

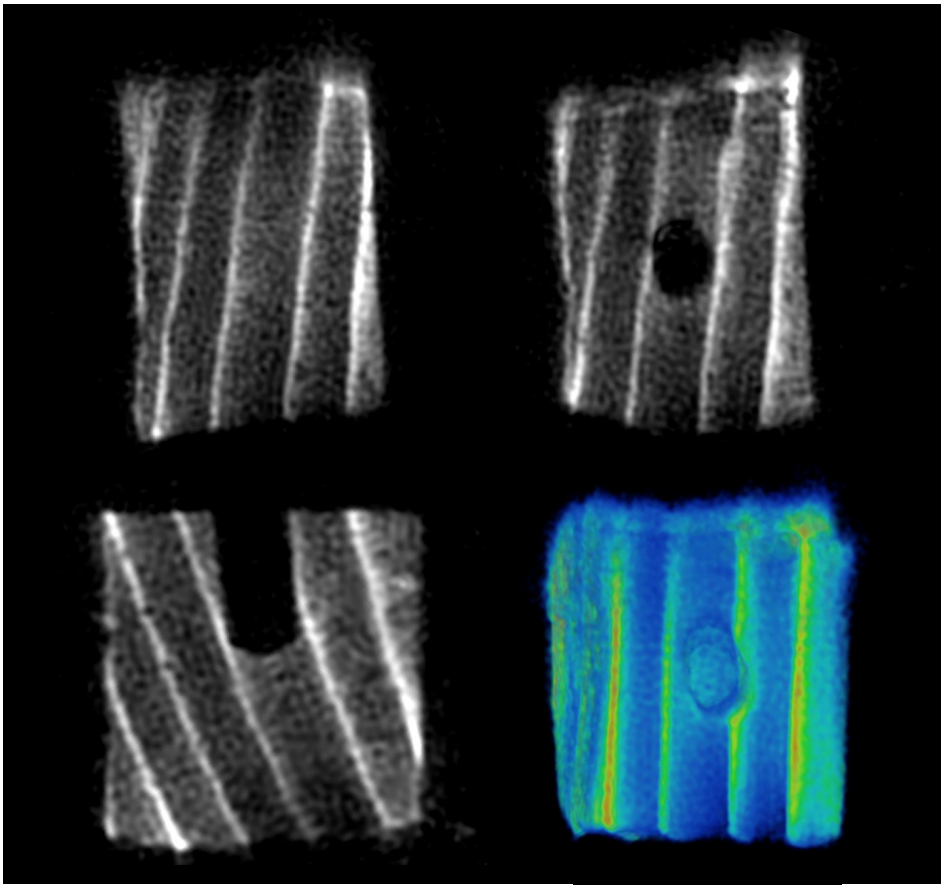

Figure 7.5: UTE imaging of dry wood containing a drilled hole, shown are three slices through the cube and a three-dimensional rendering. Latewood and Earlywood can be differentiated and the drilled hole is distinct.

In the two-dimensional slices, the wooden cube and the drilled hole are discernible; the outer shapes of the object are clearly visible. Inside of the wood, the two different tissue materials can be identified as latewood (bright) and earlywood (dark). The three-dimensional rendering of the acquired object provides a detailed overview of the wooden cube.

7.3.4 Tissue composition

In order to answer the question, which compounds contribute to the signal in the UTE dataset and which compounds don't, three major constituents of plant seeds, proteins, sugar and starch, were analysed separately. First, all substances were measured with the UTE sequence (humid dataset). After a period of 48 h within a desiccator to remove residual moisture from the protein crystals, the sugar crystals and the starch powder, a set of dry samples was measured again (dry dataset). The results of starch and proteins are shown in Fig. 7.6. no signal could be acquired from the sugar crystals.

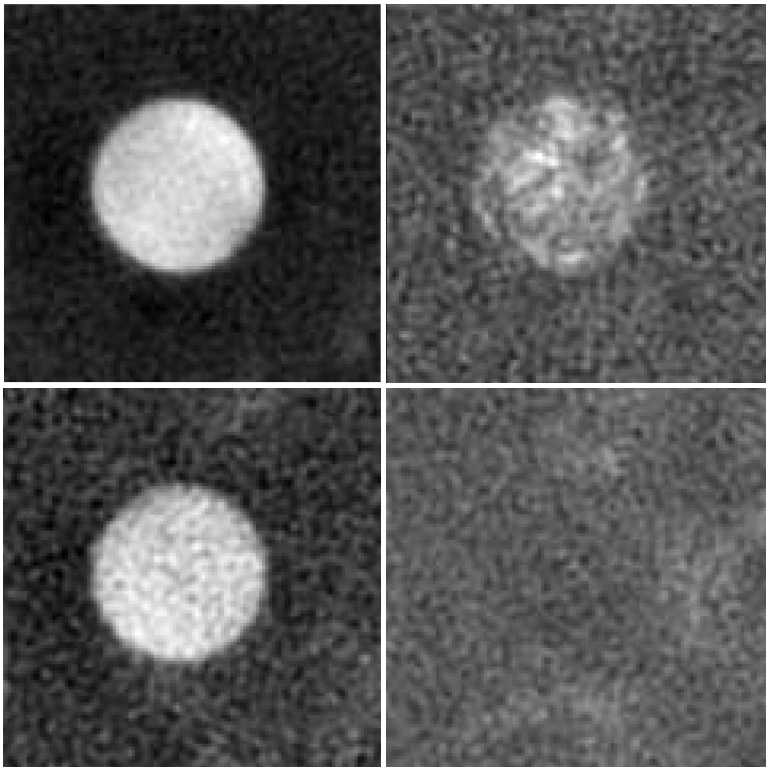

Figure 7.6: UTE images of starch (left) and proteins (right). The top row shows the samples before the drying procedure, the bottom row after 48 h of drying in a desiccator. The dry starch still provides sufficient NMR signal while the proteins are no longer detectable.

For a better visualization, the data reconstruction matrix had to be reduced in order to improve the SNR in the images. In the humid dataset, in contrast to the protein crystals, the starch powder provides enough contrast. Both substances can be detected and the shape of the glass tube can be estimated.
After the 48 h drying period, the dry starch is still detectable in the UTE image, yet with a significantly reduced signal, recognizable in the lower SNR. In the image of the

dried proteins, only noise can be seen, the sample itself no longer contributes to the NMR image.
This result indicates that the major contribution in the UTE datasets, except from residual moisture, is the starch contained in the endosperm of the crop seeds.

7.3.5 Separation of components based on T_2^* mapping

The results of a bi-exponential fit calculated from a barley seed dataset are displayed in Fig. 7.7.

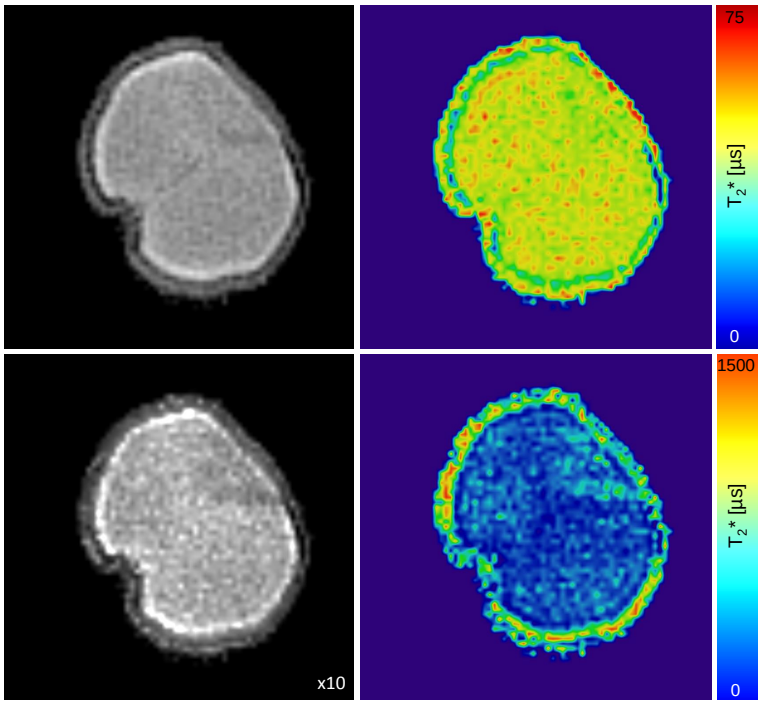

Figure 7.7: Separation of components based on T_2^*-mapping. Two components could be identified, a short-relaxing component (top row) and a component with a relatively long relaxation time T_2^*. The left column shows the M0 map of both components, the right column the T_2^* maps. The M_0 map of the components with the long T_2^* value had to be scaled in intensity by a factor of 10.

Two components could be separated with this T_2^* mapping, their M_0 maps are shown in the left column of Fig. 7.7. While both components possess a comparable distribution in the seed, their T_2^* times are significantly different. The components with the long relaxation time present in the seed are presumably water and lipid, while the starch, as the previous measurements in Sec. 7.3.4 indicate, is characterized by a relatively short relaxation time. Thus, the component in the top row of Fig. 7.7 is identified as starch,

while the component(s) shown in the bottom row is identified as (bound) water and/or lipid, which are only present in a relatively low concentration since the intensity in the M_0 map had to be scaled by a factor of 10 to match the other component's intensity. Thus, in the dry barley seed, the UTE signal mostly originates from fast relaxing components.

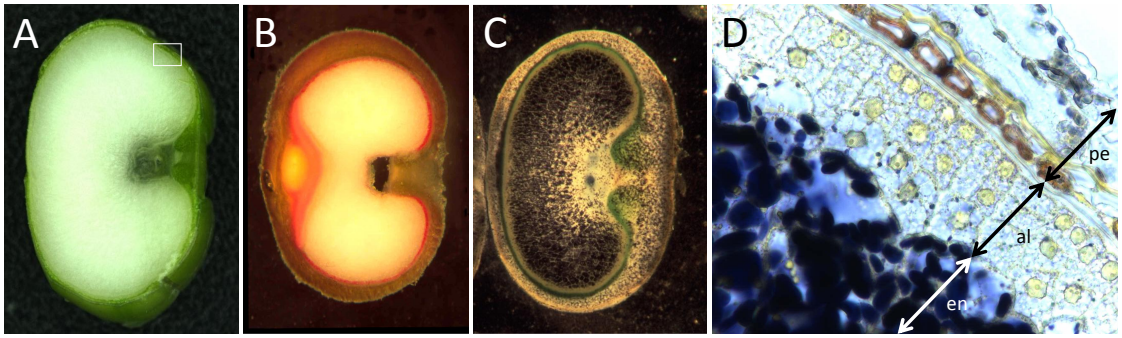

Figure 7.8: Histology of a fresh barley seed. (A) Cross section through a fresh seed. (B) Lipid staining with Sudan III showing the lipid (red) distribution within the seed. (C) Iodine staining of starch, which appears dark blue / black. (D) Fragment of a semi-thin section of the barley seed (inset in A) shows the three regions of the seed: the starchy endosperm (**en**) which is followed by the aleurone layer (**al**) containing lipid. The seed coat, the pericarp (**pe**), consists of multiple cell layers with a small fraction of lipid.

The staining of plant material can only be accomplished on fresh, thus water containing, samples. Performing a dissection on a dry seed would cause the sample the sample to be destroyed; thin slices cannot be produced. In Fig. 7.8 a section of a fresh barley seed is shown, with the according stainings of the lipid and the starch distribution within the seed. A high-resolution microscopy image provides a more detailed insight into three regions of the barley seed. The endosperm containing most of the starch and, in its outer region, also some lipids. The aleurone is a thin coating layer around the endosperm, in the inset three cell layers can be distinguished, all of them containing a large amount of lipid. The outer seed layer, the pericarp, consists of several layers and by a small fraction also of lipid and starch.
The comparison of the histology of a fresh seed (Fig. 7.8) and the results from the T_2^* mapping (Fig. 7.7) underline the capabilities of the UTE imaging protocol; the distribution of the starch calculated with the UTE T_2^* mapping method matches the starch distribution visible in a fresh seed. The lipid layer in the outer region of the endosperm contributes signal in both T_2^* maps, which might be caused by fast and slow relaxing fatty acid components present in a singular TAG molecule. The starch accumulated in the pericarp is also clearly visible in the map of short T_2^* times.

The slowly relaxing components, identified as bound water and lipid, both appear bright in the map of long T_2^* times. The semi-thin section in Fig. 7.8 shows the high concentration of lipid in the aleurone layer and, to a lesser extent, the accumulation of residual lipid in the endosperm tissue.

7.4 Discussion

Even though magnetic resonance imaging of plants has been performed for three decades, the UTE sequence has, to my knowledge, not been applied to plants and seeds.
In dry seeds, the unambiguous advantage is the visualization of the starchy endosperm and the pericarp.
The magnetically inhomogeneous plant tissue, as seen in the venus flytrap, impedes the imaging with standard sequences, yet the UTE sequence is able to acquire high-resolution datasets in an acceptable amount of time. This enabled the visualization of the digestive process of a venus flytrap, triggered by a hormone that was applied in advance.
In dead plant material, such as wood from a radiata pine, the UTE sequence provides sufficient information to distinguish the two types of wood present in the sample (latewood and earlywood). Furthermore, the hole drilled into the wooden piece could clearly be seen. This technique provides the means to investigate materials usually not visible with standard MRI protocols. One application for the imaging of wood could be the quantification of woodworm infestation in antique furniture.
The identification of the formerly unseen signal in the UTE images could be attributed to two major components; firstly, residual moisture present in most organic materials. While this bound water content in dried wood is in the range of $\sim$15 % [Rat15], it is a major contribution when the main component is typically not visible in magnetic resonance imaging. Secondly, the starch could be identified as a predominant source of the acquired NMR signal in dry seeds.
Further signal contributions originate from free water and lipid in tissues; these contributions can easily be identified when a standard imaging sequence is used.
The utilization of a T_2^* mapping technique enables the separation of multiple components present in the sample based on their relaxation times. In the resulting M_0 maps, the spatial distribution of these components can be visualized and thus identified. This technique is, in contrast to common visualization techniques, a non-destructive approach.

7.5 Conclusion

In this chapter, it has been shown that the application of the UTE sequence in plant imaging offers a more detailed insight into the plant anatomy, as compared to standard magnetic resonance imaging. The decreased chemical selectivity of the UTE sequence is a major drawback. In the first experiments, it could be shown that the signal acquired in a dry seed mostly originates from protons attached to bound water molecules and starch. In further analyses, namely the T_2^*-mapping, the individual distribution maps of two components provided a more detailed insight into the investigated plant tissue.

Chapter 8
Dynamic T_1-mapping and determination of translocation velocity of a contrast agent in planta

*Important information about the properties of water/metabolite allocation in plants and animals is provided by the noninvasive identification and evaluation of vascular tissue. By adaption and transfer of distinct medical nuclear magnetic resonance (NMR) approaches to plant science, the vascular anatomy and functionality of plants can be obtained. Here, the novel **b**otanical **a**pplication of a **c**ontrast agent for **a**scertaining **r**eallocation-processes via **d**ynamic-contrast-enhanced magnetic resonance imaging **i**mitation (BACARDI) is presented. It is tailored to the challenges posed by plant imaging and takes advantage of the in clinical imaging widely used non-toxic Gd-DTPA contrast agent (CA). T_1-maps with improved temporal resolution at a consistently high spatial resolution, sufficient for the investigation of living plants, are calculated by analysing changes in NMR signal induced by uptake of the CA.* [1]

Preface

The vascular system delivers assimilates produced by photosynthesis in leaves to the developing fruits/seeds. It largely connects all plant organs and also delivers hormonal signals and protein- and RNA-based messages. Thereby it enables the coordination of physiological and developmental processes at the whole organism level [VB13]. With the water flow, organic molecules of different size and features are forced along the

[1] This chapter refers to 'Kontrastmittelgestützte T_1-Messungen zur Untersuchung des Nährstofftransportsystems von Pflanzen' (Zulassungsarbeit für die Staatsexamensprüfung) written by S. Hammer in the department EP5 of University Würzburg under supervision of E. Munz [Ham15]

vascular vessels and channelled from the point of origin toward the location, where they are accumulated or enter the metabolic process.
Although the molecular basis of metabolite allocation has been studied intensively, little is known about dynamic of various individual compounds traveling with the water flow. Existing models characterize the main forces determining nutrient transport [Mün30], but they are incapable of answering the questions about the velocity of distinct substances (e.g. proteins, carbohydrates and etc.) along the vascular system and in relation to functionality (metabolism), architecture or developmental stage of tissues/organs. It is shown, that the structural-functional characteristics of the vascular system differ among the species, alter during the development of plant organs (and especially fruits) and thus require rather specific approaches [Kel06; Nob00]. The allocation pattern of distinct metabolites, the direction of translocation and intensity of flow are largely determined by the sink-source interactions [Cho09].
In plant sciences, the most popular technologies for non-invasive survey are X-ray, PET, and NMR. The potential for detection of metabolites using X-ray is extremely limited and thus renders x-ray based approaches less appropriate for metabolite analyses. The most powerful tool is PET, it has shown to be able to visualise sucrose in plants and various compounds in animals. This technique requires radioactive labelling of molecules and thus excludes long term experiments on developing organisms and especially on developing fruits or seeds. For the long time observation and dynamic survey of both plant and animals, NMR-based appear to be most appropriate due to minimal deposition of energy in the observed tissues.
For a long time, the lack of suitable technology has hampered systematic in vivo investigations of nutrients allocation inside of vascular system and understanding plant metabolism and adaptations to changing environmental conditions [Kno10]. Thus, further developments of NMR for plant are required, which enable to visualize the specific distinct metabolite in context of tissue structure, measure their concentration and characterise the dynamics in living plants.

8.1 Introduction

In animal and medical sciences, functional imaging and various measurements techniques for vascular survey and measurements of solute dynamic are available for many years. MRI-based angiography evolved to a fast developing branch of noninvasive diagnostics. A direct technology transfer between the medical- and the plant-biological applications field are prevented by substantial differences in physiology, metabolism and structure of plant and animal tissues [Bor12; Köc01; Sta05; Nar11].

In higher animals and human for example, the forces causing fluid to move inside of vascular system are generated by specialised organ –heart- and flow velocities are high. In the normal human cava, it is ranged from 10 to 45 cm/s [Wex68]. To the best of my knowledge, the flow velocities in plants are up to thousands-fold lower (!) and thus are measured in milimeters per second (mm/s) or per hour (mm/h) [Rol15b]. Transpiration and sink-source exchange and other interrelated processes drive the movement of fluids. Some processes are also light dependent or environmentally controlled (e.g. temperature, water availability and etc.). The prediction of the dynamic of distinct/individual metabolic compounds is nearly impossible, due to the number of unknown mechanisms involved in controlling the metabolite allocation (e.g. exporter and importer activities, existence of channels, sieves and pores) and acting along the metabolite translocation route.

The translocation of sucrose between maternal and filial organs was visualized just a few years ago in grain using ^{13}C-labelled sucrose [Mel11; Rol11; Fuc15]. In plant biology, using an isotope–labelled molecule is a widely used approach. Besides ^{13}C, other isotopes are used, as for example 15N, 22S, and etc. Unfortunately, detection sensitivity of NMR for these isotopes is very low [Lev08; Fri13].

In the praxis of magnetic resonance imaging, various other types of labelling can be used which could be useful for applications on plants, but are not experimentally tested or considered as not appropriate (review). By Dean et al. [Dea17] the indirect observation of paramagnetic manganese (Mn) ions in mature grape berries via relaxation MRI recently was performed. Mn is considered as a toxic ion and thus is less appropriate for long time experiments. Nevertheless, the paramagnetic gadolinium (Gd) ion both in its chelated and unchelated forms is non-toxic for plants [Qui90]. It could enter the root cell symplast and it moves in conjunction with the solute flow which enables tracing it in living plants [Gus01; Zha09; Gri17].

In this chapter, a Gd-based tracer was applied to trace the dynamic of transport processes in two different plant models: barley (*Hordeum vulgare*) and canola (*Brassica rapa*). The experiments resulted in the development of a new NMR-based method for plants, called BACARDI (**B**otanical **A**pplication of a **C**ontrast agent for **A**scertaining **R**eallocation-processes via **D**ynamic-contrast-enhanced magnetic resonance imaging **I**mitation). Some basic features of BACARDI originate from Dynamic Contrast-Enhanced (DCE) magnetic resonance imaging [Tof91], a technique well-known in clinical diagnostic. It relies on the paramagnetic features of a contrast agent and, in contrast to PFG (pulsed field gradient) NMR experiments, BACARDI possesses a feature advantageous for plant applications: It is capable to operate in a very low velocity range, and furthermore provides the means for concentration measurements. Thus, BAC-

ARDI represents an original solution for the investigation of the dynamic of molecules travelling with water flow inside of living plants.

8.2 Material and Methods

8.2.1 Magnetic resonance imaging

The experiments were performed on the Bruker 750 MHz scanner[2]. The determination of the contrast agent's relaxivity and the plant MRI experiments were performed with a custom-built 20 mm inner diameter birdcage coil, all experiments were conducted at room temperature and under illumination of the plants.

8.2.2 Preparing the plant for the MRI measurement

Via the peduncle, the upper region of the stem, the allocation of water and metabolites to the spike in barley plant occurs, it is driven preferentially by transpiration (green husk) and sink activity of growing grains [Rol15b]. Inside of the stem tissues, the vascular bundles are hidden and become visible by dissection of the stem (Fig. 8.5). For observation of the tracer's movement in this region, two stems of barley were cut off approximately 15 cm below the peduncle and immediately placed into 5 mm NMR glass tube filled with liquid media; as a reference point during the experiments, an additional 3 mm glass tube (filled with water) was inserted. The setup was fixated using Teflon tape and positioned inside the NMR coil, the injection of the contrast agent was performed via a tubing without touching the setup, see Fig. 8.1. The canola seeds grow inside a silique, it is in elongated fruit (Fig. 2.1B and Fig. 8.1), its internal structure is shown in Fig. 2.1. Inside the silique, two compartments may be observed, its wall is not entirely uniform and consists of two halves, which are large, green, and photosynthetically active and one thin middle wall (septum), which bears the seeds. The seeds are attached to the septum by stalks (funiculi), which are located along the merging of the septum. The approximately two cell layers wide dehiscence zone spans the length of the silique between the valve and the replum (for review, see [Fer02]). The vascular net transfers solutes, it is embedded inside the parenchyma tissues and thus only visible after dissection of the silique Fig. 2.1C. For localization of the vessels inside of the intact silique via MRI, the silique was separated from the stem and placed in an NMR-tube filled with liquid media, as described above.

[2]For details see Data 10.2 in the appendix

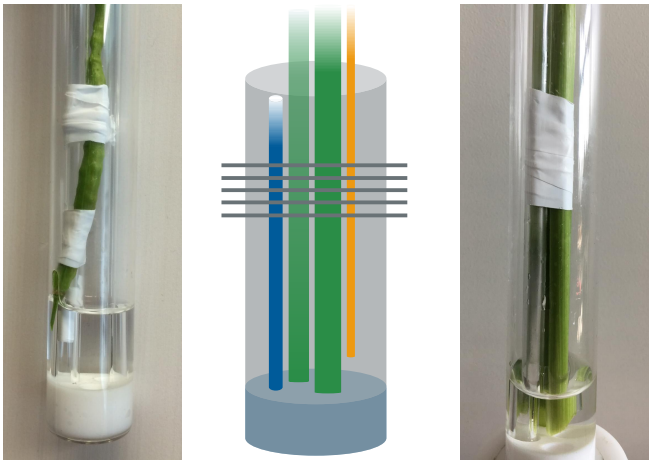

Figure 8.1: Experimental setup for the BACARDI measurements. Left: rapeseed silique, right: barley stems. Centre: scheme of setup, exemplified in detail for the barley stems: The two stems (green) are attached to the water reference (blue), the tubing from outside (orange) is for the injection of the contrast agent. After positioning in the glass tube filled with the media, the 5 imaging slices (gray) are acquired. In the fotos, the teflon tape (white) and the sample holder (white) are visible.

8.2.3 Plant-specific adjustments of the MRI-method

The majority of clinical protocols used in DCE-imaging are based on gradient echo sequences, which enable a fast acquisition of the datasets and a shortening the measurement time, therefore maximizing patient comfort. The FLASH-sequence [Haa85] is preferred in clinical imaging, where the tissues are magnetically rather homogeneous, since the sequence is based on small flip angles and thus enables an accelerated imaging compared to the SE-protocol. Plant tissue, on the contrary, is magnetically very heterogeneous, in particular due to air inclusions, compared to animal or human tissue [Bor12; Köc01]. In the presence of rather short T_2^* times, the spin echo sequence is the method of choice for application in plants. By adaption of Tofts' approach, the measurement times for the T_1-mapping via the rather slow spin echo sequence could be significantly reduced for measurement in plants.

8.2.4 Effect of the contrast agent on T_1

Gd-DTPA, the contrast agent used in the experiments, is based on Gadolinium. The molecules diameter is approximately 8.8 Å, its molecular weight is 938 amu [Oto12]. These features enable a comparison of its transport characteristics with the sucrose molecule (molecular diameter 9 Å [Ram85], molecular weight 342 g/mol [Dat18]). Gadolin-

ium is strongly paramagnetic, since it contains seven unpaired electrons. Thus, the relaxation process is accelerated in the presence of the contrast agent compared to the natural relaxation process. The shortened relaxation parameter $T_{1,1}$ itself is dependent on the initial value $T_{1,0}$ and the concentration c of the contrast agent within the sample [Tof91].

$$\frac{1}{T_{1,1}} = \frac{1}{T_{1,0}} + c \cdot R_{CA} \tag{8.1}$$

The relaxivity R_{CA} of the contrast agent at 17.6 T was determined by measuring T_1 of different dilutions (in the range of 50 μmol/l to 10 mmol/l) of the contrast agent in distilled water. For the measurements, an Inversion Recovery Spin-Echo-Sequence with varying Inversion Times (TI) was used, the slope of a linear fit through the measured values of R_1=1/T_1 plotted over the concentration c enabled the determination of the relaxivity R_{CA} at the given field strength.

8.2.5 Probing experiment vs theory by Dynamic Contrast-Enhanced MRI

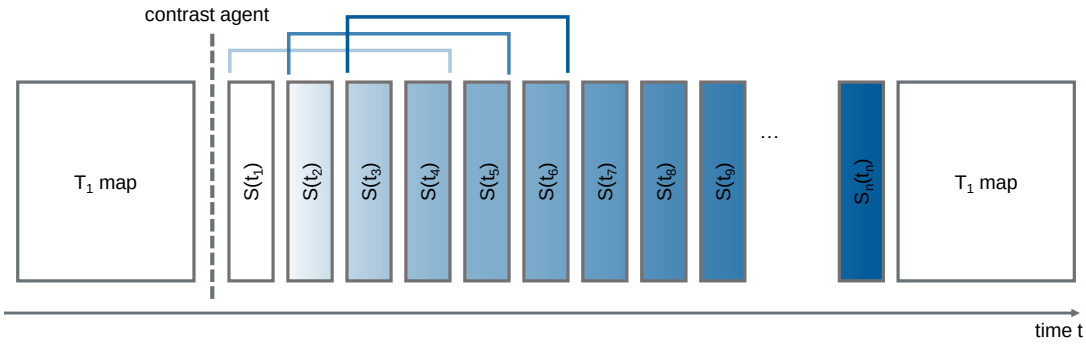

Figure 8.2: Scheme of the BACARDI protocol: After the first, time-consuming T_1-map of the sample, the contrast agent was added. The consecutive, T_1-weighted acquisitions ($S(t_i)$) were started immediately. As a reference, a second, time-consuming T_1-map was acquired at the end of the experiment.

In Fig. 8.2, the scheme of the BACARDI method is shown. At first, a reference T_1-map was acquired, based on a slice-selective Spin-Echo (SE) Sequence with various repetition times (TR). The contrast agent was added to the sample after the measurement of the time-consuming full T_1-parameter map (measurement time approximately 2 h 13 min), and adjustments for the consecutive measurements were performed (coil tuning, shimming). The following 383 (barley stem) or 549 (rapeseed silique) acquisitions for monitoring the translocation dynamics were started immediately. These

T_1-weighted images were acquired with a fixed repetition time of TR=700 ms and in a timespan significantly reduced to the initial T_1-map. The increased temporal resolution of 6 min was sufficient for the following dynamic analysis.
The concentration of the added contrast agent was 50 mmol/l, thus in the water reservoir of the plants, an approximative concentration of 20 mmol/l was present. In order to verify the correct T_1-calculations, a second T_1-map was acquired at the end of the canola experiment using the same sequence and parameters as the initial T1-map, see scheme in Fig. 8.2. For an optimization in SNR, the T_1-weighted images were acquired with a number of averages NA=4, also enabling a dynamic sliding-window analysis of the consecutive T_1-weighted images. For the estimation of vertical transport velocities, all experiments were set up with five parallel slices (thickness 0.5 mm (rapeseed), 2.0 mm (barley stem), distance between slices 2.0 mm). The detailed measurement parameters are shown in Tab. 8.1. For the first T_1-weighted images, the assumption was

T_1-map		T_1-weighted	
TR	varying	TR	700 ms
TE	4.2	TE	4.2
NA	2	NA	4
FoV	barley: 11 x 11 mm^2	FoV	barley: 11 x 11 mm^2
	rapeseed: 8 x 8 mm^2		rapeseed: 8 x 8 mm^2
Matrix	128 x 128	Matrix	128 x 128
Slices	5	Slices	5
N_{Exp}	10	N_{Exp}	barley: 383
			rapeseed: 549
T_{Acq}	2 h 13 min	T_{Acq}	5 min 58 s

Table 8.1: Measurement parameters for the BACARDI measurements. Abbreviations: **TR**: Repetition Time, **TE**: Echo Time, **NA**: Number of Averages, **FoV**: Field of View, $\mathbf{N}_{Exp}$: Number of individual experiments, $\mathbf{T}_{Acq}$: Acquisition duration of a single image.

made, that the contrast agent's concentration in the plant tissue remains zero, and, as in Tofts' approach, that signal changes were not caused by instrumental influences. By using an in-house written MATLAB (The MathWorks Inc, Natick, MA, USA) algorithm using a least-squares fit, the initial (time consuming) T_1-map was calculated. Based on the initial T_1-map and the T_1-weighted images, the dynamic T1-maps of the plant tissue were calculated. The calculation of the CA's concentration maps was enabled by the dynamically changing T1-parameter in the plant tissue. The transport velocities of the tracer could be calculated for vertical (xylem/phloem) and horizontal (out of the transporting strand) direction by determining the Gd-DTPA concentration value in the plant tissues. In most cases, a reduced T_1 parameter leads to a higher

NMR-signal S in a T_1-weighted image. This dependency can be described for every voxel by:

$$S(TR, T_1) = M_0 \cdot (1 - e^{-TR/T_1}) \tag{8.2}$$

Eq. 8.2 has to be distinguished before (S_0) and after (S_1) injection of the contrast agent:

$$S_0 \propto M_{0,0} \cdot (1 - e^{-TR/T_{1,0}}) \tag{8.3}$$

$$S_0 \propto M_{0,1} \cdot (1 - e^{-TR/T_{1,1}}) \tag{8.4}$$

which leads to a ratio x of both signals:

$$x = \frac{S_0}{S_1} = \frac{1 - e^{-TR/T_{1,0}}}{1 - e^{-TR/T_{1,1}}} \tag{8.5}$$

The equation can now be solved for the new dynamic $T_{1,1}$:

$$T_{1,1}(TR, T_{1,0}, x) = -TR \left[ln \left(1 - x \left(1 - e^{-TR/T1,0} \right) \right) \right]^{-1} \tag{8.6}$$

Within the DCE-image, the parameter $T_{1,1}$ can be calculated for every voxel. It is dependent on the measurement parameter TR, the initial value $T_{1,0}$ and the ratio of the signal intensities x in each voxel. The concentration c of the contrast agent can be calculated with the now known parameter $T_{1,0}$, based on Eq. 8.1:

$$c = \frac{T_{1,0} - T_{1,1}}{T_{1,0} \cdot T_{1,1}} \cdot \frac{1}{R_{Gd-DTPA}} \tag{8.7}$$

These equations can be written in this simple form, unlike in other studies utilizing DCE-MRI, since a standard SE sequence is used; i.e., approximations for small flip angles are not necessary.
Since the ratio x (Eq. 8.5) is dependent on the measured signal amplitudes at different time points, influences of noise or movement can affect the calculation of a correct T_1-value, this effect is common in DCE-experiments. The ratio x in a previously 'empty' voxel can be significantly changed by a growing or moving part of the plant, thus the T_1-values calculated in these areas will be too high to be physically correct and must therefore be ignored.

8.3 Results

In this chapter, Tofts' method was modified for application in living plants to: (1) evaluate the dynamic features of the vascular system and to (2) determine local con-

centrations of the contrast agent for (3) calculation of translocation velocities.

8.3.1 Estimation of the relaxivity of the contrast agent

The relaxivity of the contrast agent Gd-DTPA at 17.6 T was estimated from a concentration series as described above:

$$R_{1,Gd-DTPA} = (3.7831 \pm 0.0085)\frac{1}{mmol \cdot s}$$

In order to evaluate this result, this value can be compared to relaxivities determined at different field strengths: Sasaki et al. [Sas05] found a value of 4.79 (1/mmol·s) at a field strength of 1.5 T and 4.50 (1/mmol·s) at a field strength of 3 T in water phantoms containing dilutions of Gd-DTPA.
The value obtained at 17.6 T is located within a reasonable range and will be used for further calculations within this experiment. Since the relaxivity was measured in a water phantom, it can differ in plant tissue. Should this fact cause any possible errors, it will only concern the quantified concentrations and not the transport velocities.

8.3.2 Detection of the area of active vascular tissue

The contrast agent was taken up by the plant over the course of the experiment, which lead to an increase of signal in the tissue containing the CA, as exemplified for the barley stems in Fig. 8.3. These dynamic T_1-weighted images allowed, in combination with the initially T_1-map, acquired with a SE sequence with various TR values, the calculation of the DCE-T_1-maps, as shown in Fig. 8.4.
For a better overview, T_1-values that clearly exceed the reasonable range (e.g., caused by noise or movement of the plant) are set to zero. The presence of the contrast agent can be shown in detail in Fig. 8.5, which is a difference image between two images (i) acquired directly after application of the CA and (ii) at the end of the experiment. In this image, the reference sample is not visible since no change in signal was induced. In the stem tissue, a high intensity in the difference image represents a high change of signal over the course of the experiment and thus a high uptake of the contrast agent. In the vascular bundles, the high concentration of the CA leads to a reduction of signal and thus, they appear dark in the difference image.
The experiment with the canola plant is shown in Fig. 8.6, selected T_1-weighted images depict the uptake of the contrast agent over time. Based on these images and with the initial T_1-map as a reference, the calculation of the dynamic T_1-maps (Fig. 8.7) and

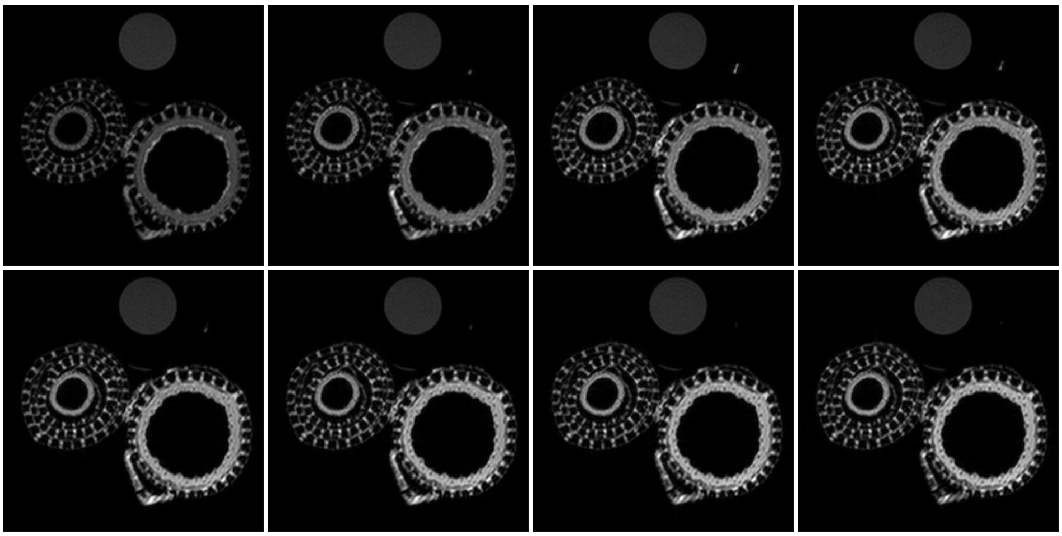

Figure 8.3: Magnitude images of the barley stems (bottom) over time and the reference sample (top). The experiment starts in the top row on the left and ends in the bottom row on the right. The allocation of the contrast agent in the plant tissue leads to a change of the acquired NMR signal, based on these magnitude images and the initial T_1-map, the dynamic T_1-maps can be calculated.

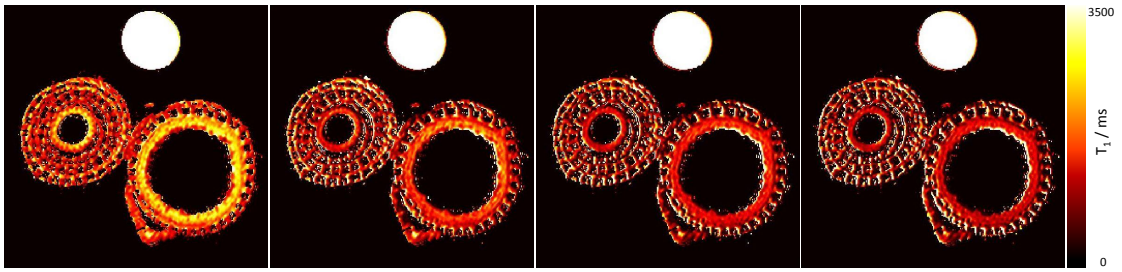

Figure 8.4: Dynamic DCE-T_1-maps of the barley stems for selected points of time. The contrast agent is taken up by the plant and is allocated in the plant tissue. The relaxation parameter T_1 decreases due to the presence of the CA.

the associated concentration maps (Fig. 8.11) was performed.

During the experiment, the seeds were growing which by itself leads to a change in signal behaviour in the voxels monitored, thus the concentration maps are valid only for the pod tissues but not for the seeds. It was not possible to distinguish this change from the effects of the CA. In this area, the voxels must be ignored since the apparent increase in signal is not caused by the contrast agent.

In the T_1-maps, the active vascular tissue strands can easily be identified within the surrounding plant tissue as their T_1 values decrease during the experiment.

The uptake of the contrast agent in the plant tissue leads to a decrease of the T_1-

Figure 8.5: **Left**: Presence of the contrast agent in the barley stems. The difference of two T_1-weighted images, one from the beginning of the experiment and one from the end reveal the areas of the plant tissue, where the contrast agent accumulated. **Right**: light microscopy images; slice of barley stem (bottom) and staining of lignine with phloroglycine (top). The vascular bundles are visible in the stem tissue.

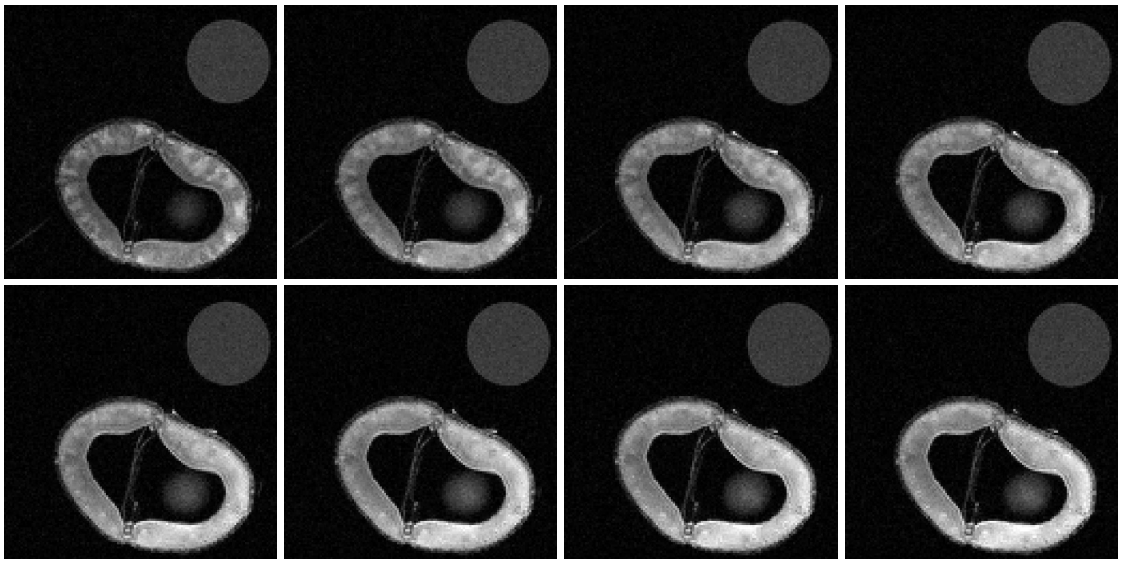

Figure 8.6: Magnitude images of the rapeseed silique (bottom) over time and the reference sample (top). The experiment starts in the top row on the left and ends in the bottom row on the right. The allocation of the contrast agent is visible.

parameter, as can be shown for two selected ROIs within the rapeseed silique, see Fig. 8.8.

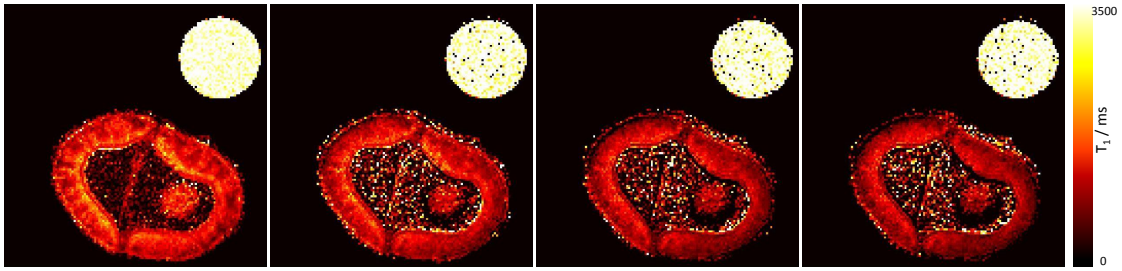

Figure 8.7: Dynamic DCE-T_1-maps of the Rapeseed silique for selected points of time. The contrast agent is taken up by the plant and is allocated in the plant tissue. The relaxation parameter T_1 decreases due to the presence of the CA. Regions of growth have been set to zero.

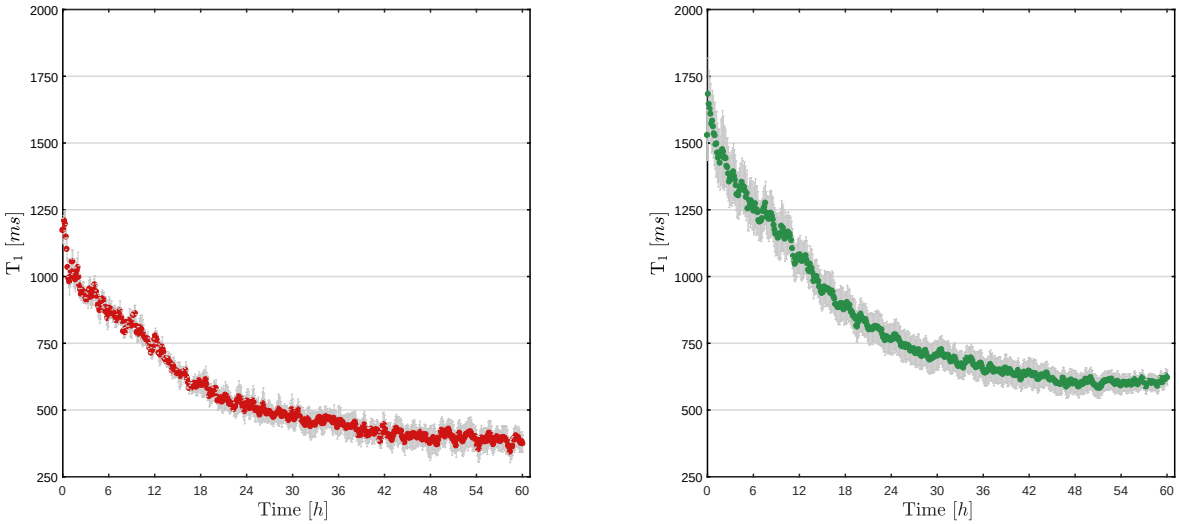

Figure 8.8: Dynamic T_1-values in the vascular strand (left) and the surrounding tissue (right). The uptake of the contrast agent leads to a significant decrease of T_1 in both tissues.

Upon administration of the contrast medium the course of a vessel can be observed, and a closer look (in Fig. 8.7) at the T_1-value of a selected transporting strand and its surrounding tissue shows a clear decrease in the relaxation parameter in both ROIs over time, shown in Fig. 8.9. The spin-lattice relaxation time T_1 falls within the time of measurement to $(28.4 \pm 4.4)\,\%$ of its initial value.
In Fig. 8.10, the T_1 course of the water sample is shown. Within the error bars, the values remain constant over the duration of the measurement. This underlines that the dynamic T_1 estimation provides reliable values over time and is not affected by external influences due to signal instabilities of the MR scanner.

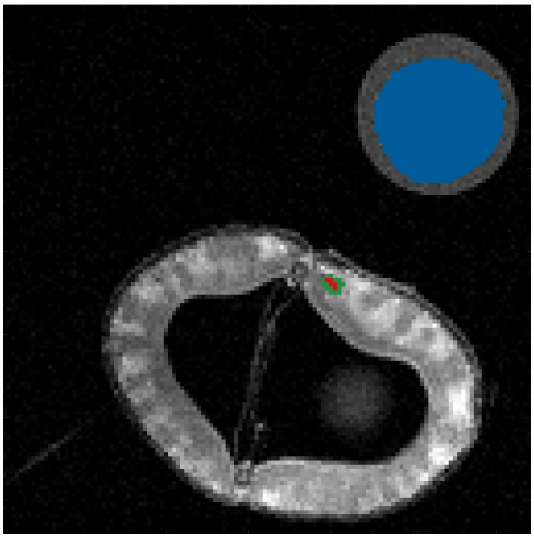

Figure 8.9: Location of ROIs within the rapeseed silique: blue: water sample, red:: vascular strand, green:: silique-tissue.

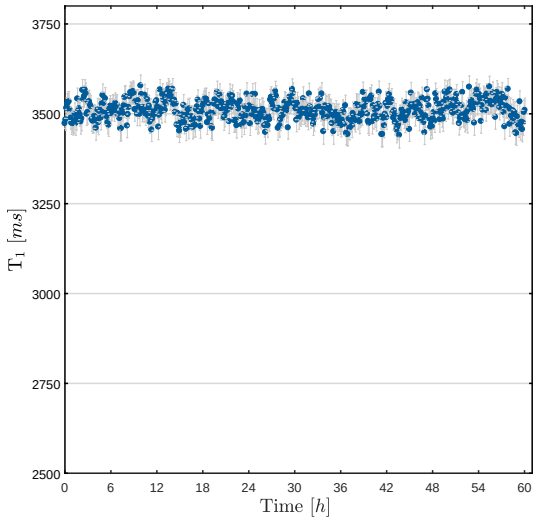

Figure 8.10: Dynamic T_1 values of the water sample (reference) - Within the error bars, the values are consistent and underline the assumption, that no external influences affect the dynamic T_1 estimation.

8.3.3 Evaluation of concentration range of the contrast agent in plant tissues

On basis of the dynamic T_1-maps, the determination of the time-dependent contrast agent concentrations is performed. Compared to the surrounding tissue, the transporting strand exhibits a higher concentration of the CA than the surroundting tissue, see Fig. 8.11 and 8.12. Concentrations of up to (0.55 ± 0.12) mmol/l were calculated, a minimal concentration of 0.01 mmol/l was found in the transporting strands at the

beginning of the experiment.

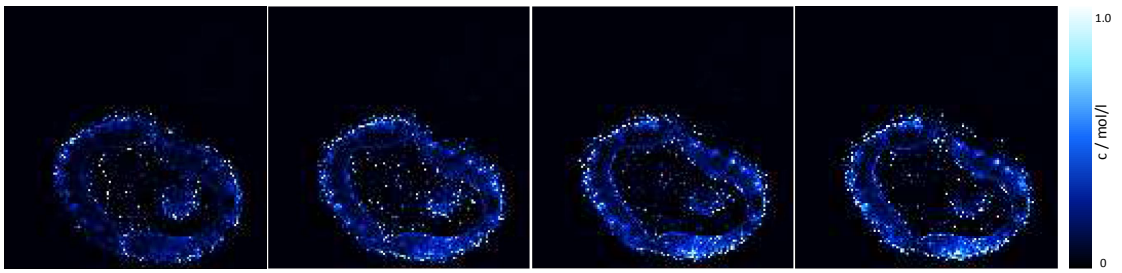

Figure 8.11: Dynamic DCE-concentration-maps of the rapeseed silique for selected points of time. The contrast agent is taken up by the plant and is allocated in the plant tissue. The vascular bundles contain the highest concentration of contrast agent.

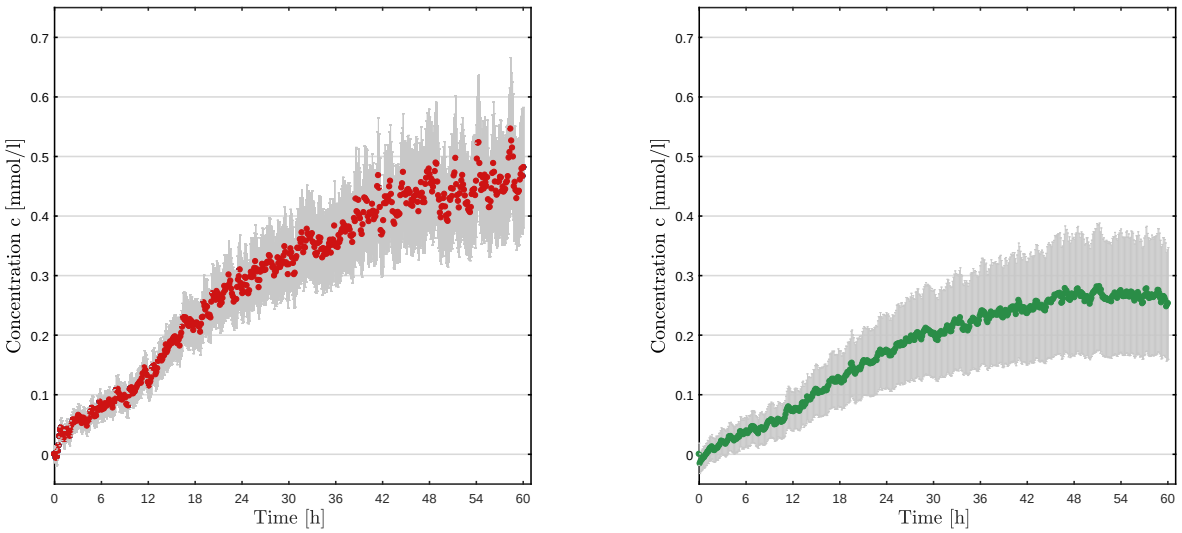

Figure 8.12: Concentration of CA in the vascular strand (left) and the surrounding tissue (right). The contrast agent allocates in both tissues, while the concentration in the vascular strand is significantly higher than in the surrounding tissue.

The quantification of the contrast agent's concentration in pod tissue around the vascular tissue strand showed the following behaviour: The T_1 parameter decreased with delivery of the contrast agent from the vascular tissue into the surrounding tissue during the experiment. Throughout this process, the concentration of the CA increased up to (0.282 ± 0.098) mmol/l. In the liquid media, the concentration of Gd-DTPA was adjusted to 20 mmol/l, in the plant's vascular strands and tissue the concentrations are significantly lower. As can be seen in Fig. 8.12, a saturation effect in the plant tissue can be observed. All transporting strands visible in the image are behaving in a comparative manner, as can be seen on basis of the calculated maps of CA concentration

in the pod. All strands in the pod investigated are functioning, since the concentration values reached are comparable. After approximately 2.5 hours after insertion of the CA, the first distinct identification of the active strands can be performed.

8.3.4 Determination of transport velocities using BACARDI

The BACARDI method can now be applied for the estimation of vertical and horizontal tracer velocities inside the barley stem and canola silique. By comparing the points of time when the T_1-parameters in the same transport fibre in different slices start to decrease, the estimation of the transport velocity in the vertical direction can be performed. The method is exemplified in canola:
It is necessary for a correct estimation to follow a vascular tissue strand through the various slices. The assumption, that the vascular tissue strands are not crossed, was made. Within each slice, the point of time of the contrast agent's first appearance in the vascular strand was determined. By calculating the difference in the delay time t_{off} between the upper and lower slices the time required for the contrast medium to pass through the slices can be estimated. The slice distance is known from the measurement parameters.

Barley stem

Three transporting strands could be identified in different slices, this enabled the calculation of the tracer's transport velocity in the barley stem. Through the arithmetic mean and standard error calculations, the vertical allocation velocity $v_{vertical}$ was obtained:

$$v_{vertical} \approx (24.3 \pm 6.1)\frac{mm}{h}$$

Canola silique

The estimation for the canola silique was performed analogously. Alongside the replum of the silique (Fig. 8.11), well pronounced vascular strands are present. In the MRI dataset, it was possible to clearly identify two vascular tissue strands, as shown in detail in Fig. 8.9.
In the rapeseed silique, the vertical transport velocity $v_{vertical}$ was determined as

$$v_{vertical} \approx (7.48 \pm 0.59)\frac{mm}{h}$$

This values does not match the water flow velocity, it is only valid for the translocation of the tracer itself. The molecular weights of water and Gd-DTPA differ significantly.

For studies on the translocation of molecules of similar (chemical/physical) properties inside of plant tissues, this tracer can potentially be used.
A leakage of the contrast agent from the vascular tissue strands into the surrounding tissue was observed. In this region, the contrast agent moves a certain distance perpendicular to the main (vertical) strand. Thus, the speed determined is therefore an estimate of the horizontal velocity of the contrast agent. For determination of this horizontal velocity, different vascular tissue regions of interest (ROIs) with a thickness of one voxel, thus being rings around the strand, were examined. The distance Δs travelled by the contrast medium was $\Delta s \approx 63\,\mu$m, thus identical to the isotropic in-plane resolution.
The determination of the time required for the contrast agent to penetrate from the vascular tissue into the pod tissue was performed as follows: looking at the graph of concentrations, it appears that some time passes until the concentration increases from 0 mmol/l to a value cc $>$ 0 mmol/l in the pod tissue. The time required for the contrast agent to penetrate from the vascular tissue into the surrounding tissue is thus the difference between the time in which the increase is initiated in the vascular tissue, and the time at which the increase starts in the surrounding pod tissue.
The translocation velocity $v_{horizontal}$ from the vascular tissue into the plant tissue can be estimated:

$$v_{horizontal} \approx \frac{\Delta s}{t_{siliquetissue,c_c} - t_{transportingstrand,c_c}} \tag{8.8}$$

An estimate of the horizontal translocation velocity (followed by arithmetic mean and standard error calculations) is obtained by analysing the vascular tissue strands and their surrounding tissue

$$v_{horizontal} \approx (105.0 \pm 9.5)\frac{\mu m}{h}$$

In the next step, a classification of the horizontal transport as a driven or passive transport mechanism is performed. To solve this question, a comparison with free diffusion can be used. The estimation of the diffusion coefficient D is enabled by an evaluation of the level of mobility of molecules. In free diffusion, Eq. 8.9 is applied, based on [Tof91].

$$\Delta s^2 = 2dDt \leftrightarrow D = \frac{(\Delta s)^2}{2dt} \tag{8.9}$$

Δs^2 is the mean square displacement of a particle in time t, and d is the dimensionality. Gussoni et al. [Gus01] measured the diffusion coefficient of Gd-DTPA in a morning glory stem as

$$D_{Gd-DTPA} = 1.0 \cdot 10^{-11}\frac{m^2}{s}$$

Hereinafter, this will serve as a reference value for the classification of horizontal transportation properties.
The transportation out of a vascular tissue strand can be regarded as a two-dimensional problem (d = 2). The average displacement Δs and the time interval t are defined as the radius of the directly surrounding tissue and time difference, respectively. Including the standard error, the time interval for the CA concentration to reach the value cc in the vascular bundle and its surrounding tissue is calculated as t = (2178 ± 198) s. With the assumption, that the transport observed is completely diffusion-driven, the diffusion coefficient can be calculated from Eq. 8.9, thus the diffusion coefficient $D_{horizontal}$ is obtained:

$$D_{horizontal} = (4.56 \pm 0.14) \cdot 10^{-13} \frac{m^2}{s}$$

In comparison to the value $D_{Gd-DTPA}$, this coefficient is two orders of magnitude smaller. Therefore, the assumption that the contrast agent is directionally transported from the vascular tissue into the pod tissue is questionable. The transport occurs to be based solely on diffusion, which must be significantly impeded, for example, by cell membranes.

8.4 Discussion

In the past, various tracers (usually isotope-labelled and fluorescent probes) were used successfully to track water and metabolite allocation in plants [Zam04; Hub15; Sug16]. For the application in living tissues, the tracer should be biologically inert, non-toxic and non-invasively detectable.

8.4.1 Advantages and restrictions of BACARDI

The method BACARDI is based on the application of a clinically used contrast agent. Thus, the minimization of interference with the plant's functionality allows for noninvasive determination of transport characteristics.
Additional microscopic examination of tissues, as it is common by application of fluorescent tracers and dye in experimental botany [Bor02; Sta05], is not required for the localization of the Gd-tracer in the vascular system. Gd-DTPA is a non-hazardous substance that can be applied for long lasting experiments, which is an advantageous feature compared to radioactive labelling, which is required for PET experiments [Hub15]. Regarding the infrastructure, the performance of PET experiments is certainly more complex (cyclotron, radiochemistry laboratory, and PET camera) than performing an MRI experiment. Via MRI, the paramagnetic component can be non-invasively traced

in living (plant) organism, similar to medical diagnostics. BACARDI represents an enabling technology, first because it's capability for survey of the fluxes in a low range of velocity (µm/h), which is not accessible for standard MRI DCE-based procedures; second, because the method provides a means to determine the local concentration of the tracer inside of tissue.
Due to the peculiarity of plant tissue, structure and metabolism, and in contrast to clinical measurements that are usually limited to a duration of one hour, the duration of the entire plant experiment was planned on a time scale of days. Since in Gd-DTPA, the Gd-ion is enclosed in a chelate complex, the paramagnetic effect of the Gd is still active, but the cell-damaging effect is suppressed. By Gd-DTPA, the metabolism of living systems is not affected [Gus01; Zha09], it could be the contrast agent of choice for various plant experiments in combination with BACARDI.

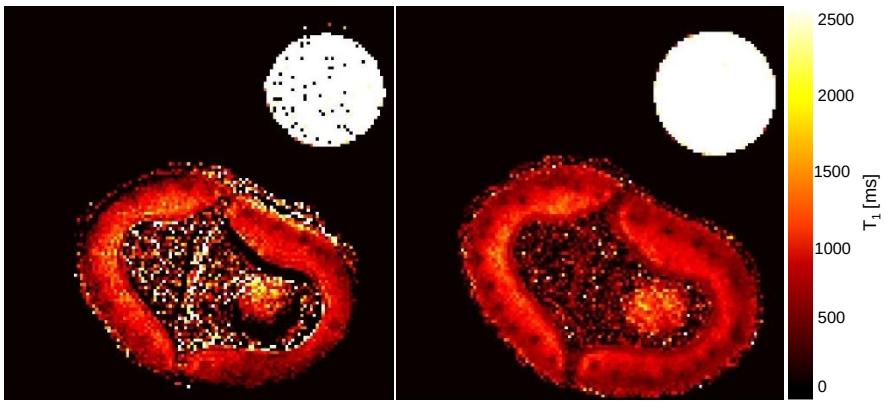

Figure 8.13: Dynamic DCE-T_1-map and reference T1-map of the rapeseed silique. The obtained T_1-values are comparable to the reference values, the dynamic method can only be applied for non-moving tissue.

For the adaption of Tofts' approach to plant imaging no approximations typically used in standard DCE-based Imaging techniques, e.g. flip angle approximations were required. Compared to the standard T_1-mapping sequence, high-resolution maps of the physical NMR parameter T_1 can be acquired dynamically and within a highly reduced time span. In Fig. 8.13, the final T_1-map recorded with BACARDI is shown side by side with the saturation recovery control measurement. The reliability of the T_1 values obtained with BACARDI is evident based on the good match of the T_1 values in both maps.In a direct comparison, the time-consuming T_1-map acquired with the various TR values provides information about the complete plant visible in the image and contains less noise. The relatively long measurement time for this map (2 h 13 min for canola and barley) underlines the advantage of the BACARDI method: by using BACARDI, a T_1-map is acquired within 6 min, which could increase the resolution in

time (by a factor of 22 in canola and barley) significantly while maintaining the spatial resolution of the image.
The dynamic T_1-maps enable the calculation of the concentration of the contrast agent, this information can then be used for identification and evaluation of the vascular bundles. With this method, it could be shown that the transport strands in silique are intact and functional. One of the major features of the BACARDI method is the direct and unambiguous identification of active transport tissue due to the fast and high-resolution T_1-maps of plant tissue. The application of the BACARDI method was exemplified on two different plants (barley and canola), and it was demonstrated how the tissues, which are instantly involved in solute allocation in the stem and fruit, can be identified using the new method (Fig. 8.11). The approach however is unable to determine T_1-times in moving or fast growing tissues, which is a disadvantage of DCE methods which rely on an initial T_1-map, compared to other time-consuming T_1-mapping methods.

8.4.2 Tracer-specific velocity and water flow

Most of the variety of reliable flow measurement methods provided by MRI directly measure the flow of water and rarely measure the velocity of molecules, which are allocated in the water flow. For example, a phase contrast encoding method used by Peuke et al [Peu01] and the utilization of a pulsed field gradient (PFG) method by Rokitta et al. [Rok99] enabled the measurement of the phloem velocity in the *Ricinus communis* plant, both provided comparable results at approximately 900 mm/h. The flow velocity can respond to the experimental condition, e.g., an increase from 36000 mm/h to 51000 mm/h in response to watering, as shown in cucumber plants by flow encoding method [VA84]; (ii) could vary in the same plant during development, e.g., in tomato from 1500 mm/h to 2100 mm/h [Win09]; (iii) could substantially differ between plant species, as for example the flow velocities reach up to 3600 mm/h in the stem of a small tree [Kar14], and be much lower in the stem of wheat and barley [Rol15b].
Via the vascular system, the differently sized tracers are translocated with distinct velocity (which could differ from that of water) and target different tissues in the plant [Bor02; Zam04; Niu11]. Compared to the measurements of water flow, measurements of their dynamics are a much more difficult task, thus, the size and types of tracers need careful consideration. It was shown by using fluorescent tracers, that small molecules such as the Lucifer Yellow LYCH (molecular mass Mr = 0.5 kDa) are highly permeable [Wan94], whereas small proteins (Mr = 15–30 kDa) are generally less mobile [Wil99]; in plant tissues, movement of large molecules (e.g., dextran Mr = 500 kDa)

is even more restricted [Arm04]. The molecular weight of Gd-DTPA (Mr=0.94 kDa) and sucrose (Mr = 0.342 kDa) are in the same range, the Gd-tracer may therefore be an appropriate tracer for the investigation of transport kinetics in plant tissue.
Hall et al. [Hal71] measured an average velocity of ^{14}C-labelled assimilates in castor bean plants as 820 mm/h, comparable to the velocity water flow [Peu01]. Measurements by the real-time radioisotope imaging system (RRIS) for mineral compounds in *Arabidopsis taliana* found translocation velocities of other compounds between 5 mm/h and 60 mm/h [Sug16].
Via DCE-MRI in T_1-weighted images, the transport velocity of Gd-DTPA in the stems of morning glory was measured to 0.7 mm/h [Gus01]. Compared to the values determined with BACARDI, this value seems rather slow; the translocation in the barley stem and the rapeseed silique was determined during the seed filling stage. At this time, the transport towards the seeds is expected to be highest in both plants.
In combination with the Gd-tracer, BACARDI is able to monitor flow velocity in range of μm/s in plants. The method is thus well appropriate for detection of tissues involved in molecular trafficking and for observation of vascular system activity in living plants. Nevertheless, features of Gd-tracers are still not fully understood [Erm10; Hal61; Bou82]. By integration of BACARDI with other state of the art technologies such as fluorescent tracers [Zam04], PET [Hub15] radioisotope-imaging [Sug16], or ^{13}C-MRI [Mel11], more confidence in the interpretation of experimental data could be achieved. In respect to metabolite allocation, these methods could provide additional information about the structure and composition of tissues.

8.4.3 Biological relevance of the BACARDI outcome

In both plants, the images provided by BACARDI allow for the detection of Gd-DTPA directly in the tissues: in the stem of barley (Fig. 8.5) and in the silique of oil rapeseed (Fig. 8.11). The allocation of CA can be monitored and related to distinct tissue structures with a high temporal resolution. Detailed investigation of the silique shows, for example, that the tracer is first detectable in the small regions of the silique walls that correspond to the main vascular vessels (xylem diameter 10-16 μm and phloem diameter of approximately 2-6 μm) and then detected in the surrounding parenchyma tissue (Fig. 8.8). The ability of BACARDI to visualize vascular tissues of the silique in a noninvasive way is indicated by the co-localization of the Gd-tracer with vascular bundles.
The experiments indicate, that the direction of Gd-flow is along the long axis of the stem (barley) and silique (canola), which is reasonable in both cases. First, the stem in

barley (peduncle region) is the main transportation route for supplying nutrients and water to the grooving spike, which is located at the top of stem. Second, the young rapeseed silique is the growing organ (sink organ). Its length increases approximately seven times regarding to its initial length towards maturity [Leb89; Wan16]. The seeds are connected to the pod sept (Fig. 2.1B), they are also localized along the longitudinal axis and involved in solute/water uptake. In the BACARDI experiment, the highest velocity of Gd-flow in the silique reached 7.48 mm/h, and it is registered along the elongation vector. The direction of flow and the high velocity, both measured with BACARDI, correspond well with the growth pattern of the silique (described above). In the tissue surrounding the vascular vessels (horizontal direction), Gd was also detected by BACARI, as demonstrated in canola silique. From an anatomical perspective, this observation could be explained by the influx of the Gd-tracer from the vascular tissue to the parenchyma. this influx could include the symplastic pathway (direct cytoplasm-to-cytoplasm) and the apoplastic pathway (passage through the cell membrane). Such a route for metabolite translocation (e.g. sucrose and small proteins) is in general expected to be very slow because the size of plasmodesmata, the activity of involved transporters, etc. are the limiting factors. The Gd-tracer used here (8.2 Å) and sucrose are distinct in structure and dynamic features. Nevertheless, the measured value of the horizontal transport velocity of Gd-DTPA in the canola silique ($v_{horizontal} \approx (8105.0 \pm 9.59)\,\mu$m/h) is comparable to the transport velocity of ^{13}C-labelled sucrose in the barley cariopsis (145 μm/h dorso-ventral, 72 μm/h lateral) [Mel11].The transport velocity of the Gd-complex is almost identical to the sugar molecule's, at least within the imaged area of tissues. This method could enable the the investigation of sucrose transport characteristics by utilization of Gd-DTPA.

The experiments indicate that the Gd enters the plant cell symplast and moves in conjunction with the flow of solutes. A similar observation was made using other non-invasive methods in the roots and stems of morning glory plants [Qui90] and in tomato [Zha09]. Compared to the connecting cell plasmodesmata, the diameter of the vascular tissue is several-fold larger. The tracer's restricted movement within the tissue's compartments, as was observed in the BACARDI experiments, is caused by this fact and the absence of transporters in the synthetic molecule of the tracer in plants. The BACARDI method is well applicable for evaluation of the transport-mechanisms in plants, but membrane permeability of Gd-DTPA as a tracer must be considered in experiments using living plants.

8.5 Conclusion

The presented BACARDI method provides the means for investigation of molecule/solute allocation in plants. The utilization of a T_1-mapping protocol in conjunction with a sliding-window analysis of the T_1-weighted images allowed to capture high-resolution T_1-maps of intact silique of *B. napus* and the stem of *H. vulgare* plants. In the plant objects, the active vascular tissue (vessels and surrounding cells) were identified. With BACARDI, the temporal resolution of the T_1-mapping has been improved to allow for the dynamic in vivo analysis of transport processes in the living plant. Concentrations of the contrast agent within the plant tissue could be estimated. These estimations further allowed for the determination of the tracer's translocation velocity, both in vertical (along the vascular tissue) and horizontal (out of the vascular strand into the plant tissue) direction.
Thus, this method is well applicable for evaluation of the transport-mechanisms (localization, dynamic, concentration measurements) in plants. In living plants, it could be a versatile instrument for various experimental designs, where paramagnetic features of Gd can be used as a label for molecules.

Chapter 9
Conclusion & Perspectives

I never expected this to happen in my lifetime and shall ask my family to put some champagne in the fridge.

Peter Higgs (about the discovery of the Higgs boson)

The noninvasive magnetic resonance imaging technique allows for the investigation of functional processes in the living plant. For this purpose during this work, different NMR imaging methods were further developed and applied.

Selective Imaging of a germinating canola seed
For the localisation of the intrusion of water into the germinating rape seed with the simultaneous depiction of the lipid-rich tissue via a 3D rendering, in Chap. 5 the technique of interleaved chemical selective acquisition of water and lipid was used in the germinating seed. The utilization of high-resolution MR images of germinated seeds enabled the localization of a predetermined water gap in the lipid-rich aleurone layer, which resides directly under the seed coat. The for a long time in biology prevalent discussion, whether such a gap exists or the seed soaks up the water from all sides, rather like a sponge, could hereby, at least for the rapeseed seed, be answered clearly. Furthermore, the segmentation and 3D visualization of the vascular tissue in the rapeseed seeds was enabled by the high-resolution datasets, a multiply branched structure preconstructed in the seed could be shown. The water is directed by the vascular tissue and thus awakens the seed gradually to life. This re-awakening could as well be tracked by means of invasive imaging via an oxygen sensor. In the re-awakened seeds, the lipid degradation starts, other than expected, not in the lipid-rich cotyledons but in the residual endosperm remaining from seed development and in the aleurone layer which previously protected the embryo. Within this layer, the degradation could be verified in the high-resolution MR datasets.

Visualisation of unsaturated fatty acid components

The method presented in Chap. 6 provides a further characteristic trait for phenotyping of seeds and lipid containing plants in general. The visualization of the compounds of fatty acids in plant seeds and fruits could be achieved by the distinct utilization of chemical shift-selective imaging techniques. Via the application of a CSI sequence the fatty acid compounds in an olive were localized in a 2D slice. In conjunction with an individually adjusted CHESS presaturation module [Haa85] the high-resolution 3D visualization of saturated and unsaturated fatty acid compounds in different seeds was achieved. The ratio maps calculated from these datasets allow to draw conclusions from the developmental stage or the type of seed. Furthermore, it could be shown that the storage condition of two soybean seeds with different storage time durations lead to no degradation of the fatty acid content.

Plant imaging with ultrashort echo times

Additional structural information from inside of dry seeds are now accessible via MRI. In this work the imaging of cereal seeds could be significantly improved by the application of the UTE sequence. The hitherto existing depictions of the lipid distribution, acquired with the spin echo sequence, were always sufficient for examinations of the lipid content, yet defects in the starchy endosperm or differences in the starch concentration within the seed remained constantly unseen with this technique. In a direct comparison of the datasets acquired with the previous imaging technique (spin echo) and with UTE imaging, the advantage of data acquisition with UTE could be shown. By investigating the potential seed compounds (starch, proteins, sugar) in pure form, the constituent parts contributing to the signal could be identified as bound water (residual moisture) and starch. The application of a bi-exponential fit on the datasets of the barley seed enabled the separate mapping of magnetization and of relaxation time of two components contributing to the NMR signal. The direct comparison with histological stainings verified the previous results, thus this technique can be used for the selective imaging of starch in dry seeds.

Dynamic determination of translocation velocities

Conclusions on the translocation characteristics in plants can be drawn by the technique proposed in Chap. 8. The associated translocation velocities can now, even in the range of several μm/h, be determined in the living plant. Based on calculated concentrations of an MR contrast agent, which was taken up by the plant, these translocation velocities were estimated both in longitudinal direction, thus along the vascular bundle,

and in horizontal direction, thus out of the bundle. The latter velocity is located below the contrast agent's velocity value of free diffusion. By adjusting a dynamic contrast-enhancing imaging technique (DCE-Imaging, [Tof91]) the acquisition duration of a T_1-map was significantly reduced. By means of these maps, local concentrations of the contrast agent in plant stems and the siliques of the rapeseed plant could be determined.

Outlook

Numerous questions in plant science can only be answered by non-invasive techniques such as MRI. For this reason, besides the experimental results achieved in this work, further NMR methods were tested and provided for the investigation of plants.

As an example, the study on the imaging of magnetic exchange processes are mentioned, which provided the groundwork for a possible transfer of CEST experiments (**C**hemical **E**xchange **S**aturation **T**ransfer) to the plant. The results are presented in the bachelor thesis of A. Jäger [Jä17], which was performed under my supervision, they find great interest under biologists.

The development of new technologies, which extend the possibilities for the investigation of living organisms, is of great importance. For this reason, I have contributed to the development of the currently unpublished method RACETE (**R**efocused **A**cquisition of **C**hemical **E**xchange **T**ransferred **E**xcitations [Jak17], [Reu17], [Gut18a]). By rephasing the transferred magnetization the utilization of properties which have not been available in chemical "'exchange"' experiments is enabled. With this method a positive contrast is generated, thus a reference experiment is not mandatory. Furthermore, the image phase, which in classical experiments contains no information about the exchanged protons, can be used for the distinct identification of multiple substances which have been excited simultaneously.

This recently at the Department of Experimental Physics V developed method can be used in particular for the identification of lipids and for the localization of sugars and amino acids, thus it can serve the enhancement and improvement of non-invasive analytical methods.

Zusammenfassung & Ausblick

Die nicht-invasive Bildgebungstechnik der Magnetresonanz ermöglicht es, funktionelle Prozesse in Pflanzen am lebenden Objekt zu untersuchen. Hierfür wurden im Rahmen dieser Arbeit verschiedene NMR-Bildgebungsmethoden weiterentwickelt und angewendet. Da Pflanzen ein magnetisch sehr inhomogenes Gewebe besitzen, bedingt durch Lufteinschlüsse und das Vorhandensein verschiedenster gelöster Stoffe im Pflanzengewebe, wurden daher hauptsächlich Spin-Echo-Methoden für die Bildgebung verwendet.

Selektive Bildgebung der Keimung eines Raps-Samens
Um das erste Eindringen des Wassers in den keimenden Raps-Samen bei gleichzeitiger Darstellung des lipid-reichen Gewebes mittels einer 3D-Visualisierung zu lokalisieren, wurde in Kapitel 5 die Technik der verschachtelten, chemisch selektiven Aufnahme von Wasser und Lipid im keimenden Samen verwendet. Durch Verwendung von hochausgelösten MR-Aufnahmen an gekeimten Samen konnte weiterhin in der lipid-reichen Aleuron-Schicht, die sich direkt unter der Samenschale befindet, ein gezielt angelegter Einlass für das Wasser verortet werden. Die in der Biologie lange Zeit verbreitete Diskussion, ob es einen solchen Einlass gibt oder der keimende Samen das Wasser eher wie ein Schwamm von allen Seiten aufsaugt, konnte hierdurch, zumindest für den Raps-Samen, eindeutig beantwortet werden. Weiterhin konnte durch die hoch-aufgelösten Aufnahmen das vaskuläre Gewebe in den Raps-Samen segmentiert und in 3D veranschaulicht werden, es zeigte sich eine mehrfach verzweigte Struktur, die bereits im Samen angelegt ist. Das Wasser folgt hierbei dem vaskulären Gewebe und erweckt hierdurch den Samen schrittweise zum Leben. Dieses Wieder-Erwachen konnte ebenfalls durch die invasive Bildgebung mittels eines Sauerstoff-Sensors nachverfolgt werden. Im nun erwachten Samen selbst beginnt der Lipid-Abbau, anders als zunächst angenommen, nicht in den lipid-haltigen Kotyledonen sondern im von der Samen-Entwicklung verbliebenden Endosperm und in der den Keimling vormals schützenden Aleuron-Schicht. In dieser konnte der Abbau an gekeimten Samen durch hochaufgelöste MR-Aufnahmen nachgewiesen werden.

Darstellung ungesättigter Fettsäure-Bestandteile

Die in Kapitel 6 vorgeschlagene Methode liefert ein weiteres Merkmal zur Phenotypisierung von Samen und lipidhaltigen Pflanzenbestandteilen im Allgemeinen. Die Darstellung der Bestandteile ungesättigter Fettsäuren in Pflanzensamen und -Früchten konnte durch gezielte Verwendung von chemisch selektiven Bildgebungstechniken erreicht werden. Durch die Anwendung einer CSI-Sequenz konnten die Fettsäurebestandteile in Oliven in einer 2D-Schicht lokalisiert werden. In Verbindung mit einem jeweils angepassten CHESS-Vorsättigungsmodul [Haa85] wurde die hochaufgelöste 3D-Darstellung von gesättigten und ungesättigten Fettsäurebestandteilen in unterschiedlichen Samen erreicht. Rückschlüsse über das Entwicklungsstadium sowie die Sorte der verwendeten Samen können aus den Verhältnis-Karten, die aus den jeweiligen Datensätzen berechnet wurden, gezogen werden. Dass in diesem Fall die Aufbewahrungsmethode zu keiner Degradation der Fettsäurezusammensetzung geführt hat, konnte weiterhin am Beispiel von zwei Sojasamen mit unterschiedlicher Lagerdauer gezeigt werden.

Pflanzenbildgebung mit ultrakurzen Echozeiten

Zusätzliche strukturelle Informationen aus dem Inneren trockener Samen sind nun mittels MRT zugänglich. In dieser Arbeit konnte durch die UTE-Sequenz die Bildgebung von Getreidesamen deutlich vorangebracht werden. Die bisherigen Darstellungen der Lipid-Verteilung, aufgenommen mit einer Spin-Echo Sequenz, waren zwar für die Betrachtung des Lipid-Gehalts stets ausreichend, Defekte im stärkehaltigen Endosperm oder Unterschiede in der Stärke-Konzentration innerhalb des Samen blieben mit dieser Technik jedoch stets verborgen. Im direkten Vergleich der mit der bisherigen Technik (Spin-Echo) und der UTE-Bildgebung aufgenommenen Datensätze konnte der Vorteil der Datenaufnahme mit UTE gezeigt werden. Durch die Untersuchung der möglichen Samenbestandteile (Stärke, Proteine, Zucker) in Reinform konnten die zum Signal beitragen Bestandteile als gebundenes Wasser (Restfeuchte) und Stärke identifiziert werden. Die Verwendung bi-exponentiellen Fits and die Messdaten ermöglichte es im Gersten-Samen, zwei zum Signal beitragende Komponenten in getrennten Karten bezüglich ihrer Magnetisierung und Relaxationszeit zu trennen. Der Vergleich mit histologischen Färbungen bestätigte die bisherigen Ergebnisse, somit kann diese Technik zur selektiven Darstellung von Stärke in trockenen Samen verwendet werden.

Dynamische Berechnung der Transportgeschwindigkeiten

Rückschlüsse auf das Transportverhalten in Pflanzen können durch die in Kapitel 8 vorgestellte Technik gezogen werden. Die zugehörigen Transportgeschwindigkeiten im lebenden Pflanzenobjekt können nun, selbst im Bereich von wenigen μm/h, bestimmt

werden. Diese wurden anhand von berechneten Konzentrationen eines von der Pflanze aufgenommenen MR-Kontrastmittels sowohl in longitudinaler Richtung, also entlang des Leitgewebebündels, als auch in horizontaler Richtung, also aus dem Leitbündel heraus, abgeschätzt werden; Letztere Geschwindigkeit liegt deutlich unter dem Wert der freien Diffusionsgeschwindigkeit des Kontrastmittels. Hierfür wurden durch Anpassung einer dynamischen Kontrast-erhöhenden Bildgebungstechnik (DCE-Imaging, [Tof91]) die Aufnahmedauer einer für die weiteren Berechnungen benötigen T_1-Karte deutlich reduziert. Mittels dieser Karten konnten die lokalen Konzentrationen des Kontrastmittels in Pflanzenstängeln und Schoten der Rapspflanze bestimmt werden.

Ausblick

Zahlreiche Fragen in der Pflanzenforschung können nur durch nicht-invasive Techniken wie MRT beantwortet werden. Deswegen wurden, neben den experimentellen Ergebnissen, die mittels dieser Arbeit erreicht wurden, auch weitere NMR Methoden für die Untersuchung von Pflanzen getestet und zur Verfügung gestellt.

Als Beispiel seien hier die Untersuchungen zur Bildgebung von magnetischen Austauschprozessen genannt, welche eine Vorarbeit zur möglichen Übertragung con CEST-Experimenten (**C**hemical **E**xchange **S**aturation **T**ransfer) auf das Modell Pflanze liefern. Die Ergebnisse sind in der Bachelor-Arbeit von A. Jäger [Jä17], an deren Durchführung ich als Betreuer maßgeblich beteiligt war, dargestellt und finden großes Interesse bei Biologen.

Von besonderer Wichtigkeit sind auch die Entwicklungen neuer Technologien, die die Möglichkeiten zur Untersuchung von lebenden Organismen erweitern können. Deswegen habe ich zu der Entwicklung der bislang unveröffentlichten Methode RACETE (**R**efocused **A**cquisition of **C**hemical **E**xchange **T**ransferred **E**xcitations [Jak17], [Reu17], [Gut18a]) beigetragen. Durch das Rephasieren der transferierten Magnetisierung können Eigenschaften, die bislang in chemischen "'Austausch"'-Experimenten nicht zur Verfügung stehen, ausgenutzt werden. Mit dieser Methode wird ein positiver Kontrast erzeugt, sie ist deshalb nicht zwingend auf ein Referenz-Experiment angewiesen. Weiterhin kann die Bildphase, welche in klassichen CEST-Experimenten keine Information über die ausgetauschten Protonen enthält, zur eindeutigen Identifizierung mehrerer parallel angeregter Substanzen verwendet werden.

Diese erst vor Kurzem am Lehrstuhl Experimentelle Physik V entwickelte Methode kann im Speziellen für die Identifizierung von Lipiden und für die Lokalisierung von Zucker und Aminosäuren genutzt werden und damit der Erweiterung und Verbesserung nicht-invasiver Analysemethoden dienen.

Appendix

Chapter 10
Appendix

10.1 Supervised Projects

During the work of this PhD-thesis, several projects have been supervised by me. In this section, the projects and their results are presented.

Sebastian Hammer: Kontrastmittelgestützte T_1-Messungen zur Untersuchung des Nährstofftransportsystems von Pflanzen

Sebastian Hammer performed the research for his "Zulassungsarbeit für die Staatsexamensprüfung" [Ham15] at the Department of Experimental Physics V at the University of Würzburg under my supervision. Some results of his work are presented in Chap. 8. The focus was set on the development of the BACARDI method and its first application in plants.

As a first step, the relaxivities of two contrast agents, Gd-DTPA and $GdCl_3$, were determined and first applications of both contrast agents on plants were tested. As research objects the stems of rose plants and the fruits of the rapeseed plant were used. Both plants showed a distinct uptake of the contrast agents, for reasons of toxicity and handling, the contrast agent used for clinical imaging, Gd-DTPA, was chosen for the following experiments.

The initial idea of acquiring a time-consuming T_1map before adding the contrast agent to the plant and then using rapidly acquired T_1-weighted images for the calculation of T_1-maps proved to be feasible in plant tissue. Sebastian Hammer developed an algorithm for the data analysis and created the name of the method: BACARDI.

After the setup of the experimental design, the BACARDI scheme was tested on rapeseed siliques and the translocation velocities were determined, both in longitudinal and in horizontal direction. In order to understand the obtained results, a comparison with the free diffusion of the CA molecule indicated a driven translocation in longitudinal and a hindered translocation in horizontal direction.

Based on the results created in this research project, I applied the BACARDI method successfully on barley stems, as shown in Chap. 8.

Andreas Jäger: Magnetresonanz-Bildgebung von chemischen Austauschprozessen

During his research for his Bachelor Thesis [Jä17], Andreas Jäger was supervised by Fabian T. Gutjahr and me. The aim of this work was the measurement of chemical exchange processes on Iopamidol and glucose molecules with the CEST (**C**hemical **E**xchange **S**aturation **T**ransfer) method.
Andreas Jäger built the phantoms required for these measurements and applied data analysis algorithms. For the evaluation of the CEST effect in Iopamidol, z-spectra of various dillutions of Iopamidol were acquired at three magnetic field strengths: 7.0 T, 11.7 T, and 17.5 T. Furthermore, the tranverse relaxation rate, R_2, of both Iopamidol and glucose dillutions was determined.

10.2 Measurement Parameters

In this appendix, the measurement parameters of the NMR experiments performed in this work are presented.

10.2.1 FAC-selective measurements

Soybean[1] (sat.)	Soybean[1] (unsat.)	**Parameter**	Rapeseed (sat.)	Rapeseed (unsat.)
875 ms	875 ms	**TR**	685 ms	685 ms
6 ms	6 ms	**TE**	4.5 ms	4.5 ms
18 x 8 x 8	18 x 8 x 8	**FoV/mm^3**	8 x 4 x 4	8 x 4 x 4
360 x 160 x 160	180 x 80 x 80	**Matrix**	192 x 96 x 96	192 x 96 x 96
2	8	**NA**	4	8
12 h 26 min	12 h 26 min	$\mathbf{T}_{Acq}$	7 h 1 min	14 h 2 min
2670 Hz	187 Hz	$\mathbf{\Delta}\omega_{SolvSupp}$	2670 Hz	-280 Hz
2.0 ms	1.5 ms	$t_{pulseSolvSupp}$	2.0 ms	1.4 ms
76.0 ms	74.0 ms	$\tau_{SolvSupp}$	76.0 ms	73.6 ms
110°	104°	$\alpha_{SolvSupp}$	105°	108°

Table 10.1: Measurement parameters for FAC-selective measurements. Abbreviations: **TR**: Repetition Time, **TE**: Echo Time, **FoV**: Field of View, **NA**: Number of Averages, $\mathbf{T}_{Acq}$: Total duration of the experiment, $\mathbf{t}_{pulseSolvSupp}$: duration of solvent suppression RF pulses, $\Delta\omega_{SolvSupp}$: offresonance frequency of solvent suppression RF pulses, $\tau_{SolvSupp}$: duration of solvent suppression RF pulses, $\alpha_{SolvSupp}$: flip angle of solvent suppression RF pulses.

[1]Soybeans of different developmental stage (same storage duration).

Nuts (sat.)	Nuts (unsat.)	**Parameter**	Soybean[2] (sat.)	Soybean[2] (unsat.)
685 ms	685 ms	**TR**	600 ms	600 ms
4.49 ms	4.49 ms	**TE**	12.75 ms	12.75 ms
8 x 4 x 4	8 x 4 x 4	**FoV/mm^3**	7.5 x 7.5 x 7.5	7.5 x 7.5 x 7.5
192 x 96 x 96	192 x 96 x 96	**Matrix**	125 x 125 x125	125 x 125 x125
4	8	**NA**	4	8
7 h 1 min	14 h 2 min	$\mathbf{T}_{Acq}$	10 h 25 min	20 h 50 min
2670 Hz	-502 Hz	$\mathbf{\Delta}\omega_{SolvSupp}$	2000 Hz	-1550 Hz
2.0 ms	1.2 ms	$t_{pulseSolvSupp}$		
		$BW_{SolvSupp}$	3000 Hz	3000 Hz
76.0 ms	72.8 ms	$\tau_{SolvSupp}$	217.05 ms	101.35 ms
105°	107°	$\alpha_{SolvSupp}$	95°	95°

Table 10.2: Measurement parameters for FAC-selective measurements. Abbreviations: **TR**: Repetition Time, **TE**: Echo Time, **FoV**: Field of View, **NA**: Number of Averages, $\mathbf{T}_{Acq}$: Total duration of the experiment, $\mathbf{t}_{pulseSolvSupp}$: duration of solvent suppression RF pulses, $\mathbf{BW}_{SolvSupp}$: bandwidth of solvent suppression RF pulses, $\Delta\omega_{SolvSupp}$: offresonance frequency of solvent suppression RF pulses, $\tau_{SolvSupp}$: duration of solvent suppression module, $\alpha_{SolvSupp}$: flip angle of solvent suppression RF pulses.

[2]Soybeans stored for 1 and for 36 years (same developmental stage).

10.2.2 UTE and MSME measurements

Parameter	Barley seed	Barley seed	Wheat seed	Wheat seed
Sequence	Spin Echo	UTE	Spin Echo	UTE
TR	750 ms	50 ms	500 ms	100 ms
TE	7.3 ms	0 μs	4.3 ms	10 μs
FoV / mm^3	13 x 6.5 x 6.5	13 x 6.5 x 6.5	10 x 5 x 5	15 x 5 x 5
Matrix	200 x 100 x 100	200 x 100 x 100	96 x 48 x 48	150 x 50 x 50
NA	4	4	6	6
T$_{Acq}$	8 h 20 min	3 h 1 min	3 h 50 min	19 h 35 min

Table 10.3: Measurement parameters for UTE & SE measurements of barley and wheat seeds. Abbreviations: **TR**: Repetition Time, **TE**: Echo Time, **FoV**: Field of View, **NA**: Number of Averages, **T**$_{Acq}$: Total duration of the experiment.

Parameter	Pea seed	Pea seed	"cavity seed"	"cavity seed"
Sequence	Spin Echo	UTE	Spin Echo	UTE
TR	1,000 ms	50 ms	500 ms	50 ms
TE	5.1 ms	10 μs	6.9 ms	10 μs
FoV / mm^3	12 x 12 x 12	12 x 12 x 12	20 x 10 x 10	20 x 10 x 10
Matrix	133 x 133 x 133	133 x 133 x 133	200 x 100 x 100	200 x 100 x 100
NA	2	12	4	8
T$_{Acq}$	9 h 49 min	10 h 27 min	5 h 33 min	5 h 19 min

Table 10.4: Measurement parameters for UTE & SE measurements of pea seed and the seed with the cavity. Abbreviations: see Tab. 10.3

Parameter	Venus flytrap	Venus flytrap	Proteins & Starch	Wood
Sequence	Spin Echo	UTE	UTE	UTE
TR	500 ms	50 ms	50 ms	50 ms
TE	9.3 ms	10 μs	0 μs	10 μs
FoV / mm^3	18 x 12 x 12	20 x 15 x 15	15 x 11.3 x 11.3	15 x 15 x 15
Matrix	150 x 100 x 100	167 x 125 x 125	80 x 60 x 60	133 x 133 x 133
NA	1	2	4	16
T$_{Acq}$	1 h 23 min	1 h 38 min	3 h 26 min	13 h 57 min

Table 10.5: Measurement parameters for UTE measurements of the venus flytrap, proteins and starch and dry wood. Abbreviations: see Tab. 10.3

10.3 Non-MRI Methods

For verification of the MRI experiments, further analyses were performed on the plant samples. The description of the methods and the corresponding results are presented in this appendix.

10.3.1 The analysis of total lipid and total protein using low-field NMR instruments[1]

Time-domain nuclear magnetic resonance was applied for the compositional analysis of germinating seeds. The mq60 instrument (Bruker GmbH, Rheinstetten Germany) has a magnetic field strength of 0.5 T and allows high throughput analysis of major seed traits [Rol15]. It was used for the analysis of total lipid content in either intact seeds or parts thereof. Material from germination experiments (either intact seeds or freeze-dried hand-dissected material) was measured by standard procedures, as described in [Bor11].

All samples were dried at 60 °C overnight. Metabolic intermediates were extracted with chloroform/methanol/water [Sch14]. The analysis of soluble sugars was performed by ion chromatography using pulsed amperometric detection (ICS-3000, Dionex, USA). Separation of the sample extract was carried out on a Dionex PA1 column (2 x 250 mm) and a guard column (PA1 2 x 50 mm) at 25 °C by applying an isocratic run with 100 mM NaOH at constantflow rate of 0.35 mL/min over 40 min. Authentic standards (Sigma, Germany) were used for external calibration.

All other metabolic intermediates were analyzed using capillary electrophoresis (CESI 8000, SCIEX, USA) coupled to mass spectrometry (ABI4000, SCIEX) [Gul16]. Injection time was set to 15 s (corresponding to ∼14 nl injection volume); the mass spectrometer was used in negative ion mode. Ions were detected using multiple reaction monitoring (MRM). The following MRM transitions were used: substance/Q1 mass/Q2 mass/declustering potential/collision energy for sucrose-6-phosphate/421/79/-95/-98, for 3-PGA/185/97/-35/-20, and for phosphoenolpyruvate/167/79/-35/-14. Nitrogen was used as a curtain gas, nebulizer gas, and collision gas. The ion spray voltage was set to 1,200 V, the capillary temperature was set to ambient (20 °C), and the dwell time for all compounds was 100 ms.

[1] The measurements and analyses were performed by Sabine Herrmann (IPK Gatersleben).

10.3.2 4D Volume-Rendering[2]

A visual investigation based on volume renderings of the 4D NMR-monitoring data [Kau05] was conducted. Generation of the rendering could be performed by using the software framework MeVisLab (MeVis Fraunhofer, Bremen, Germany) in combination with an integrated Giga Voxel Renderer (GVR), a GPU-accelerated, high-quality ray casting approach. Manual adjustment of the transfer functions for mapping data values to colour and opacity emphasized regions exhibiting high signal intensities due to incoming water.

Due to the uptake of water, the seed's volume increases over time. For quantification of the overall change in volume, a segmentation at each point in time was performed by employing an active contour approach. It was used since it requires no edge information but is instead based on the Mumford–Shah functional for segmentation [Cha01]. The approach is able to cope with very noisy data and extract objects whose boundaries are not necessarily defined by a strong gradient.

For the segmentation of the seeds, the agar surrounding the seeds was cropped by employing the software ITK-SNAP [Yus06]. While this is a time-consuming process that has to be carried out for all points in time, it is still much faster than manually segmenting the entire seed. The segmentation of each seed results in a closed surface per point in time whose enclosed volume is computed.

An initial spherical contour is positioned by the user in the centre of the seed at time t0. Since the location of the seed varies only slightly over time, the same position is employed to segment the remaining points in time. In an iterative process, the sphere is inflated, considering a weighted combination of external image and internal forces, until it touches the bordering agar medium. The weights and the number of iterations have been fine-tuned based on a sample of points in time. A visual verification showed that the obtained values yielded adequate results for all 110 points in time.

[2]The analyses were performed by Steffen Oeltze-Jafra (ICCAS, Innovation centre Computer Assisted Surgery, University of Leipzig).

10.4 Hardware

In this appendix, the technical information of the NMR scanners and resonators used in this work are provided.

10.4.1 NMR Scanners

Complete Name	Bruker AMX 500
Manufacturer	Oxford Instruments, Abingdon, UK & Bruker Biospin, Rheinstetten, Germany
Field strength	11.74 T
^{1}H NMR frequency	500.132 MHz
Gradient strength	660 mT/m
Operation software	ParaVision 4.0
Location	Department of Experimental Physics 5, University of Würzburg

Data 10.1: Technical information of the Bruker AMX in Würzburg

Complete Name	Bruker Avance 750 WB
Manufacturer	Bruker Biospin, Rheinstetten, Germany
Field strength	17.6 T
^{1}H NMR frequency	approx. 747 MHz
Gradient strength	1,000 mT/m
Operation software	ParaVision 4.0
Location	Department of Experimental Physics 5, University of Würzburg

Data 10.2: Technical information of the Bruker Avance 750 WB in Würzburg

Complete Name	Agilent 14 T 600 MHz
Manufacturer	Varian Inc., Palo Alto, California, USA & Agilent, Santa Clara, California, USA
Field strength	14.0 T
^{1}H NMR frequency	599.719 MHz
Gradient strength	1,000 mT/m
Operation software	VNMRJ 4.0 A
Location	Huck Institutes of the Life Sciences, High Field Magnetic Resonance Center, Penn State University, Pennsylvania, USA

Data 10.3: Technical information of the Varian 14 T at Penn State University

Complete Name	Bruker Avance III HD 400 WB
Manufacturer	Bruker Biospin, Rheinstetten, Germany
Field strength	9.39 T
^{1}H NMR frequency	400.132 MHz
Gradient strength	1,000 mT/m
Operation software	ParaVision 6.0
Location	Leibniz Institute of Plant Genetics and Crop Plant Research (IPK), Gatersleben, Germany

Data 10.4: Technical information of the Bruker Avance III HD 400 WB at IPK Gatersleben

10.4.2 NMR Resonators

^{1}H 5 mm Helmholtz coil

Name	^{1}H 5 mm Helmholtz
Manufacturer	I. Kaufmann, EP5, University of Würzburg
Type	Helmholtz coil
^{1}H NMR frequency	500.132 MHz
inner diameter	5 mm

Data 10.5: Technical information of the ^{1}H 5 mm Helmholtz coil

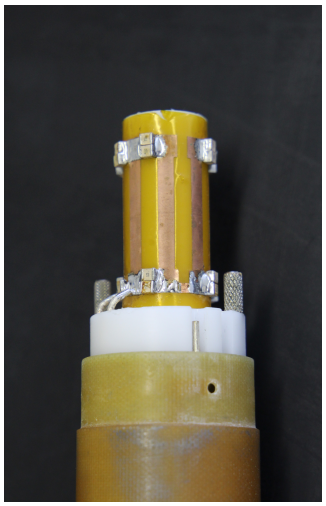

^{1}H ^{19}F 17 mm birdcage coil

Name	^{1}H ^{19}F 17 mm Birdcage
Manufacturer	A. Vilter, EP5, University of Würzburg
Type	Birdcage coil
^{1}H NMR frequency	500.132 MHz
inner diameter	17 mm

Data 10.6: Technical information of the ^{1}H ^{19}F 17 mm birdcage coil

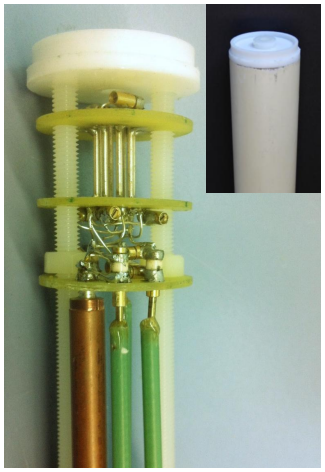

^{1}H ^{13}C 5 mm saddle coil

Name	^{1}H ^{13}C 5 mm Saddle
Manufacturer	F. Fidler, EP5, University of Würzburg
Type	Double-resonant saddle coil
^{1}H NMR frequency	747.000 MHz
inner diameter	5 mm

Data 10.7: Technical information of the ^{1}H ^{13}C 5 mm saddle coil

^{1}H 20 mm birdcage coil

Name	^{1}H 20 mm Birdcage
Manufacturer	EP5, University of Würzburg
Type	Birdcage coil
^{1}H NMR frequency	747.000 MHz
inner diameter	20 mm

Data 10.8: Technical information of the ^{1}H 20 mm birdcage coil

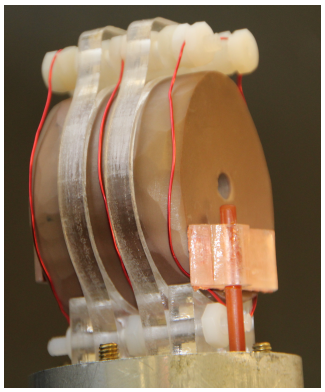

^{1}H 5 mm ceramic resonator

Name	^{1}H 5 mm ceramic resonator
Manufacturer	The Huck Institutes of Life Sciences, The Pennsylvania State University
Type	Ceramic resonator
^{1}H NMR frequency	599.719 MHz
Inner diameter	5 mm

Data 10.9: Technical information of the ^{1}H 5 mm ceramic resonator

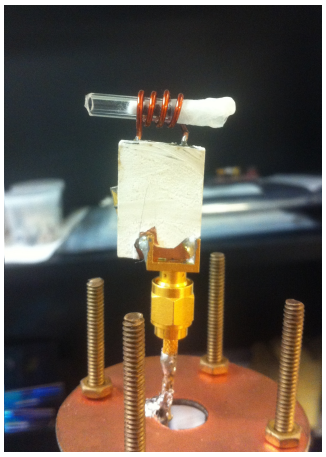

^{1}H 4 mm solenoid coil

Name	^{1}H 4 mm solenoid coil
Manufacturer	The Huck Institutes of Life Sciences, The Pennsylvania State University
Type	solenoid coil
^{1}H NMR frequency	599.719 MHz
Inner diameter	4 mm

Data 10.10: Technical information of the ^{1}H 4 mm solenoid coil

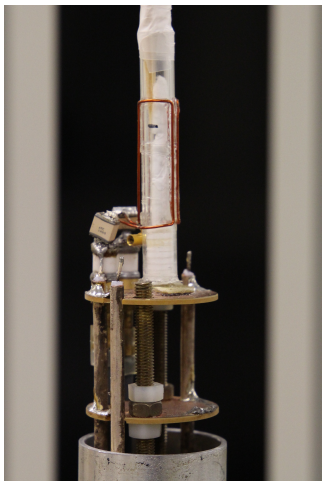

^{1}H 9 mm saddle coil

Name	^{1}H 9 mm saddle coil
Manufacturer	The Huck Institutes of Life Sciences, The Pennsylvania State University
Type	saddle coil
^{1}H NMR frequency	599.719 MHz
Inner diameter	9 mm

Data 10.11: Technical information of the ^{1}H 9 mm saddle coil

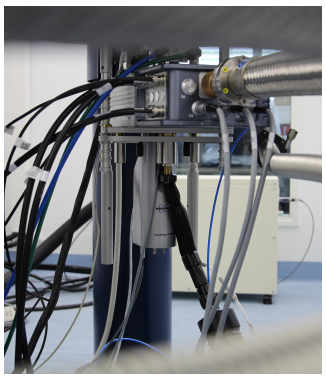

^{1}H-^{13}C-CryoProbehead

Name	^{1}H-^{13}C-CryoProbehead
Manufacturer	Bruker Biospin, Rheinstetten, Germany
Type	saddle coil
^{1}H NMR frequency	400.132 MHz
Inner diameter	5 mm

Data 10.12: Technical information of the ^{1}H-^{13}C 5 mm CryoProbehead

List of Figures

Chapter 10
Bibliography

Articles

[Ale12] Nikos Alexandratos, Jelle Bruinsma, et al. "World agriculture towards 2030/2050: the 2012 revision". In: *ESA Working paper FAO, Rome (Techn. Report)* (2012).

[All15] Doug K Allen, Philip D Bates, and Henrik Tjellström. "Tracking the metabolic pulse of plant lipid production with isotopic labeling and flux analyses: Past, present and future". In: *Progress in lipid research* 58 (2015), pp. 97–120.

[And10] Vyacheslav Andrianov, Nikolai Borisjuk, Natalia Pogrebnyak, Anita Brinker, Joseph Dixon, Sergei Spitsin, John Flynn, Paulina Matyszczuk, Karolina Andryszak, Marilyn Laurelli, et al. "Tobacco as a production platform for biofuel: overexpression of Arabidopsis DGAT and LEC2 genes increases accumulation and shifts the composition of lipids in green biomass". In: *Plant biotechnology journal* 8.3 (2010), pp. 277–287.

[Ann08] Sanjay Annarao, OP Sidhu, Raja Roy, Rakesh Tuli, and CL Khetrapal. "Lipid profiling of developing Jatropha curcas L. seeds using 1 H NMR spectroscopy". In: *Bioresource Technology* 99.18 (2008), pp. 9032–9035.

[Arm04] JK Armstrong, RB Wenby, HJ Meiselman, and TC Fisher. "The hydrodynamic radii of macromolecules and their effect on red blood cell aggregation". In: *Biophysical journal* 87.6 (2004), pp. 4259–4270.

[Ayt08] Zehra Aytac, Gülcan Kinaci, and Engin Kinaci. "Genetic variation, heritability and path analysis of summer rapeseed cultivars". In: *J. Appl. Biol. Sci* 2.3 (2008), pp. 35–39.

[Ban16] Sunil Bansal and Timothy P Durrett. "Camelina sativa: An ideal platform for the metabolic engineering and field production of industrial lipids". In: *Biochimie* 120 (2016), pp. 9–16.

[Bar12] Guillaume Barthole, Loïc Lepiniec, Peter M Rogowsky, and Sébastien Baud. "Controlling lipid accumulation in cereal grains". In: *Plant science* 185 (2012), pp. 33–39.

[Ber91] CJ Bergin, JM Pauly, and A Macovski. "Lung parenchyma: projection reconstruction MR imaging." In: *Radiology* 179.3 (1991), pp. 777–781.

[Bew97] JD Bewley. "Seed dormancy and germination". In: *The plant cell* 9.7 (1997), pp. 1055–1066.

[Blo46] Felix Bloch. "Nuclear induction". In: *Physical review* 70.7-8 (1946), p. 460.

[Blo05] Kai Tobias Block and Jens Frahm. "Spiral imaging: a critical appraisal". In: *Journal of Magnetic Resonance Imaging* 21.6 (2005), pp. 657–668.

[Blü09] Peter Blümler, Carel W Windt, and Dagmar van Dusschoten. "Magnetic resonance in plants". In: *Nova Acta Leopoldina* 357 (2009), pp. 17–30.

[Bor02] Ljudmilla Borisjuk, Trevor L Wang, Hardy Rolletschek, Ulrich Wobus, and Hans Weber. "A pea seed mutant affected in the differentiation of the embryonic epidermis is impaired in embryo growth and seed maturation". In: *Development* 129.7 (2002), pp. 1595–1607.

[Bor11] Ljudmilla Borisjuk, Hardy Rolletschek, Johannes Fuchs, Gerd Melkus, and Thomas Neuberger. "Low and high field magnetic resonance for in vivo analysis of seeds". In: *Materials* 4.8 (2011), pp. 1426–1439.

[Bor12] Ljudmilla Borisjuk, Hardy Rolletschek, and Thomas Neuberger. "Surveying the plant's world by magnetic resonance imaging". In: *The Plant Journal* 70.1 (2012), pp. 129–146.

[Bor13a] Ljudmilla Borisjuk, Hardy Rolletschek, and Thomas Neuberger. "Nuclear magnetic resonance imaging of lipid in living plants". In: *Progress in lipid research* 52.4 (2013), pp. 465–487.

[Bor13b] Ljudmilla Borisjuk, Thomas Neuberger, Jörg Schwender, Nicolas Heinzel, Stephanie Sunderhaus, Johannes Fuchs, Jordan O Hay, Henning Tschiersch, Hans-Peter Braun, Peter Denolf, et al. "Seed architecture shapes embryo metabolism in oilseed rape". In: *The Plant Cell* 25.5 (2013), pp. 1625–1640.

[Bot86] Paul A Bottomley, Hugo H Rogers, and Thomas H Foster. "NMR imaging shows water distribution and transport in plant root systems in situ". In: *Proceedings of the National Academy of Sciences* 83.1 (1986), pp. 87–89.

[Bou82] GW Bourne and JM Trifaro. "The gadolinium ion: a potent blocker of calcium channels and catecholamine release from cultured chromaffin cells". In: *Neuroscience* 7.7 (1982), pp. 1615–1622.

[Boy82] John S Boyer. "Plant productivity and environment". In: *Science* 218.4571 (1982), pp. 443–448.

[Bre07] Maria Antonietta Brescia, Tonietta Pugliese, Edme Hardy, and Antonio Sacco. "Compositional and structural investigations of ripening of table olives, Bella della Daunia, by means of traditional and magnetic resonance imaging analyses". In: *Food chemistry* 105.1 (2007), pp. 400–404.

[Bro86] John M Brown, G Allan Johnson, and Paul J Kramer. "In vivo magnetic resonance microscopy of changing water content in Pelargonium hortorum roots". In: *Plant Physiology* 82.4 (1986), pp. 1158–1160.

[Cal94] Paul T Callaghan, Christopher J Clark, and Lucy C Forde. "Use of static and dynamic NMR microscopy to investigate the origins of contrast in images of biological tissues". In: *Biophysical chemistry* 50.1-2 (1994), pp. 225–235.

[Can16] Núria Canela, Miguel Ángel Rodríguez, Isabel Baiges, Pedro Nadal, and Lluís Arola. "Foodomics imaging by mass spectrometry and magnetic resonance". In: *Electrophoresis* (2016).

[Can00] MJ Canny. "Water transport at the extreme–restoring the hydraulic system in a resurrection plant". In: *The New Phytologist* 148.2 (2000), pp. 187–193.

[Car16] Maria GA Carosio, Diego F Bernardes, Fabiana D Andrade, Tiago B Moraes, Giancarlo Tosin, and Luiz A Colnago. "Measuring thermal properties of oilseeds using time domain nuclear magnetic resonance spectroscopy". In: *Journal of Food Engineering* 173 (2016), pp. 143–149.

[Cha01] Tony F Chan and Luminita A Vese. "Active contours without edges". In: *IEEE Transactions on image processing* 10.2 (2001), pp. 266–277.

[Cha12] Kent D Chapman and John B Ohlrogge. "Compartmentation of triacylglycerol accumulation in plants". In: *Journal of Biological Chemistry* 287.4 (2012), pp. 2288–2294.

[Cha03] Karyn E Chappell, Nayna Patel, Peter D Gatehouse, Janice Main, Basant K Puri, Simon D Taylor-Robinson, and Graeme M Bydder. "Magnetic resonance imaging of the liver with ultrashort TE (UTE) pulse sequences". In: *Journal of Magnetic Resonance Imaging* 18.6 (2003), pp. 709–713.

[Che07] Wei Chen, Yan Zhang, Xueping Liu, Baoyuan Chen, Jinxing Tu, and Fu Tingdong. "Detection of QTL for six yield-related traits in oilseed rape (Brassica napus) using DH and immortalized F2 populations". In: *Theoretical and Applied Genetics* 115.6 (2007), pp. 849–858.

[Cho09] Brendan Choat, Greg A Gambetta, Kenneth A Shackel, and Mark A Matthews. "Vascular function in grape berries across development and its relevance to apparent hydraulic isolation". In: *Plant physiology* 151.3 (2009), pp. 1677–1687.

[Cof89] Gary P Cofer, John M Brown, and G Allan Johnson. "In vivo magnetic resonance microscopy at 5 μm". In: *Journal of Magnetic Resonance (1969)* 83.3 (1989), pp. 608–616.

[Col07] Luiz Alberto Colnago, Mario Engelsberg, André Alves Souza, and Lúcio Leonel Barbosa. "High-throughput, non-destructive determination of oil content in intact seeds by continuous wave-free precession NMR". In: *Analytical chemistry* 79.3 (2007), pp. 1271–1274.

[Con87] A Connelly, JAB Lohman, BC Loughman, H Quiquampoix, and RG Ratcliffe. "High Resolution Imaging of Plant Tissues". In: *Journal of Experimental Botany* 38.10 (1987), pp. 1713–1723.

[Cos17] Maria-Cecília D Costa, Mariana AS Artur, Julio Maia, Eef Jonkheer, Martijn FL Derks, Harm Nijveen, Brett Williams, Sagadevan G Mundree, José M Jiménez-Gómez, Thamara Hesselink, et al. "A footprint of desiccation tolerance in the genome of Xerophyta viscosa". In: *Nature plants* 3.4 (2017), nplants201738.

[Day08] Fabian M Dayrit, Olivia Erin M Buenafe, Edward T Chainani, and Ian Mitchelle S De Vera. "Analysis of monoglycerides, diglycerides, sterols, and free fatty acids in coconut (Cocos nucifera L.) oil by 31P NMR spectroscopy". In: *Journal of agricultural and food chemistry* 56.14 (2008), pp. 5765–5769.

[DR16] Bert De Rybel, Ari Pekka Mähönen, Yrjö Helariutta, and Dolf Weijers. "Plant vascular development: from early specification to differentiation". In: *Nature reviews. Molecular cell biology* 17.1 (2016), p. 30.

[Dea17] Ryan J Dean, Simon J Clarke, Suzy Y Rogiers, Timothy Stait-Gardner, and William S Price. "Solute transport within grape berries inferred from the paramagnetic properties of manganese". In: *Functional Plant Biology* 44.10 (2017), pp. 969–977.

[Dew14] Khaled Dewan and Hanan El-saadany. "Dynamic contrast enhanced MRI of wrist as a useful diagnostic tool in early rheumatoid arthritis". In: *The Egyptian Journal of Radiology and Nuclear Medicine* 45.3 (2014), pp. 803–810.

[Die00] W Diepenbrock. "Yield analysis of winter oilseed rape (Brassica napus L.): a review". In: *Field Crops Research* 67.1 (2000), pp. 35–49.

[Din93] Jiu Ping Ding and Barbara G Pickard. "Mechanosensory calcium-selective cation channels in epidermal cells". In: *The Plant Journal* 3.1 (1993), pp. 83–110.

[Dur11] Timothy P Durrett, Sean E Weise, Christoph Benning, et al. "Increasing the energy density of vegetative tissues by diverting carbon from starch to oil biosynthesis in transgenic Arabidopsis". In: *Plant biotechnology journal* 9.8 (2011), pp. 874–883.

[Duy98] JH Duyn, Y Yang, JA Frank, and JW van der Veen. "Simple correction method for k-space trajectory deviations in MRI." In: *Journal of magnetic resonance (San Diego, Calif.: 1997)* 132.1 (1998), p. 150.

[EK11] Riham H El Khouli, Katarzyna J Macura, Ihab R Kamel, Michael A Jacobs, and David A Bluemke. "3-T dynamic contrast-enhanced MRI of the breast: pharmacokinetic parameters versus conventional kinetic curve analysis". In: *American Journal of Roentgenology* 197.6 (2011), pp. 1498–1505.

[Erm10] Yury A Ermakov, Kishore Kamaraju, Krishnendu Sengupta, and Sergei Sukharev. "Gadolinium ions block mechanosensitive channels by altering the packing and lateral pressure of anionic lipids". In: *Biophysical journal* 98.6 (2010), pp. 1018–1027.

[Fab14] Hilary T Fabich, Martin Benning, Andrew J Sederman, and Daniel J Holland. "Ultrashort echo time (UTE) imaging using gradient pre-equalization and compressed sensing". In: *Journal of Magnetic Resonance* 245 (2014), pp. 116–124.

[Far11] Jill M Farrant and John P Moore. "Programming desiccation-tolerance: from plants to seeds to resurrection plants". In: *Current opinion in plant biology* 14.3 (2011), pp. 340–345.

[Fer02] Cristina Ferrándiz. "Regulation of fruit dehiscence in Arabidopsis". In: *Journal of Experimental Botany* 53.377 (2002), pp. 2031–2038.

[Fes03] Jeffrey A Fessler and Bradley P Sutton. "Nonuniform fast Fourier transforms using min-max interpolation". In: *IEEE Transactions on Signal Processing* 51.2 (2003), pp. 560–574.

[FS06] William E Finch-Savage and Gerhard Leubner-Metzger. "Seed dormancy and the control of germination". In: *New phytologist* 171.3 (2006), pp. 501–523.

[FS15] William E Finch-Savage and George W Bassel. "Seed vigour and crop establishment: extending performance beyond adaptation". In: *Journal of experimental botany* 67.3 (2015), pp. 567–591.

[Fit15] Ana Fita, Adrián Rodríguez-Burruezo, Monica Boscaiu, Jaime Prohens, and Oscar Vicente. "Breeding and domesticating crops adapted to drought and salinity: a new paradigm for increasing food production". In: *Frontiers in plant science* 6 (2015), p. 978.

[Fou93] Loic Foucat, Andre Chavagnat, and Jean-Pierre Renou. "Nuclear magnetic resonance micro-imaging and X-radiography as possible techniques to study seed germination". In: *Scientia Horticulturae* 55.3-4 (1993), pp. 323–331.

[Fuc13] Johannes Fuchs, Thomas Neuberger, Hardy Rolletschek, Silke Schiebold, Thuy Ha Nguyen, Nikolai Borisjuk, Andreas Börner, Gerd Melkus, Peter Jakob, and Ljudmilla Borisjuk. "A noninvasive platform for imaging and quantifying oil storage in submillimeter tobacco seed". In: *Plant physiology* 161.2 (2013), pp. 583–593.

[Fuc15] Johannes Fuchs, Gerd Melkus, Ljudmilla Borisjuk, and Peter Jakob. "Tracking metabolite dynamics in plants via indirect 13C chemical shift imaging with an interleaved variable density acquisition weighted sampling pattern". In: *Magnetic Resonance Materials in Physics, Biology and Medicine* 28.2 (2015), pp. 127–134.

[Gao08] Chunfang Gao, Wei Xiong, Yiliang Zhang, Wenqiao Yuan, and Qingyu Wu. "Rapid quantitation of lipid in microalgae by time-domain nuclear magnetic resonance". In: *Journal of microbiological methods* 75.3 (2008), pp. 437–440.

[Gar07] Małgorzata Garnczarska, Tomasz Zalewski, and Marek Kempka. "Changes in water status and water distribution in maturing lupin seeds studied by MR imaging and NMR spectroscopy". In: *Journal of experimental botany* 58.14 (2007), pp. 3961–3969.

[Gli06] SM Glidewell. "NMR imaging of developing barley grains". In: *Journal of Cereal Science* 43.1 (2006), pp. 70–78.

[God10] H Charles J Godfray, John R Beddington, Ian R Crute, Lawrence Haddad, David Lawrence, James F Muir, Jules Pretty, Sherman Robinson, Sandy M Thomas, and Camilla Toulmin. "Food security: the challenge of feeding 9 billion people". In: *science* 327.5967 (2010), pp. 812–818.

[Gol93] Garry E Gold, John M Pauly, Gary H Glover, John C Moretto, Albert Macovski, and Robert J Herfkens. "Characterization of atherosclerosis with a 1.5-T imaging system". In: *Journal of Magnetic Resonance Imaging* 3.2 (1993), pp. 399–407.

[Gol95] Garry E Gold, John M Pauly, Albert Macovski, and Robert J Herfkens. "MR spectroscopic imaging of collagen: tendons and knee menisci". In: *Magnetic resonance in medicine* 34.5 (1995), pp. 647–654.

[Gri17] Eckhard Grimm, Daniel Pflugfelder, Dagmar van Dusschoten, Andreas Winkler, and Moritz Knoche. "Physical rupture of the xylem in developing sweet cherry fruit causes progressive decline in xylem sap inflow rate". In: *Planta* 246.4 (2017), pp. 659–672.

[Gro15] Marina Gromova, Armel Guillermo, Pierre-Alain Bayle, and Michel Bardet. "In vivo measurement of the size of oil bodies in plant seeds using a simple and robust pulsed field gradient NMR method". In: *European Biophysics Journal* 44.3 (2015), pp. 121–129.

[Gru70] Scott M Grundy and EH Ahrens Jr. "The effects of unsaturated dietary fats on absorption, excretion, synthesis, and distribution of cholesterol in man". In: *Journal of Clinical Investigation* 49.6 (1970), p. 1135.

[Gru02] Marco LH Gruwel, Xiang S Yin, Michael J Edney, Steve W Schroeder, Alex W MacGregor, and Suzanne Abrams. "Barley viability during storage: use of magnetic resonance as a potential tool to study viability loss". In: *Journal of Agricultural and Food Chemistry* 50.4 (2002), pp. 667–676.

[Gul16] Mehmet Can Gulersonmez, Stephen Lock, Thomas Hankemeier, and Rawi Ramautar. "Sheathless capillary electrophoresis-mass spectrometry for anionic metabolic profiling". In: *Electrophoresis* 37.7-8 (2016), pp. 1007–1014. ISSN: 1522-2683.

[Gus93] M Gussoni, F Greco, R Consonni, H Molinari, G Zannoni, G Bianchi, and L Zetta. "Application of NMR microscopy to the histochemistry study of olives (Olea europaea L.)" In: *Magnetic resonance imaging* 11.2 (1993), pp. 259–268.

[Gus94] M Gussoni, F Greco, M Pegna, G Bianchi, and L Zetta. "Solid state and microscopy NMR study of the chemical constituents of Afzelia cuanzensis seeds". In: *Magnetic resonance imaging* 12.3 (1994), pp. 477–486.

[Gus01] M Gussoni, F Greco, A Vezzoli, T Osuga, and L Zetta. "Magnetic resonance imaging of molecular transport in living morning glory stems". In: *Magnetic resonance imaging* 19.10 (2001), pp. 1311–1322.

[Haa85] Axel Haase, Jens Frahm, Wolfgang Hanicke, and Dietmar Matthaei. "1H NMR chemical shift selective (CHESS) imaging". In: *Physics in medicine and biology* 30.4 (1985), p. 341.

[Hah50] Erwin L Hahn. "Spin echoes". In: *Physical review* 80.4 (1950), p. 580.

[Hal61] TJ Haley, K Raymond, N Komesu, and HC Upham. "Toxicological and pharmacological effects of gadolinium and samarium chlorides". In: *British journal of pharmacology and chemotherapy* 17.3 (1961), pp. 526–532.

[Hal71] Shelagh M Hall, Dennis A Baker, and John A Milburn. "Phloem transport of 14 C-labelled assimilates in Ricinus". In: *Planta* 100.3 (1971), pp. 200–207.

[Hal93] John M Halloin, Thomas G Cooper, E James Potchen, and Tommy E Thompson. "Proton magnetic resonance imaging of lipid in pecan embryos". In: *Journal of the American Oil Chemists' Society* 70.12 (1993), pp. 1259–1262.

[Han08] Lars G Hanson. "Is quantum mechanics necessary for understanding magnetic resonance?" In: *Concepts in Magnetic Resonance Part A* 32.5 (2008), pp. 329–340.

[Hay11] Daniel M Hayden, Hardy Rolletschek, Ljudmilla Borisjuk, Jason Corwin, Daniel J Kliebenstein, Asa Grimberg, Sten Stymne, and Katayoon Dehesh. "Cofactome analyses reveal enhanced flux of carbon into oil for potential biofuel production". In: *The Plant Journal* 67.6 (2011), pp. 1018–1028.

[He04] Qiuhong He, Ray Z Xu, Pavel Shkarin, Giuseppe Pizzorno, Carol H Lee-French, Douglas L Rothman, Dikoma C Shungu, and Hyunsuk Shim. "Magnetic resonance spectroscopic imaging of tumor metabolic markers for cancer diagnosis, metabolic phenotyping, and characterization of tumor microenvironment". In: *Disease markers* 19.2, 3 (2004), pp. 69–94.

[He07] Qiuhong He, Pavel Shkarin, Regina J Hooley, Donald R Lannin, Jeffrey C Weinreb, and Veerle Ilse Julie Bossuyt. "In vivo MR spectroscopic imaging of polyunsaturated fatty acids (PUFA) in healthy and cancerous breast tissues by selective multiple-quantum coherence transfer (Sel-MQC): A preliminary study". In: *Magnetic resonance in medicine* 58.6 (2007), pp. 1079–1085.

[Hei06] Melanie Heilmann, Fabian Kiessling, Marta Enderlin, and Lothar R Schad. "Determination of pharmacokinetic parameters in DCE MRI: consequence of nonlinearity between contrast agent concentration and signal intensity". In: *Investigative radiology* 41.6 (2006), pp. 536–543.

[Hem15] Kathrin RF Hemberger, Peter M Jakob, and Felix A Breuer. "Multiparametric oxygen-enhanced functional lung imaging in 3D". In: *Magnetic Resonance Materials in Physics, Biology and Medicine* 28.3 (2015), pp. 217–226.

[Hem14] O Hemminki, R Immonen, J Närväinen, A Kipar, J Paasonen, KT Jokivarsi, H Yli-Ollila, P Soininen, K Partanen, T Joensuu, et al. "In vivo magnetic resonance imaging and spectroscopy identifies oncolytic adenovirus responders". In: *International journal of cancer* 134.12 (2014), pp. 2878–2890.

[Hen86] J Hennig, A Nauerth, and H Friedburg. "RARE imaging: a fast imaging method for clinical MR". In: *Magnetic resonance in medicine* 3.6 (1986), pp. 823–833.

[Hey14] Anna K Heye, Ross D Culling, Maria del C Valdés Hernández, Michael J Thrippleton, and Joanna M Wardlaw. "Assessment of blood–brain barrier disruption using dynamic contrast-enhanced MRI. A systematic review". In: *NeuroImage: Clinical* 6 (2014), pp. 262–274.

[Hil93] Matthew J Hills, Martin D Watson, and Denis J Murphy. "Targeting of oleosins to the oil bodies of oilseed rape (Brassica napus L.)" In: *Planta* 189.1 (1993), pp. 24–29.

[Höf41] K Höfler, H Migsch, and W Rottenburg. "Über die Austrocknungresistenz landwirtschaftlicher Kulturpflanzen". In: *Forschungsdienst* 12 (1941), pp. 50–61.

[Hon09] Young-Shick Hong, Jee-Hyun Cho, Na-Ri Kim, Chulhyun Lee, Chaejoon Cheong, Kwan Soo Hong, and Cherl-Ho Lee. "Artifacts in the measurement of water distribution in soybeans using MR imaging". In: *Food chemistry* 112.1 (2009), pp. 267–272.

[Hor12] Patrick J Horn, Andrew R Korte, Purnima B Neogi, Ebony Love, Johannes Fuchs, Kerstin Strupat, Ljudmilla Borisjuk, Vladimir Shulaev, Young-Jin Lee, and Kent D Chapman. "Spatial mapping of lipids at cellular resolution in embryos of cotton". In: *The Plant Cell* 24.2 (2012), pp. 622–636.

[Hor13] Patrick J Horn, Jillian E Silva, Danielle Anderson, Johannes Fuchs, Ljudmilla Borisjuk, Tara J Nazarenus, Vladimir Shulaev, Edgar B Cahoon, and Kent D Chapman. "Imaging heterogeneity of membrane and storage lipids in transgenic Camelina sativa seeds with altered fatty acid profiles". In: *The Plant Journal* 76.1 (2013), pp. 138–150.

[Hu08] Qiang Hu, Milton Sommerfeld, Eric Jarvis, Maria Ghirardi, Matthew Posewitz, Michael Seibert, and Al Darzins. "Microalgal triacylglycerols as feedstocks for biofuel production: perspectives and advances". In: *The plant journal* 54.4 (2008), pp. 621–639.

[Hub15] Michiel Hubeau and Kathy Steppe. "Plant-PET scans: in vivo mapping of xylem and phloem functioning". In: *Trends in plant science* 20.10 (2015), pp. 676–685.

[Hwa03] Jong-Hee Hwang, Stefan Bluml, Alexander Leaf, and Brian D Ross. "In vivo characterization of fatty acids in human adipose tissue using natural abundance 1H decoupled 13C MRS at 1.5 T: clinical applications to dietary therapy". In: *NMR in Biomedicine* 16.3 (2003), pp. 160–167.

[Ish96] N Ishida, M Koizumi, and H Kano. "Location of sugars in barley seeds during germination by NMR microscopy". In: *Plant, Cell & Environment* 19.12 (1996), pp. 1415–1422.

[Joh87] G Allan Johnson, John Brown, and Paul J Kramer. "Magnetic resonance microscopy of changes in water content in stems of transpiring plants". In: *Proceedings of the National Academy of Sciences* 84.9 (1987), pp. 2752–2755.

[Joh92] RW Johnson, MA Dixon, and DR Lee. "Water relations of the tomato during fruit growth". In: *Plant, Cell & Environment* 15.8 (1992), pp. 947–953.

[Kar14] Ralf Kartäusch, Xavier Helluy, Peter Michael Jakob, and Florian Fidler. "Optimization of the AC-gradient method for velocity profile measurement and application to slow flow". In: *Journal of Magnetic Resonance* 248 (2014), pp. 131–136.

[Kel06] Markus Keller, Jason P Smith, and Bhaskar R Bondada. "Ripening grape berries remain hydraulically connected to the shoot". In: *Journal of Experimental Botany* 57.11 (2006), pp. 2577–2587.

[Kik06] Kaori Kikuchi, Mika Koizumi, Nobuaki Ishida, and Hiromi Kano. "Water uptake by dry beans observed by micro-magnetic resonance imaging". In: *Annals of botany* 98.3 (2006), pp. 545–553.

[Kis84] Mordechai E Kislev. "Emergence of wheat agriculture". In: *Paleorient* (1984), pp. 61–70.

[Kno10] Michael Knoblauch and Winfried S Peters. "Münch, morphology, microfluidics - our structural problem with the phloem". In: *Plant, cell & environment* 33.9 (2010), pp. 1439–1452.

[Kno04] Gerhard Knothe and James A Kenar. "Determination of the fatty acid profile by 1H-NMR spectroscopy". In: *European Journal of Lipid Science and Technology* 106.2 (2004), pp. 88–96.

[Köc01] Walter Köckenberger. "Nuclear magnetic resonance micro-imaging in the investigation of plant cell metabolism". In: *Journal of experimental botany* 52.356 (2001), pp. 641–652.

[Koi08] Mika Koizumi, Kaori Kikuchi, Seiichiro Isobe, Nobuaki Ishida, Shigehiro Naito, and Hiromi Kano. "Role of seed coat in imbibing soybean seeds observed by micro-magnetic resonance imaging". In: *Annals of botany* 102.3 (2008), pp. 343–352.

[Koi14] Mika Koizumi and Hiromi Kano. "Lens: Water channel for dry broad bean seeds at germination observed by micro-magnetic resonance imaging". In: *American Journal of Biology and Life Sciences* 2.2 (2014), p. 37.

[Kot05] John J Kotyk, Marty D Pagel, Kevin L Deppermann, Ronald F Colletti, Norman G Hoffman, Elias J Yannakakis, Pradip K Das, and Joseph JH Ackerman. "High-throughput determination of oil content in corn kernels using nuclear magnetic resonance imaging". In: *Journal of the American Oil Chemists' Society* 82.12 (2005), pp. 855–862.

[Kum75] Anil Kumar, Dieter Welti, and Richard R Ernst. "NMR Fourier zeugmatography". In: *Journal of Magnetic Resonance (1969)* 18.1 (1975), pp. 69–83.

[Lar08] Peder EZ Larson, Paul T Gurney, and Dwight G Nishimura. "Anisotropic field-of-views in radial imaging". In: *IEEE transactions on medical imaging* 27.1 (2008), pp. 47–57.

[Lau73] Paul Christian Lauterbur. "Image Formation by Induced Local Interactions: Examples Employing Nuclear Magnetic Resonance". In: *Nature* 242.190 (1973), p. 191.

[Leb89] Robert J Lebowitz. "Image analysis measurements and repeatability estimates of siliqua morphological traits in Brassica campestris L". In: *Euphytica* 43.1-2 (1989), pp. 113–116.

[Lep17] Olivier Leprince, Anthoni Pellizzaro, Souha Berriri, and Julia Buitink. "Late seed maturation: drying without dying". In: *Journal of experimental botany* 68.4 (2017), pp. 827–841.

[Lun01] Ernesto Lunati, Paolo Farace, Elena Nicolato, Claudia Righetti, Pasquina Marzola, Andrea Sbarbati, and Francesco Osculati. "Polyunsaturated fatty acids mapping by 1H MR-chemical shift imaging". In: *Magnetic resonance in medicine* 46.5 (2001), pp. 879–883.

[Ma08] Jingfei Ma. "Dixon techniques for water and fat imaging". In: *Journal of Magnetic Resonance Imaging* 28.3 (2008), pp. 543–558.

[Man73] Peter Mansfield and Peter K Grannell. "NMR'diffraction'in solids?" In: *Journal of Physics C: solid state physics* 6.22 (1973), p. L422.

[Man05] Bertram Manz, Kerstin Müller, Birgit Kucera, Frank Volke, and Gerhard Leubner-Metzger. "Water uptake and distribution in germinating tobacco seeds investigated in vivo by nuclear magnetic resonance imaging". In: *Plant Physiology* 138.3 (2005), pp. 1538–1551.

[MAT97] Masashi MATSUBAYASHI et al. "Water imaging of seeds by neutron beam". In: *Bioimages* 5.2 (1997), pp. 45–48.

[Mat05] Mark A Matthews and Ken A Shackel. "Growth and water transport in fleshy fruit". In: *Vascular transport in plants* (2005), pp. 181–197.

[Maz15] M Mazhar, D Joyce, G Cowin, I Brereton, P Hofman, R Collins, and M Gupta. "Non-destructive 1 h-mri assessment of flesh bruising in avocado (persea americana m.) cv. hass". In: *Postharvest Biology and Technology* 100 (2015), pp. 33–40.

[Mel09b] Gerd Melkus, Hardy Rolletschek, Ruslana Radchuk, Johannes Fuchs, Twan Rutten, Ulrich Wobus, Thomas Altmann, Peter Jakob, and Ljudmilla Borisjuk. "The metabolic role of the legume endosperm: a noninvasive imaging study". In: *Plant physiology* 151.3 (2009), pp. 1139–1154.

[Mel11] Gerd Melkus, Hardy Rolletschek, Johannes Fuchs, Volodymyr Radchuk, Eva Grafahrend-Belau, Nese Sreenivasulu, Twan Rutten, Diana Weier, Nicolas Heinzel, Falk Schreiber, et al. "Dynamic 13C/1H NMR imaging uncovers sugar allocation in the living seed". In: *Plant biotechnology journal* 9.9 (2011), pp. 1022–1037.

[Mil88] B Millet. "Gadolinium ion is an inhibitor suitable for testing the putative role of stretch-activated ion channels in geotropism and thigmotropism". In: *Biophys. J.* 53 (1988), 115a.

[Mit45] HH Mitchell, TS Hamilton, FR Steggerda, and HW Bean. "The chemical composition of the adult human body and its bearing on the biochemistry of growth". In: *Journal of Biological Chemistry* 158.3 (1945), pp. 625–637.

[Miy98] Yuko Miyake, Kazuhisa Yokomizo, and Narihide Matsuzaki. "Determination of unsaturated fatty acid composition by high-resolution nuclear magnetic resonance spectroscopy". In: *Journal of the American Oil Chemists' Society* 75.9 (1998), pp. 1091–1094.

[Mor90] PG Morris, HE Darceuil, A Jasinski, AK Jha, DJO McIntyre, and DH Northcote. "NMR microscopy of the germinating castor bean". In: *Philosophical Transactions of the Royal Society of London A: Mathematical, Physical and Engineering Sciences* 333.1632 (1990), pp. 487–493.

[Mün30] E Münch. "Die Stoffbewegungen in der Pflanze". In: *Jena: Gustav Fischer* (1930).

[Mus05] Livio Muscariello, Francesco Rosso, Gerardo Marino, Antonio Giordano, Manlio Barbarisi, Gennaro Cafiero, and Alfonso Barbarisi. "A critical overview of ESEM applications in the biological field". In: *Journal of cellular physiology* 205.3 (2005), pp. 328–334.

[Nap14] Johnathan A Napier, Richard P Haslam, Frederic Beaudoin, and Edgar B Cahoon. "Understanding and manipulating plant lipid composition: metabolic engineering leads the way". In: *Current opinion in plant biology* 19 (2014), pp. 68–75.

[Nar11] Andrea Nardini, Sebastiano Salleo, and Steven Jansen. "More than just a vulnerable pipeline: xylem physiology in the light of ion-mediated regulation of plant water transport". In: *Journal of experimental botany* 62.14 (2011), pp. 4701–4718.

[Née17] Guillaume Née, Yong Xiang, and Wim JJ Soppe. "The release of dormancy, a wake-up call for seeds to germinate". In: *Current opinion in plant biology* 35 (2017), pp. 8–14.

[Neu08] Thomas Neuberger, Nese Sreenivasulu, Markus Rokitta, Hardy Rolletschek, Cornelia Göbel, Twan Rutten, Volodja Radchuk, Ivo Feussner, Ulrich Wobus, Peter Jakob, et al. "Quantitative imaging of oil storage in developing crop seeds". In: *Plant Biotechnology Journal* 6.1 (2008), pp. 31–45.

[Nie17] Mikkel Schou Nielsen, Kasper Borg Damkjær, and Robert Feidenhans. "Quantitative in-situ monitoring of germinating barley seeds using X-ray dark-field radiography". In: *Journal of Food Engineering* 198 (2017), pp. 98–104.

[Niu11] Chenxing Niu, Nataliya Smith, Philippe Garteiser, Rheal Towner, and Jeanmarie Verchot. "Comparative analysis of protein transport in the N. benthamiana vasculature reveals different destinations." In: *Plant signaling & behavior* 6.11 (2011), pp. 1793–1808.

[Nob00] Park S Nobel and Erick De la Barrera. "Carbon and water balances for young fruits of platyopuntias". In: *Physiologia Plantarum* 109.2 (2000), pp. 160–166.

[Non10] Hiroyuki Nonogaki, George W Bassel, and J Derek Bewley. "Germination—still a mystery". In: *Plant Science* 179.6 (2010), pp. 574–581.

[Osu99] Toshiaki Osuga and Hozumi Tatsuoka. "Effect of 1.5 T steady magnetic field on neuroconduction of a bullfrog sciatic nerve in a partially active state within several hours after extraction". In: *Magnetic resonance imaging* 17.5 (1999), pp. 791–794.

[Oto12] Adriane G Otopalik, Jane Shin, Barbara S Beltz, David C Sandeman, and Nancy H Kolodny. "Differential uptake of MRI contrast agents indicates charge-selective blood-brain interface in the crayfish". In: *Cell and tissue research* 349.2 (2012), pp. 493–503.

[Pac10] Nathan A Pack and Edward VR DiBella. "Comparison of myocardial perfusion estimates from dynamic contrast-enhanced magnetic resonance imaging with four quantitative analysis methods". In: *Magnetic resonance in medicine* 64.1 (2010), pp. 125–137.

[Pau06] Anna-Lisa Paul, Robert J Ferl, and Mark W Meisel. "High magnetic field induced changes of gene expression in arabidopsis". In: *Biomagnetic research and technology* 4.1 (2006), p. 7.

[Pau08] Sandra Pauls, Felix M Mottaghy, Stefan A Schmidt, Stefan Krüger, Peter Möller, Hans-Jürgen Brambs, and Arthur Wunderlich. "Evaluation of lung tumor perfusion by dynamic contrast-enhanced MRI". In: *Magnetic resonance imaging* 26.10 (2008), pp. 1334–1341.

[Peu01] AD Peuke, M Rokitta, U Zimmermann, L Schreiber, and A Haase. "Simultaneous measurement of water flow velocity and solute transport in xylem and phloem of adult plants of Ricinus communis over a daily time course by nuclear magnetic resonance spectrometry". In: *Plant, Cell & Environment* 24.5 (2001), pp. 491–503.

[Pfl17] Daniel Pflugfelder, Ralf Metzner, Dagmar Dusschoten, Rüdiger Reichel, Siegfried Jahnke, and Robert Koller. "Non-invasive imaging of plant roots in different soils using magnetic resonance imaging (MRI)". In: *Plant Methods* 13.1 (2017), p. 102.

[Phi66] John R Philip. "Plant water relations: some physical aspects". In: *Annual Review of Plant Physiology* 17.1 (1966), pp. 245–268.

[Pie02] LN Pietrzak, J Fregeau-Reid, B Chatson, and B Blackwell. "Observations on water distribution in soybean seed during hydration processes using nuclear magnetic resonance imaging". In: *Canadian journal of plant science* 82.3 (2002), pp. 513–519.

[Piv94] James M Pivarnik and RA Palmer. "Water and electrolyte balance during rest and exercise". In: *Nutrition in exercise and sport* 2 (1994), pp. 245–262.

[Poh97] R Pohmann, M Von Kienlin, and A Haase. "Theoretical evaluation and comparison of fast chemical shift imaging methods". In: *Journal of Magnetic Resonance* 129.2 (1997), pp. 145–160.

[Pop91] JM Pope, H Rumpel, W Kuhn, R Walker, D Leach, and V Sarafis. "Applications of chemical-shift-selective NMR microscopy to the non-invasive histochemistry of plant materials". In: *Magnetic resonance imaging* 9.3 (1991), pp. 357–363.

[Pur46] Edward M Purcell, HC Torrey, and Robert V Pound. "Resonance absorption by nuclear magnetic moments in a solid". In: *Physical review* 69.1-2 (1946), p. 37.

[Qui90] H Quiquampoix, RG Ratcliffe, S Ratković, and Ž Vučinić. "1H and 31P NMR investigation of gadolinium uptake in maize roots". In: *Journal of Inorganic Biochemistry* 38.4 (1990), pp. 265–275.

[Raj12] Loïc Rajjou, Manuel Duval, Karine Gallardo, Julie Catusse, Julia Bally, Claudette Job, and Dominique Job. "Seed germination and vigor". In: *Annual review of plant biology* 63 (2012), pp. 507–533.

[Ram85] LE Ramm, MB Whitlow, and MM Mayer. "The relationship between channel size and the number of C9 molecules in the C5b-9 complex." In: *The Journal of immunology* 134.4 (1985), pp. 2594–2599.

[Rat15] Josef Rathbauer and Leopold Lasselsberger. "Eine optimale Heizung für alle gibt es nicht". In: *Österreichische BauernZeitung* (2015), pp. 14–17.

[Rat09] Judith R Rathjen, Ekaterina V Strounina, and Daryl J Mares. "Water movement into dormant and non-dormant wheat (Triticum aestivum L.) grains". In: *Journal of experimental botany* 60.6 (2009), pp. 1619–1631.

[Rob03] Matthew D Robson, Peter D Gatehouse, Mark Bydder, and Graeme M Bydder. "Magnetic resonance: an introduction to ultrashort TE (UTE) imaging". In: *Journal of computer assisted tomography* 27.6 (2003), pp. 825–846.

[Rob06] Matthew D Robson and Graeme M Bydder. "Clinical ultrashort echo time imaging of bone and other connective tissues". In: *NMR in Biomedicine* 19.7 (2006), pp. 765–780.

[Rok99] Markus Rokitta, AD Peuke, Ulrich Zimmermann, and Axel Haase. "Dynamic studies of phloem and xylein flow in fully differentiated plants by fast nuclear-magnetic-resonance microimaging". In: *Protoplasma* 209.1-2 (1999), pp. 126–131.

[Rol11] Hardy Rolletschek, Gerd Melkus, Eva Grafahrend-Belau, Johannes Fuchs, Nicolas Heinzel, Falk Schreiber, Peter M Jakob, and Ljudmilla Borisjuk. "Combined noninvasive imaging and modeling approaches reveal metabolic compartmentation in the barley endosperm". In: *The Plant Cell Online* 23.8 (2011), pp. 3041–3054.

[Rol15] Hardy Rolletschek, Johannes Fuchs, Svetlana Friedel, Andreas Börner, Harald Todt, Peter M Jakob, and Ljudmilla Borisjuk. "A novel noninvasive procedure for high-throughput screening of major seed traits". In: *Plant biotechnology journal* 13.2 (2015), pp. 188–199.

[Sal11] Yuliya A Salanenka and Alan G Taylor. "Seedcoat permeability: uptake and post-germination transport of applied model tracer compounds". In: *HortScience* 46.4 (2011), pp. 622–626.

[Sar09] Bimal Kumar Sarkar, Wei-Yuan Yang, Zhen Wu, Huiru Tang, and Shangwu Ding. "Variations of water uptake, lipid consumption, and dynamics during the germination of Sesamum indicum seed: a nuclear magnetic resonance spectroscopic investigation". In: *Journal of agricultural and food chemistry* 57.18 (2009), pp. 8213–8219.

[Sas05] Makoto Sasaki, Eri Shibata, Yoshiyuki Kanbara, and Shigeru Ehara. "Enhancement effects and relaxivities of gadolinium-DTPA at 1.5 versus 3 Tesla: a phantom study". In: *Magnetic Resonance in Medical Sciences* 4.3 (2005), pp. 145–149.

[Sat09] Jitendra K Satyarthi, D Srinivas, and Paul Ratnasamy. "Estimation of free fatty acid content in oils, fats, and biodiesel by 1H NMR spectroscopy". In: *Energy & Fuels* 23.4 (2009), pp. 2273–2277.

[Sch03] H Schneider, B Manz, M Westhoff, S Mimietz, M Szimtenings, T Neuberger, C Faber, G Krohne, A Haase, F Volke, et al. "The impact of lipid distribution, composition and mobility on xylem water refilling of the resurrection plant Myrothamnus flabellifolia". In: *New Phytologist* 159.2 (2003), pp. 487–505.

[Sha10] Sharifudin Md Shaarani, Arturo Cardenas-Blanco, MH Gao Amin, Ng G Soon, and Laurance D Hall. "Monitoring development and ripeness of oil palm fruit (Elaeis guneensis) by MRI and bulk NMR". In: *International Journal of Agriculture and Biology (Pakistan)* (2010).

[Shi89] Tai-yow Shiao and Ming-shi Shiao. "Determination of fatty acid compositions of triacylglycerols by high resolution NMR spectroscopy". In: *Bot Bull Academia Sinica* 30 (1989), pp. 191–199.

[Sim16] Jeffrey P Simpson and John B Ohlrogge. "A novel pathway for triacylglycerol biosynthesis is responsible for the accumulation of massive quantities of glycerolipids in the surface wax of bayberry (Myrica pensylvanica) fruit". In: *The Plant Cell* 28.1 (2016), pp. 248–264.

[Sin96] Samuel Singer, Mohanram Sivaraja, Kerry Souza, Kevin Millis, and Joseph M Corson. "1H-NMR detectable fatty acyl chain unsaturation in excised leiomyosarcoma correlate with grade and mitotic activity." In: *Journal of Clinical Investigation* 98.2 (1996), p. 244.

[Sri16] Amitava Srimany, Christy George, Hemanta R Naik, Danica Glenda Pinto, N Chandrakumar, and T Pradeep. "Developmental patterning and segregation of alkaloids in areca nut (seed of Areca catechu) revealed by magnetic resonance and mass spectrometry imaging". In: *Phytochemistry* 125 (2016), pp. 35–42.

[Sta05] Ruth Stadler, Christian Lauterbach, and Norbert Sauer. "Cell-to-cell movement of green fluorescent protein reveals post-phloem transport in the outer integument and identifies symplastic domains in Arabidopsis seeds and embryos". In: *Plant physiology* 139.2 (2005), pp. 701–712.

[Ste16] Tina Steinbrecher and Gerhard Leubner-Metzger. "The biomechanics of seed germination". In: *Journal of experimental botany* 68.4 (2016), pp. 765–783.

[Stu12] VJF Sturm, TC Basse-Lüsebrink, T Kampf, G Stoll, and PM Jakob. "Improved encoding strategy for CPMG-based Bloch-Siegert B 1+ mapping". In: *Magnetic resonance in medicine* 68.2 (2012), pp. 507–515.

[Sug16] Ryohei Sugita, Natsuko I Kobayashi, Atsushi Hirose, Takayuki Saito, Ren Iwata, Keitaro Tanoi, and Tomoko M Nakanishi. "Visualization of Uptake of Mineral Elements and the Dynamics of Photosynthates in Arabidopsis by a Newly Developed Real-Time Radioisotope Imaging System (RRIS)". In: *Plant and Cell Physiology* 57.4 (2016), pp. 743–753.

[Ter05a] Victor V Terskikh, J Allan Feurtado, Shane Borchardt, Michael Giblin, Suzanne R Abrams, and Allison R Kermode. "In vivo13C NMR metabolite profiling: potential for understanding and assessing conifer seed quality". In: *Journal of experimental botany* 56.418 (2005), pp. 2253–2265.

[Ter05b] Victor V Terskikh, J Allan Feurtado, Chengwei Ren, Suzanne R Abrams, and Allison R Kermode. "Water uptake and oil distribution during imbibition of seeds of western white pine (Pinus monticola Dougl. ex D. Don) monitored in vivo using magnetic resonance imaging". In: *Planta* 221.1 (2005), pp. 17–27.

[Ter08] Victor V Terskikh, Ying Zeng, J Allan Feurtado, Michael Giblin, Suzanne R Abrams, and Allison R Kermode. "Deterioration of western redcedar (Thuja plicata Donn ex D. Don) seeds: protein oxidation and in vivo NMR monitoring of storage oils". In: *Journal of experimental botany* 59.4 (2008), pp. 765–777.

[Ter11] Victor V Terskikh, Kerstin Müller, Allison R Kermode, and Gerhard Leubner-Metzger. "In Vivo 1 H-NMR Microimaging During Seed Imbibition, Germination, and Early Growth". In: *Seed Dormancy: Methods and Protocols* (2011), pp. 319–327.

[Tho96] E Louise Thomas, Gary Frost, ML Barnard, David J Bryant, Simon D Taylor-Robinson, J Simbrunner, Glyn A Coutts, M Burl, Stephen R Bloom, KD Sales, et al. "An in vivo 13 C magnetic resonance spectroscopic study of the relationship between diet and adipose tissue composition". In: *Lipids* 31.2 (1996), pp. 145–151.

[Tof91] Paul S Tofts and Allan G Kermode. "Measurement of the blood-brain barrier permeability and leakage space using dynamic MR imaging. 1. Fundamental concepts". In: *Magnetic resonance in medicine* 17.2 (1991), pp. 357–367.

[Tri15b] Simon MF Triphan, Felix A Breuer, Daniel Gensler, Hans-Ulrich Kauczor, and Peter M Jakob. "Oxygen enhanced lung MRI by simultaneous measurement of T1 and T2* during free breathing using ultrashort TE". In: *Journal of Magnetic Resonance Imaging* 41.6 (2015), pp. 1708–1714.

[Tro07] Stéphanie Troufflard, Albrecht Roscher, Brigitte Thomasset, Jean-Noël Barbotin, Stephen Rawsthorne, and Jean-Charles Portais. "In vivo 13 C NMR determines metabolic fluxes and steady state in linseed embryos". In: *Phytochemistry* 68.16 (2007), pp. 2341–2350.

[Tsc12] Henning Tschiersch, Gregor Liebsch, Ljudmilla Borisjuk, Achim Stangelmayer, and Hardy Rolletschek. "An imaging method for oxygen distribution, respiration and photosynthesis at a microscopic level of resolution". In: *New Phytologist* 196.3 (2012), pp. 926–936.

[VA84] H Van As and TJ Schaafsma. "Noninvasive measurement of plant water flow by nuclear magnetic resonance". In: *Biophysical journal* 45.2 (1984), pp. 469–472.

[VA07] Henk Van As. "Intact plant MRI for the study of cell water relations, membrane permeability, cell-to-cell and long distance water transport". In: *Journal of Experimental Botany* 58.4 (2007), pp. 743–756.

[VA09] Henk Van As, Tom Scheenen, and Frank J Vergeldt. "MRI of intact plants". In: *Photosynthesis Research* 102.2-3 (2009), p. 213.

[VA13] Henk Van As and John Van Duynhoven. "MRI of plants and foods". In: *Journal of Magnetic Resonance* 229 (2013), pp. 25–34.

[VB13] Aart JE Van Bel, Ykä Helariutta, Gary A Thompson, Jurriaan Ton, Sylvie Dinant, Biao Ding, and John W Patrick. "Phloem: the integrative avenue for resource distribution, signaling, and defense". In: *Frontiers in plant science* 4 (2013), p. 471.

[Vig03] Georgia Vigli, Angelos Philippidis, Apostolos Spyros, and Photis Dais. "Classification of edible oils by employing 31P and 1H NMR spectroscopy in combination with multivariate statistical analysis. A proposal for the detection of seed oil adulteration in virgin olive oils". In: *Journal of Agricultural and Food Chemistry* 51.19 (2003), pp. 5715–5722.

[Voz96] JA Vozzo, JM Halloin, TG Cooper, and EJ Potchen. "Use of NMR [nuclear magnetic resonance] spectroscopy and magnetic resonance imaging for discriminating Juglans nigra L. seeds". In: *Seed Science and Technology (Switzerland)* (1996).

[Wan94] Ning Wang and Donald B Fisher. "The use of fluorescent tracers to characterize the post-phloem transport pathway in maternal tissues of developing wheat grains". In: *Plant Physiology* 104.1 (1994), pp. 17–27.

[Wan16] Xiaodong Wang, Li Chen, Aina Wang, Hao Wang, Jianhua Tian, Xiaoping Zhao, Hongbo Chao, Yajun Zhao, Weiguo Zhao, Jun Xiang, et al. "Quantitative trait loci analysis and genome-wide comparison for silique related traits in Brassica napus". In: *BMC plant biology* 16.1 (2016), p. 71.

[Wan81] G Wanner, H Formanek, and RR Theimer. "The ontogeny of lipid bodies (spherosomes) in plant cells". In: *Planta* 151.2 (1981), pp. 109–123.

[Wei11] Karin Weitbrecht, Kerstin Müller, and Gerhard Leubner-Metzger. "First off the mark: early seed germination". In: *Journal of experimental botany* 62.10 (2011), pp. 3289–3309.

[Wex68] Lewis Wexler, Derek H Bergel, Ivor T Gabe, Geoffrey S Makin, and Christopher J Mills. "Velocity of blood flow in normal human venae cavae". In: *Circulation Research* 23.3 (1968), pp. 349–359.

[Whe15] Heather L Wheeler, Ronald Soong, Denis Courtier-Murias, Adolfo Botana, Blythe Fortier-Mcgill, Werner E Maas, Michael Fey, Howard Hutchins, Sridevi Krishnamurthy, Rajeev Kumar, et al. "Comprehensive multiphase NMR: a promising technology to study plants in their native state". In: *Magnetic Resonance in Chemistry* 53.9 (2015), pp. 735–744.

[Wil99] Deborah K Wilkins, Shaun B Grimshaw, Véronique Receveur, Christopher M Dobson, Jonathan A Jones, and Lorna J Smith. "Hydrodynamic radii of native and denatured proteins measured by pulse field gradient NMR techniques". In: *Biochemistry* 38.50 (1999), pp. 16424–16431.

[Win06] Carel W Windt, Frank J Vergeldt, P Adrie De Jager, and Henk Van As. "MRI of long-distance water transport: a comparison of the phloem and xylem flow characteristics and dynamics in poplar, castor bean, tomato and tobacco". In: *Plant, Cell & Environment* 29.9 (2006), pp. 1715–1729.

[Win09] Carel W Windt, Edo Gerkema, and Henk Van As. "Most water in the tomato truss is imported through the xylem, not the phloem: a nuclear magnetic resonance flow imaging study". In: *Plant Physiology* 151.2 (2009), pp. 830–842.

[Woj06] Łukasz Wojtyla, Małgorzata Garnczarska, Tomasz Zalewski, Waldemar Bednarski, Lech Ratajczak, and Stefan Jurga. "A comparative study of water distribution, free radical production and activation of antioxidative metabolism in germinating pea seeds". In: *Journal of plant physiology* 163.12 (2006), pp. 1207–1220.

[Yus06] Paul A Yushkevich, Joseph Piven, Heather Cody Hazlett, Rachel Gimpel Smith, Sean Ho, James C Gee, and Guido Gerig. "User-guided 3D active contour segmentation of anatomical structures: significantly improved efficiency and reliability". In: *Neuroimage* 31.3 (2006), pp. 1116–1128.

[Zam04] Patricia Zambryski. "Cell-to-cell transport of proteins and fluorescent tracers via plasmodesmata during plant development". In: *The Journal of cell biology* 164.2 (2004), pp. 165–168.

[Zha09] Hui-Juan Zhang, Zheng-Gui Wei, Hai-Yan Zhao, Hong-Xia Yang, Hui-Xin Li, and Feng Hu. "Effects of low-molecular-weight organic acids on gadolinium accumulation and transportation in tomato plants". In: *Biological trace element research* 127.1 (2009), pp. 81–93.

Books

[Ber04] Matt A Bernstein, Kevin F King, and Xiaohong Joe Zhou. *Handbook of MRI pulse sequences*. Elsevier, 2004.

[Bro14] Robert W Brown, Y-C Norman Cheng, E Mark Haacke, Michael R Thompson, and Ramesh Venkatesan. *Magnetic resonance imaging: physical principles and sequence design*. John Wiley & Sons, 2014.

[Cal93] Paul T. Callaghan. *Principles of nuclear magnetic resonance microscopy*. Oxford University Press on Demand, 1993.

[Die12] Peter Diehl, Ekkehard Fluck, and Robert Kosfeld. *NMR Basic Principles and Progress/NMR Grundlagen und Fortschritte*. Vol. 7. Springer Science & Business Media, 2012.

[Fri13] Horst Friebolin. *Ein-und zweidimensionale NMR-Spektroskopie: eine Einführung*. John Wiley & Sons, 2013.

[Kau05] Arie Kaufman and Klaus Mueller. *7 - Overview of Volume Rendering*. Ed. by Charles D. Hansen and Chris R. Johnson. Burlington: Butterworth-Heinemann, 2005, pp. 127 –174. ISBN: 978-0-12-387582-2.

[Kee11] James Keeler. *Understanding NMR spectroscopy*. 2nd ed. West Sussex: John Wiley & Sons, 2011. ISBN: 978-0-470-74609-7.

[Lan12] Otto Ludwig Lange, Ludger Kappen, and E-D Schulze. *Water and plant life: problems and modern approaches*. Vol. 19. Springer Science & Business Media, 2012.

[Lev08] Malcolm H. Levitt. *Spin Dynamics - Basics of Nuclear Magnetic Resonance*. 2nd ed. John Wiley & Sons Ltd, 2008. ISBN: 978-0-470-51118-6.

Theses

[Ham15] Sebastian Hammer. "Kontrastmittelgestützte T_1-Messungen zur Untersuchung des Nährstofftransportsystems von Pflanzen". Zulassungsarbeit für die Staatsexamensprüfung. Julius-Maximilians-Universität Würzburg, 2015.

[Jä17] Andreas Jäger. "Magnetresonanz-Bildgebung von chemischen Austauschprozessen". Bachelor thesis. Julius-Maximilians-Universität Würzburg, 2017.

[Kau08] Ilja Kaufmann. "Funktionelle NMR-Mikroskopie and Pflanzenwurzeln". PhD thesis. Julius-Maximilians-Universität Würzburg, 2008.

[Mel09a] Gerd Melkus. "Entwicklung und Anwendung spektroskopischer ^{1}-NMR-Methoden zur in vivo Charakterisierung von Xenograft-Tumormodellen bei 17.6 T". PhD thesis. Julius-Maximilians-Universität Würzburg, 2009.

[Reu17] Lucas Reuther. "Charakterisierung einer neuen Methode zur Untersuchung von chemischen Austauschprozessen mittels MRT". Bachelor thesis. Julius-Maximilians-Universität Würzburg, 2017.

[Tri15a] Simon Triphan. "T_1- und T_2^*-Quantifizierung in der menschlichen Lunge". PhD thesis. Julius-Maximilians-Universität Würzburg, 2015.

[Win11] Patrick Winter. "Radiale Bildgebung am Hochfeld". Diploma thesis. Julius-Maximilians-Universität Würzburg, 2011.

Online sources

[Bru17] BrukerCorporation. *111 KHz probe for ultra-fast magic angle spinning.* 2017. URL: https://www.bruker.com/products/mr/nmr/probes/probes/solids/very-fast-mas/07-mm/overview.html (visited on 02/26/2018).

[Bun16] Bundesministerium für Ernährung und Landwirtschaft. *Statistisches Jahrbuch des BMEL für 2013, Tabelle 209.* 2016. URL: http://www.bmel-statistik.de//fileadmin/user_upload/010_Jahrbuch/Agrarstatistisches-Jahrbuch-2016.pdf (visited on 02/26/2018).

[COD17a] CODATA. *proton gyromagnetic ratio.* 2017. URL: http://physics.nist.gov/cgi-bin/cuu/Value?gammap (visited on 02/26/2018).

[COD17b] CODATA. *proton gyromagnetic ratio over 2 pi.* 2017. URL: http://physics.nist.gov/cgi-bin/cuu/Value?gammapbar (visited on 02/26/2018).

[Dat18] Open Chemistry Database. *Sucrose*. 2018. URL: `https://pubchem.ncbi.nlm.nih.gov/compound/sucrose` (visited on 02/26/2018).

[Fes17] Jeffrey A. Fessler. *Michigan Image Reconstruction Toolbox (MIRT)*. 2017. URL: `http://web.eecs.umich.edu/~fessler/code/index.html` (visited on 02/26/2018).

[Int17] International Union for Conservation of Nature. *Table 1: Numbers of threatened species by major groups of organisms (1996–2017)*. 2017. URL: `http://cmsdocs.s3.amazonaws.com/summarystats/2017-1_Summary_Stats_Page_Documents/2017_1_RL_Stats_Table_1.pdf` (visited on 02/26/2018).

[O'H12] Thomas C. O'Haver. *MATLAB peakfit.m*. 2012. URL: `http://terpconnect.umd.edu/~toh/spectrum/InteractivePeakFitter.htm` (visited on 02/26/2018).

Conference Proceedings

[Nay00] Krishna S Nayak, John M Pauly, Garry E Gold, and Dwight G Nishimura. "Imaging ultrashort T2 species in the brain". In: *Proc Int Soc Magn Reson Med*. Vol. 509. 2000.

Patents

[Bot84] Paul A Bottomley. *Selective volume method for performing localized NMR spectroscopy*. US Patent 4,480,228. 1984.

List of Publications

Patents

[Jak17] P. M. Jakob, F. T. Gutjahr, **E. Munz**: Method and System to Detect a Solute in a Solvent Using Nuclear Magnetic Resonance, Date of filing as European Patent: 22.12.2017

Peer-reviewed articles

[Gut18a] F. T. Gutjahr, **E. Munz**, P. M. Jakob: *Positive Chemical Exchange Contrast in MRI using Refocused Acquisition of Chemical Exchange Transferred Excitations (RACETE)*, Zeitschrift fuer Medizinische Physik (2018), DOI: 10.1016/j.zemedi.2018.05.005

[Rad18a] V. Radchuk, V. Tran, R. Radchuk, M. Diaz-Mendoza, D. Weier, D. Riewe, J. Fuchs, G. Hensel, J. Kumlehn, **E. Munz**, N. Heinzel, H. Rolletschek, M. Martinez, L. Borisjuk: *Vacuolar processing enzyme 4 contributes to maternal control of grain size in barley by executing programmed cell death in pericarp*, New Phytologist 218 (2018): 1127–1142, DOI: 10.1111/nph.14729

[Mun17] **E. Munz**, H. Rolletschek, S. Oeltze, J. Fuchs, A. Gündel, T. Neuberger, S. Ortleb, P. M. Jakob, L. Borisjuk: *A functional imaging study of germinating oilseed rapeseed*, New Phytologist 216 (2017): 1181-1190, DOI: 10.1111/nph.14736

[Sch17] S. Scherzer, L. Shabala, B. Hedrich, J. Fromm, H. Bauer, **E. Munz**, P. M. Jakob, K. Al-Rascheid, I. Kreuzer, D. Becker, M. Eiblmeier, H. Rennenberg, S. Shabala, M. Bennett, E. Neher and R. Hedrich: *Insect hapto-electrical stimulation of Venus flytrap triggers exocytosis in gland cells*, Proceedings of the National Academy of Sciences 114.18 (2017): 4822-4827. DOI: 10.1073/pnas.1701860114

[Woo17] H. Woodfield, D. Sturtevant, L. Borisjuk, **E. Munz**, I. Guschina, K. Chapman, J. Harwood: *Spatial and temporal mapping of key lipid species in Brassica napus seeds*, Plant Physiology 173.4 (2017): 1998-2009. DOI: 10.1104/pp.16.01705

[Mun16] **E. Munz**, P. M. Jakob, L. Borisjuk: *The potential of nuclear magnetic resonance to track lipids in planta*, Biochimie 130 (2016): 97-108. DOI: 10.1016/j.biochi.2016.07.014

[Kov16] N. Kovalchuk, W. Chew, P. Sornaraj, N. Borisjuk, N. Yang, R. Singh, N. Bazanova, Y. Shavrukov, A. Guendel, **E. Munz**, L. Borisjuk, P. Langridage, M. Hrmova, S. Lopato: *The homeodomain transcription factor TaHDZipI-2 from wheat regulates flowering time, frost tolerance and grain size*, New Phytologist 211.2 (2016): 671-687. DOI: 10.1111/nph.13919

[Rol15b] H. Rolletschek, E. Grafahrend-Belau, **E. Munz**, V. Radschuk, R. Kartäusch, H. Tschiersch, G. Melkus, F. Schreiber, P. M. Jakob ,L. Borisjuk: *Metabolic architecture of the cereal grain and its relevance to maximize carbon use efficiency*, Plant Physiology 2015;169(3): 1698-1713. DOI: 10.1104/pp.15.00981

[Sch14] J. Schwender, C. König, M. Klapperstück, N. Heinzel, **E. Munz**, I. Hebbelmann, J. O. Hay, P. Denolf, S. De Bodt, H. Redestig, E. Caestecker, P. M. Jakob, L. Borisjuk, H. Rolletschek: *Transcript abundance on its own cannot be used to infer fluxes in central metabolism*, Frontiers in Plant Science 2014;5:668. DOI: 10.3389/fpls.2014.00668

Conference Proceedings

Talks

[Bor18] L. Borisjuk, **E. Munz**, P. M. Jakob, T. Neuberger: *New Nuclear Magnetic Resonance Imaging Tools For Plant Developmental Biology*, 12th Congress of the International Plant Molecular Biology, (2018)

[Mei18] T. Meitzel, R. Radchuk, E. L. McAdam, I. Thormählen, R. Feil, **E. Munz**, P. Geigenberger, J. J. Ross, J. E. Lunn, L. Borisjuk: *Activation of auxin biosynthesis by trehalose 6?phosphate is required for normal seed filling in pea (Pisum sativum)*, 12th Congress of the International Plant Molecular Biology, (2018)

[Rad18b] V. Radchuk, V. Tran, J. Fuchs, G. Hensel, **E. Munz**, H. Rolletschek, L. Borisjuk: *Programmed Cell Death In Maternal Seed Tissues Controls Endosperm Development And Filling Of Cereal Grains*, 12th Congress of the International Plant Molecular Biology, (2018)

[Gut18b] F. T. Gutjahr, **E. Munz**, P. M. Jakob: *Darstellung von chemischem Austausch mit positivem Kontrast*, 21. Jahrestagung der Deutschen Sektion der ISMRM, (2018), (**V17**)

[Rol16] H. Rolletschek, E. Grafahrend-Belau, **E. Munz**, L. Borisjuk : *Unravelling the metabolic architecture of cereal grains and perspectives for crop improvement* , PBE (Plant Biology Europe), (2016), (**T18**)

[Hop12b] A. J. Hopfgartner, F. Fidler, **E. Munz**, P. M. Jakob: *MoCoLoCo: 3D MR-based High-Resolution Motion Correction*, ESMRMB, (2012), (**242**)

Posters

[Rol18] H. Rolletschek, A. Gündel, **E. Munz**, S. Ortleb, L. Borisjuk: *Metabolic view on the awakening of life in germinating oilseeds (Brassica napus)*, 12th Congress of the International Plant Molecular Biology, (2018), (**P247**)

[Rad18c] V. Radchuk, R. Sharma, E. Potokina, R. Radchuk, **E. Munz**, Nils Stein, B. Kilian, L. Borisjuk: *The Jekyll Genes, Important For Sexual Reproduction, Are Lineage Specific For The Closely Related Grass Tribes Triticeae And Bromeae*, 12th Congress of the International Plant Molecular Biology, (2018), (**P231**)

[Lee17] G. Lee, J. Choi, **E. Munz**, I. T. Ozbolat, M. Lanagan, T. Neuberger: *Multi scroll coil setup for simultaneous acquisition of MR microscopy data sets of 3D printed cells*, Proc. Intl. Soc. Mag. Reson. Med. 25, (2017), (**3792**)

[Kei17] P. Keil, **E. Munz**, H. Rolletschek, L. Borisjuk: *Current status of non-invasive, high throughput analysis of seed metabolism at IPK*, PLANT 2030 Status Seminar 2017, (2017)

[Mun15b] **E. Munz**, P. Winter, L. Borisjuk, P. M. Jakob: *Seeing the unseen in plants with UTE-imaging*, Proc. ICMRM 13, (2015), (**P107**)

[Mun15a] **E. Munz**, L. Borisjuk, P. M. Jakob, T. Neuberger: *3D distribution of unsaturated fatty acid components in seeds*, Proc. ICMRM 13, (2015), (**P108**)

[Ham15] S. Hammer, **E. Munz**, L. Borisjuk, P. M. Jakob: *Contrast agent aided localisation of active transport tissue in canola*, Proc. ICMRM 13, (2015) (**P109**)

[Rol15b] H. Rolletschek, J. Schwender, C. König, **E. Munz**, L. Borisjuk: *Transcript abundance on its own cannot be used to infer fluxes in central oilseed metabolism*, Gordon Research Conference: Plant Lipids: Structure, Metabolism & Function (2015), Galveston

[Bor15] L. Borisjuk, H. Rolletschek, **E. Munz**, J. Fuchs, T. Neuberger, P. M. Jakob: *Nuclear magnetic resonance imaging and quantification of lipid in living plants*, Gordon Research Conference: Plant Lipids: Structure, Metabolism & Function (2015), Galveston

[Mun13] **E. Munz**, J. Fuchs, L. Borisjuk, P. M. Jakob: *3D Water and Lipid MR-Microscopy of Rape Seed Germination Dynamics*, Proc. ICMRM 12 (2013), (**P88**)

[Lyk13] G. Lykowsky, F. Carinci, K. Hemberger, **E. Munz**, P. M. Jakob, D. Haddad: *Quantitative Sodium MRI in an osteoarthritis Goat model: Preliminary results*, Proc. Intl. Soc. Mag. Reson. Med. 21 (2013), (**3549**)

[Mun12] **E. Munz**, A. J. Hopfgartner, S. Raghuraman, T. Lanz, P. M. Jakob: *Motion-Tracking: fast high-resolution 2D motion quantification and depiction of shivering*, Proc. Intl. Soc. Mag. Reson. Med. 20 (2012), (**2469**)

[Hop12a] A. J. Hopfgartner, **E. Munz**, F. Fidler, P. M. Jakob: *Motion Correction: MRI-based ultra-fast high-resolution 3D-tracking*, Proc. Intl. Soc. Mag. Reson. Med. 20 (2012), (**2471**)

Danksagung

Nach fünf aufregenden, spannenden und wunderschönen Jahren ist es an der Zeit, neue Wege zu gehen. Wie jeder andere Mensch auch habe ich mich weiterentwickelt.

Jasmin Wagner (Blümchen) - 2000

An dieser Stelle möchte ich mich bedanken bei

- **Prof. Dr. Peter M. Jakob**, für die Möglichkeit, diese Dissertation am Lehrstuhl für Experimentelle Physik V der Universität Würzburg anzufertigen, sowie für die hilfreichen Impulse und Hinweise während der Arbeit.

- **Dr. Ljudmilla Borisjuk**, für die nahezu unendlich vielen Ideen, welche Pflanze man als nächstes messen sollte, wofür man die Ergebnisse verwenden kann und wie man sie am besten darstellt. Auch für die zahlreichen Lieferungen von Samen, Pflanzen und sonstigen Messobjekten.

- **Dr. Thomas Neuberger**, für die gemeinsamen Messungen, die freundliche Aufnahme und Unterbringung in den USA, die vielen Gespräche und natürlich für die Tipps und Anregungen! Vor allem aber vielen Dank für die Motivation, die ich durch unsere gemeinsame Arbeit erhalten habe!

- **Sabine Voll**. Für ganz viel! Für das Lachen, das durch die Wand dringt, für die Unterstützung im Labor und für die vielen kleinen Gemeinheiten und großen Nettigkeiten!

- **Fabian Gutjahr**, für die spannende gemeinsame Arbeit und Forschung an CEST und RACETE (a.k.a. CEET). Vor allem aber für die vielen lehrreichen Programmier-Sessions am AMX und die sehr unterhaltsamen Diskussionen, teilweise zu den ungewöhnlichsten Tages- und Nachtzeiten per Skype, WhatsApp und Email.

- **Sabine Herrmann** und **Stefan Ortleb**, eure Segmentierungen meiner Messdaten haben oftmals erst den entscheidenen Schritt nach vorne befähigt.

- **Steffen Wagner**, für die regelmäßige Versorgung mit (noch) lebenden Pflanzen, die leider immer noch auf regelmäßiges Gießen und ausreichend Licht angewiesen sind, sowie für die Unterstützung bei der Betreuung unseres 400ers.

- Der **Arbeitsgruppe AAN (Assimilat-Allokation und NMR)** am IPK Gatersleben, für und mit euch zu arbeiten macht einfach Spaß!

- **Thomas Kampf** und **Dr. Volker Sturm**, für die Bereitschaft, ihr enormes und umfangreiches Fachwissen jederzeit mit mir zu teilen.

- **Dr. Daniel Weber**, für die Hilfe beim Heliumfüllen am AMX und dafür, dass ich diese Tätigkeit im Anschluss an ihn übergeben durfte. Auch für viele interessante Gespräche beim Füllen, Essen und im Labor.

- **Johannes Fuchs**, für die Unterstützung bei der Einarbeitung in den Themenbereich der Pflanzenbildgebung und die hilfreichen Tipps bei Fragen und Problemen.

- **Patrick Winter**, für die Einarbeitung und Hilfestellung bei den UTE-Messungen. Deine Programmier-Arbeit ist wirklich beeindruckend!

- **Sebastian Hammer**, für die angenehme gemeinsame Arbeit mit Kontrastmitteln an Pflanzen und besonders für den kreativen Arbeitstitel!

- **Andreas Jäger**, für den Spaß und das Interesse an den durchgeführten CEST-Messungen, die in Zukunft auch an Pflanzen getestet werden.

- **Dr. Florian Fidler**, **Markus Düring** und **Gunthard Lykowsky**, ohne die die verwendeten Messspulen niemals in so kurzer Zeit wieder einsatzbereit gewesen wären.

- **Dr. Simon Triphan**, mit dem ich als EP5-Praktikant die ersten Erfahrungen im Bereich der MR-Bildgebung sammeln konnte. Auch verdanke ich ihm das Wissen, was der π-day ist und warum Kuchen für erfolgreiche Wissenschaft essenziell ist.

- **Dr. Andreas Hopfgartner**, für die Betreuung während meiner Diplomarbeit und die Hilfe bei der Einarbeitung in die Doktorarbeit. Vor allem aber für die unzähligen Kommentare, Witze und Sprüche, die einem den Arbeitsalltag ungemein erheitert haben.

- Den **Mensa-Lemmingen**, der Essensgruppe der EP5. Die gemeinsamen Mahlzeiten und Gespräche waren oftmals ein Highlight des kompletten (Mess-)Alltags.
- Den Ex- und aktuellen Bewohnern sowie den regelmäßigen Besuchern von **Büro E090**, für die angenehme Arbeitsatmosphäre, die vielen Diskussionen und die Unterstützung bei Problemen und Fragestellungen.
- Especially I want to thank **Dr. Catherine Smith** for correcting my spelling and grammar mistakes. Guten Tag!
- Allen weiteren **Korrekturlesern** dieser Dissertation, für das Finden und Anstreichen der Fehler, für zahlreiche konstruktive Vorschläge und besonders für die aufgewandte Zeit.